POLITECNICO DI TORINO

Master's Degree in Aerospace Engineering

Master's Degree Thesis

Temporal Scales in the Multiphase Microphysics of Warm Clouds

Supervisors

Prof. Daniela TORDELLA

Dr. Federico FRATERNALE

Prof. Jörg SCHUMACHER

Candidate

Ludovico FOSSÀ

April 2020

Abstract

The large scale dynamics of warm atmospheric clouds are strongly coupled to small scale turbulence and droplet microphysics. The entrainment-mixing process is crucial in determining cloud evolution and is believed to foster spectral broadening and to enhance droplet collision and coalescence. Temporal scales such as evaporation, phase relaxation and reaction times have been widely used to parameterize the impact of turbulent mixing on cloud evolution. In this thesis their role is investigated through a particle-resolved three-dimensional pseudospectral direct numerical simulation model. The evolution of the cloud-clear air interface at cloud top is modeled as an initial value problem of decaying turbulence. Several numerical experiments were carried out over the same computational domain with different initial conditions. The model also considers solution and curvature effects, droplet collisions, temperature stratification and vertical stability. Droplet and time scale statistics are computed by averaging over the planes parallel to the interface. The attempt to parameterize the spectral broadening as a function of both phase relaxation and eddy turnover times has not been successful. Polydisperse distributions exhibit a departure from the homogeneous mixing limit above the cloud top after a few elapsed eddy turnover times. Relatively high values for the evaporation time are found in regions close to the cloud core, whereas the saturation and phase relaxation times show higher values above the interface in the clear air slab. Estimates for the reaction time are in good agreement with such results. Evaporation, phase relaxation and saturation times appear to be positively, negatively and poorly correlated, respectively, with the homogeneous mixing degree across the interface.

Acknowledgements

First and foremost, I would like to thank my leading supervisor, prof. Daniela Tordella, for all her support and scientific guidance. She gave me the opportunity of participating in one of her research projects, organized my stay in Germany during that time and truly helped me out in many situations. I acknowledge prof. Jörg Schumacher of TU Ilmenau for kindly hosting me at the Institut für Thermo- und Fluiddynamik during the months of October and November. Our scientific discussions and his suggestions helped me better understanding the problems we were dealing with. It truly was a formative experience to me. I must thank Dr. Federico Fraternale for all his support and for putting up with me every time I had an issue with the codes. Even while I was spending time abroad he would have a moment to call and help out. The same for Shahbozbek Abdunabiev, whose programming tips have been crucial. This thesis would have never been completed without his contribution. I also thank PhD student Mina Golshan and MoS student Mattia Tomatis, for all the time we spent together on the project at PoliTo and Najmee, Philip and Sandeep for our time in Ilmenau. I wish you all the best for your future.

I thank my family and friends for supporting me all the time. Maria Grazia, Umberto, my sister Daria, all the people who accompanied me during these years, for the good time we spent together. Salvo, Elena, Sofia, Tommy, Poggio, Samir, Enrica, Sophie, Pica, Pellé... It's just too many of you! I just can't name you all, but you know this work is dedicated to you too. Quiero también dedicar este trabajo a María Rosa y Héctor, que me acojeron y me ayudaron durante mi estadía en Argentina. Los quiero muy mucho.

Table of Contents

Acronyms

CN
: condensation nuclei

CCN
: cloud condensation nuclei

DNS
: direct numerical simulations

DSD
: droplet size distribution

HIT
: homogeneous isotropic turbulence

MVD
: mean volume radius

PDF
: probability density function

TKE
: turbulent kinetic energy

Chapter 1

Introduction

Cloud systems give a unique texture to the Earth surface. They can shade large portions of continents and oceans and can be easily spotted by observing our planet from the outer space. It is evident that these large hydrometeors have a considerable impact upon geophysical dynamics, weather and climate. Clouds are important actors on the stage of atmospheric circulation, planetary radiative balance and water redistribution. Their existence is determined by atmosphere dynamics, which are - in turn - strongly influenced by the clouds themselves. This coupling accounts for the complexity of such systems, which also results in their unpredictability, an aspect that has fascinated humans - and artists - for ages. Impalpable and isolated, clouds are represented in a number of paintings and artworks that ultimately unveil how their features haven't changed much during the late centuries (Raymond A. Shaw, 2003). Yet, clouds have turned out to be strongly influenced by anthropogenic effects (Raymond A. Shaw, 2003). Cloud modeling is a long-standing problem in weather and climate sciences because of the complexity of the processes involved (Devenish et al., 2012). This complexity has been held responsible of uncertainties in climate models at least since 1996[1] and even the relatively "*boring*" low-level marine type of clouds has been accused to be a "*big bad player on global warming*" due to the positive feedback they exert with warming oceans (Kerr, 2009).

Results from cloud models, simulations and laboratory and in situ-experiments may be difficult to interpret. An ubiquitous problem in cloud physics is to understand to what extent a scientific result can be generalised in order to reach the behavior of much more complex systems that are found in reality. Real cloud

[1]See the contribution of the WGI to the Second Assessment of the IPCC (Intergovernmental Panel on Climate Change) in 1996, p. 31 [https://www.ipcc.ch/site/assets/uploads/2018/02/ipcc_sar_wg_I_full_report.pdf].

systems are characterised by a number of complex phenomena that occur over a vast range of spatial and temporal scales (Devenish et al., 2012).

A cloud is a colloidal dispersion of sub-micron sized particles, liquid droplets and frozen ice crystals that forms in the atmosphere of a planet. All these constituents interact with the surrounding atmosphere gases (mainly air and water vapor), these interactions spanning over a number of scales, from less than a micrometer up to a few kilometers. The influence of buoyancy forces and atmospheric winds (wind shear) accounts for the production of kinetic energy in such flows, which naturally become turbulent. Turbulence is known to play a pivotal role in cloud physics and many cloud-related phenomena, such as droplet growth and shrinking by condensation, droplet clustering, collision and coalescence, atmosphere stability, interfacial mixing and aerosol activation (Devenish et al., 2012). These topics have known increasing popularity within the turbulence and multi-phase scientific communities in recent years. Turbulent flows feature a significant interaction between large and small scale processes, thus allowing the microphysics to have an impact on the droplet spectrum and the cloud radiative properties, ultimately determining cloud evolution (Devenish et al., 2012; Raymond A. Shaw, 2003).

Clouds can form, evolve and disappear readily. In fact, the evolution of a cloud depends how the condensed liquid water is redistributed among its droplets with time. The likelihood of a cloud to appear or to disappear strongly depends on its balance with the surrounding water vapor and temperature fields. The lifetime of a cloud depends on the cloud type, spanning somewhere between a few minutes and a couple of days.

Cloud formation is due to the condensation of saturated water vapor. Atmospheric aerosols act as cloud condensation nuclei (CCN) thus allowing small drops ($\sim$ 1µm) to start growing via heterogeneous nucleation in a supersaturated environment (Rogers & Yau, 1996). The rate of condensational growth for small spherical drops

$$\frac{dr^2}{dt} \sim 2s \tag{1.1}$$

is linear with the local level of supersaturation experienced by the droplet itself, r being the droplet radius and s the supersaturation. Condensation is important for small water drops, but turns to be slower and less effective for increasing droplets diameters. Increasing droplet mass results in increasing inertia, which modulates its response to droplet clustering and collision-coalescence (Raymond A. Shaw, 2003). For relatively large droplets ($\sim$ 30µm) collision-coalescence becomes integral to allow droplet growth up to drizzling radii ($\sim 10^2$ µm) (Devenish et al., 2012; Pruppacher & Klett, 2010). To start the precipitation, a number of water drops must grow big enough to settle and reach the ground before evaporating completely. One would expect the time required to reach drizzle ($\sim$ 100µm) or rain drops ($\sim$ 1mm) sizes to be longer than observed in reality (Lehmann, Siebert, & Shaw, 2009).

Conversely, warm clouds (i.e. clouds residing under non-freezing conditions) such as small shallow cumuli and trade wind cumuli are observed to precipitate readily - within 15-20 minutes - (Göke, Ochs, & Rauber, 2007; Laird, Ochs, Rauber, & Miller, 2000; Szumowski, Rauber, Ochs, & Miller, 1997). The reasons behind the rapid onset of precipitation in such clouds have yet to be explained (Lehmann et al., 2009; Tölle & Krueger, 2014; Yang, Shaw, & Xue, 2016). Several hypotheses have been proposed, pointing out to the role played by giant and ultragiant CCN, the presence of "*lucky*" droplets with enhanced collisional growth rates (Yang et al., 2016) and local turbulent bursts of supersaturation that speed up the condensational growth (Raymond A. Shaw, 2000; Raymond A. Shaw, Reade, Collins, & Verlinde, 1998). Intermittent structures are the hallmark of turbulent flows at the scales close to the dissipative range (H. Siebert, Gerashchenko, et al., 2010): in-situ measurements conducted in stratocumulus clouds near the cloud top revealed an intermittent behavior consistent with the Kolmogorov-Obukhov refined similarity hypothesis with scalings that are somewhat similar to those typical of homogeneous isotropic turbulence, also featuring a dissipation rate that reaches the maximum value near the cloud top (H. Siebert, Shaw, & Warhaft, 2010).

Entrainment and detrainment at cloud boundaries are important phenomena that significantly impact the evolution of the droplet population inside the cloud (Burnet & Brenguier, 2007). These processes are the consequence of the so-called interfacial instabilities, with buoyancy effects being prevalent at the cloud top (Devenish et al., 2012). The aim of this thesis is to study the commonly used time-scale parameterization of the entrainment-mixing process for a shearless mixing scenario at a cloud top-clear air interface. A number of studies (e.g. Lehmann et al., 2009 and Lu et al., 2018) has focused on time scale analysis and how it describes the behavior of the mixing process or the impact of turbulence on nucleation and spectral broadening (Chandrakar et al., 2016). Andrejczuk, Grabowski, Malinowski, and Smolarkiewicz, 2009; Gao, Liu, Li, and Lu, 2018; Kumar, Götzfried, Suresh, Schumacher, and Shaw, 2018; Kumar, Schumacher, and Shaw, 2014 adressed these issues via direct numerical simulations (DNS).

DNS are numerical experiments that permit scientists to investigate the evolution of initial value problems in computational fluid dynamics (CFD). Their main advantage relies on the ability to theoretically describe all the spatial scales that are encompassed by a turbulent flow, including the smallest ones that are usually filtered in large eddy simulations (LES) (Pope, 2000, p. 344). If the scientific objective is to study the small scale interaction of micron-sized water drops and the turbulent structures, then DNS are the most valuable tool. In spite of a highly idealized setup, DNS are able to reproduce precisely the evolution of the Navier-Stokes equations and the coupling between small and large scales. By contrast, the main drawback is the computational cost, which can be enormous. The number of floating point operations rises steeply with the number of cells of the meshing grid

and the number of time steps ($\sim Re_\ell^3$) (Pope, 2000, p. 348). The use of DNS is therefore often limited to research applications, at moderate Reynolds numbers and for simple geometries.

The numerical model used in these experiments is based on a incompressible pseudo-spectral homogeneous isotropic solver, it accounts for droplet growth by condensation and collision-coalescence and includes the buoyancy feedback of water vapor and temperature but neglects the break-up of drizzle size drops and radiative cooling. The droplet response on the carrier flow is considered only though condensation and evaporative cooling. Simulations are not forced (as were for instance in Kumar, Schumacher, and Shaw, 2013) and follow a transient decay during runtime. For the purposes of this research campaign eighteen simulation runs have been executed. The computational domain is a parallelepiped composed by two cubes, each one hosting a zero-mean velocity turbulent region. The lower cube simulates the cloud slab, the higher cube the clear air segment. Periodic boundary conditions were adopted. The initial Taylor Reynolds number in the cloud cube is $Re_\lambda = 50$.

The outline of this thesis is the following: cloud dynamics and microphysics are discussed in chapter 2; in chapter 3 the most important concepts related to cloud turbulence and the mixing dynamics are presented; the role of temporal scales is introduced in chapter 4. Eventually, the numerical model is fully explained in chapter 5 and results are presented in chapter 6. Conclusions are drawn in chapter 7.

Chapter 2

Cloud dynamics and microphysics

The aim of this chapter it to provide a brief introduction to the fundamental concepts of cloud dynamics and microphysics. The ideas presented in the next pages are the key to setting up a numerical model for our analysis. Of course, this thesis does not expect to be exhaustive and shall focus on a very specific aspect of the roles that the temporal scales of microphysical and turbulent processes may have on cloud evolution. More complete discussions of the ideas that are expressed and accepted here can be found in literature (Khvorostyanov & Curry, 2014; Lamb & Verlinde, 2011; Pruppacher & Klett, 2010; Rogers & Yau, 1996).

2.1 Air, water vapor and aerosols

A cloud is a colloidal dispersion of air, water vapor, sub micron-sized aerosols, water drops and ice crystals. It forms through the condensation (or deposition) of water vapor into drops and crystals and disappears through evaporation (or sublimation) and precipitation. Water vapor can be found in large quantities in the Earth's troposphere. In fact, both dry air (which is a gas mixture itself) and water vapor behave, to a good approximation, as perfect gases. Then, the variations of their thermodynamic properties are well described by the law:

$$p = \rho \frac{R}{\mathcal{M}} T \tag{2.1}$$

p being the pressure, ρ the density, $R = 8314\ \mathrm{J\,kg^{-1}\,K^{-1}}$ the universal gas constant and T the static temperature. $\mathcal{M}$ is the molar mass of the gas mixture, which is roughly $29\ \mathrm{kg\,kmol^{-1}}$ for dry air. In the vapor phase, also water behaves as an ideal

gas to a good approximation. The water vapor partial pressure e can be defined via the perfect gas law:

$$e = \rho_v \frac{R}{\mathcal{M}_v} T \tag{2.2}$$

with ρ_v being the vapor density and $\mathcal{M}_v \cong 18\ \mathrm{kg\,kmol^{-1}}$. Let's focus on the condensation and evaporation processes. Depending on the local thermodynamic conditions there is a critical amount of vapor that can be absorbed by the atmosphere. When at equilibrium, the atmosphere is partly filled with liquid water and partly with vapor. The molecules are in agitation, some liquid molecules happen to break away from the liquid phase while the same amount of vapor molecules simultaneously collides with the liquid surface, hence changing phase. Under this conditions the vapor field is said to be saturated. That is, the water vapor partial pressure e equals the saturation vapor pressure e_s. If we assume that the phase transition occurs under isobaric and isothermal conditions (which can be considered correct to a good approximation) the variation of the saturation vapor pressure can be related to the variation of the static temperature via the **Clausius-Clapeyron** equation

$$\frac{de_s}{e_s} = \frac{L_w}{R_v} \frac{dT}{T^2} \tag{2.3}$$

L_w being the latent heat of evaporation and $R_v = R/\mathcal{M}_v$. e_s increases as temperature increases (Rogers & Yau, 1996). At 273.15 K the saturation vapor pressure is 611 Pa[1]. By integrating equation 2.3 with respect to these reference conditions we get

$$\frac{e_s(T)}{e_s(T_{ref})} = exp\left(\frac{L_w}{R_v T_{ref}}\left(1 - \frac{T_{ref}}{T}\right)\right)$$

and, by recalling equation 2.2

$$\frac{\rho_{sv}(T)}{\rho_{sv}(T_{ref})} = \frac{T_{ref}}{T} exp\left(\frac{L_w}{R_v T_{ref}}\left(1 - \frac{T_{ref}}{T}\right)\right) \tag{2.4}$$

In order to condense, the partial pressure must exceed the saturation pressure. That is, the relative humidity

$$RH = \frac{e}{e_s} = \frac{\rho_v}{\rho_{sv}}$$

must exceed unity. Another quantity which will be widely used in this work is the supersaturation

$$s = \frac{e}{e_s} - 1 = \frac{\rho_v}{\rho_{sv}} - 1$$

[1]See the table *Vapor pressure from 0 to 370°C* in (Lide, 2004).

whose positive values allow the condensation (deposition) process to occur. The relative humidity and the supersaturation in the atmosphere are functions of both the local vapor density and the static temperature. In fact, positive values for the supersaturation in the atmosphere do not exceed 2%, being too low to trigger homogeneous condensation. Homogeneous nucleation requires enormous levels of supersaturation to take place as a stable process. Conversely, water can condense over dispersed solid and hygroscopic aerosols that are likely to float in the atmosphere via a process known as heterogeneous condensation (Pruppacher & Klett, 2010). This is due to the fact that the presence of solute molecules in a substance can significantly lower the local saturation vapor pressure, allowing condensation to occur (Rogers & Yau, 1996). Activation and growth through variation of the saturation pressure near the surface of inorganic solutes are well described by the Köhler theory, which accounts for two opposite phenomena - the Raoult and the Kelvin effect - which determine the critical supersaturation level beyond which nucleation and hygroscopic growth are able to start (Wex, Stratmann, Topping, & McFiggans, 2008). A recent study by (Ovadnevaite et al., 2017) shows that the presence of organic surfactants can result in a reduction of the Kelvin effect without affecting the Raoult term, thereby leading to substantial increases in cloud droplet populations. This is very important for Earth regions, like the Amazon, where the local biosphere releases organic aerosols that are likely to serve as condensation nuclei (Pöschl et al., 2010).

Both organic and inorganic aerosols acting as condensation nuclei (CN) usually have a volume equivalent diameter D_ρ ranging between 0.01 and 1 µm. In some cases, giant and ultragiant aerosols (2 to 10 µm) can also act as a basis for the nucleation process leading to bigger CN and CCN. In figure 2.1 different kind of atmospheric aerosols (including rain, drizzle, haze and hail particles) are shown along with their absorbed/scattered radiation wavelengths.

Aerosol concentration can vary significantly in space and time depending on the presence of sources (volcanoes, forests, urban and industrial environments) and meteorological factors (Rogers & Yau, 1996). Large and hygroscopic aerosols serve as centers of nucleation and condensational growth.

2.2 Cloud thermodynamics and convection

As stated earlier, air and water vapor are part of a gas mixture. The masses of dry air and water vapor in a given volume are related through the mixing ratio

$$w = \frac{M_v}{M_a} = \frac{\rho_v}{\rho_a} \cong \frac{\mathcal{M}_v}{\mathcal{M}_a} \frac{e}{p}$$

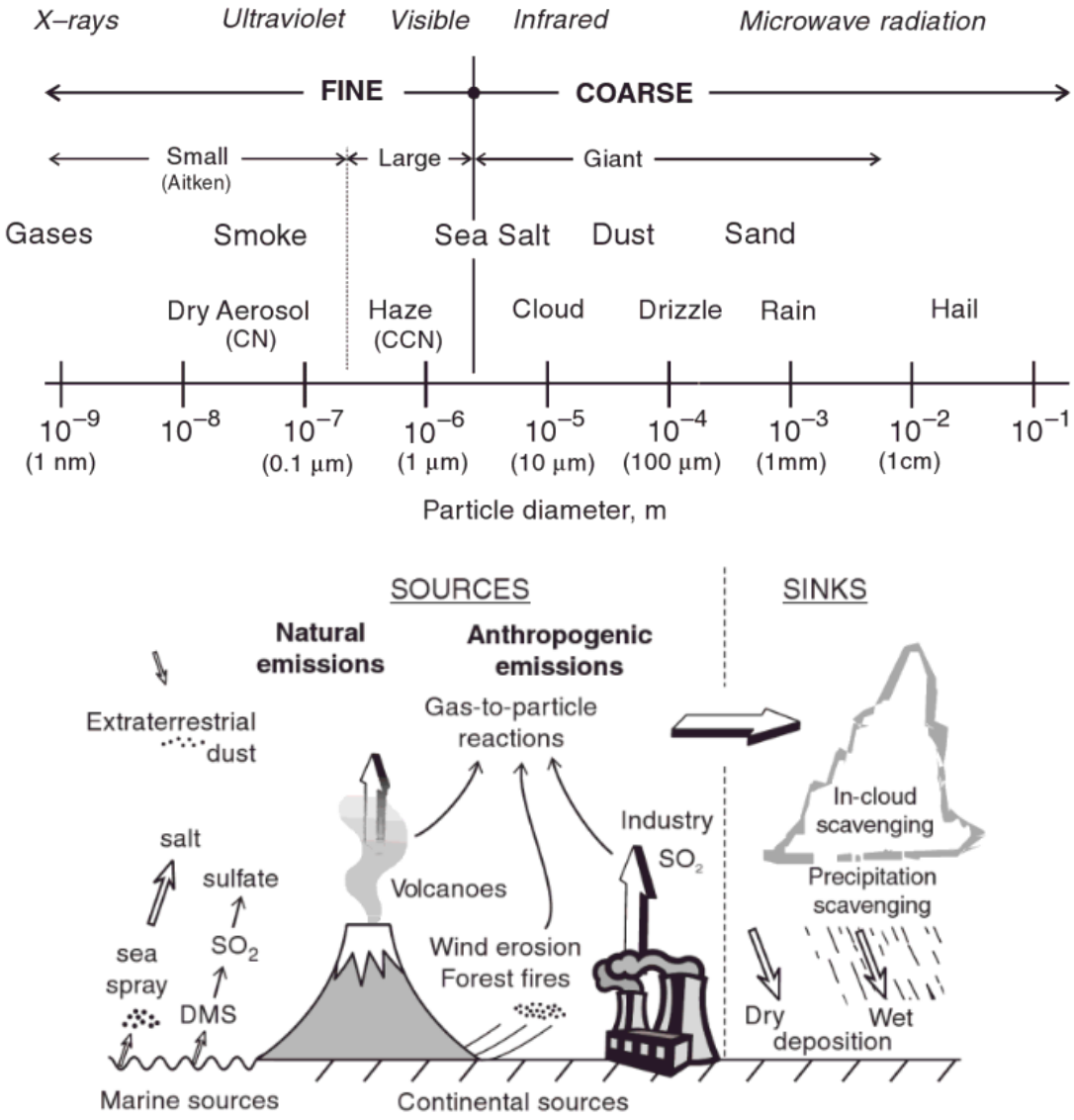

Figure 2.1: **Top:** aerosols found in the atmosphere. Distinction must be drawn between fine particles ($D_\rho < 2$µm) and coarse particles, such as sea salt, dust and sand grains falling into the class of *giant* aerosols. The emission wavelengths of each class are shown in the top line. **Bottom:** some possible aerosol sources (and sinks) in the atmosphere of planet Earth are shown in the aerosol cycle, from production to scavenging and deposition on the ground. Both images were taken from (Lamb & Verlinde, 2011), pp. 67-68.

and the specific humidity

$$q = \frac{M_v}{M_a + M_v} = \frac{\rho_v}{\rho_a + \rho_v} \cong \frac{\mathcal{M}_v}{\mathcal{M}_a}\frac{e}{p}$$

2.2.1 Adiabatic processes

A parcel of moist (i.e. which contains water vapor) or dry air in the atmosphere can be subject to a number of thermodynamic processes. Adiabatic processes are of particular interests in cloud physics, since in many cases cloud parcels may be modeled as gas mixtures that undergo adiabatic expansions or compressions. Clear air or cloud parcels can be advected upwards by buoyancy forces. The adiabatic hypothesis assumes that during the process the parcel does not cease nor gain heat:

$$\delta q = 0$$

An adiabatic process, if reversible, is also isentropic

$$ds = \frac{\delta q}{T}$$

an by applying the first law of thermodynamics

$$ds = \frac{\delta q}{T} = \frac{dh}{T} - \frac{1}{\rho}\frac{dp}{T} = c_p\left(\frac{dT}{T} - \frac{R}{\mathcal{M}c_p}\frac{dp}{p}\right) = c_p\frac{d\theta}{\theta}$$

c_p being the specific heat per mass unit. The variation of entropy depends on the variation of the quantity closed in the round brackets. θ is called the potential temperature and should not be confused with the static temperature T.

$$\frac{d\theta}{\theta} = \frac{dT}{T} - \frac{R}{\mathcal{M}c_p}\frac{dp}{p} \tag{2.5}$$

Potential temperature is a conservative variable for adiabatic processes:

$$\frac{dT}{T} = \frac{R}{c_p\mathcal{M}}\frac{dp}{p}$$

and can also be defined as the temperature that a parcel would reach if it were brought adiabatically from the initial conditions (p_0, T_0) to the lowest pressure (the ambient pressure p_{amb}).

The potential temperature also provides a criterion for the dynamic stability of a parcel of air. By differentiating equation 2.5 with respect to the altitude z, one gets

$$\frac{1}{\theta}\frac{\partial\theta}{\partial z} = \frac{1}{T}\frac{\partial T}{\partial z} - \frac{R}{c_p\mathcal{M}p}\frac{\partial p}{\partial z}$$

which can be expressed through Stevin's law

$$\frac{1}{\theta}\frac{\partial\theta}{\partial z} = \frac{1}{T}\frac{\partial T}{\partial z} + \frac{R\rho g}{c_p \mathcal{M} p} = \frac{1}{T}\left(\frac{\partial T}{\partial z} + \frac{g}{c_p}\right)$$

denoting the atmospheric lapse rate $\gamma = -\partial T/\partial z$, one gets the stability criterion

$$\frac{1}{\theta}\frac{\partial\theta}{\partial z} = \frac{1}{T}(\Gamma - \gamma) \tag{2.6}$$

the term on the right hand side of equation 2.6 represents the temperature difference between a parcel that was subjected to an adiabatic updraft (or downdraft) and the surrounding air. If its greater than zero, it means that the parcel will be subjected to a restoring buoyancy force (Rogers & Yau, 1996).

The relative humidity RH and the supersaturation s are both related to the local vapor density and temperature inside the cloud. A parcel of cloudy air that is advected upwards with vertical velocity w will experience an adiabatic expansion. Since it is assumed that the potential temperature remains approximately constant, the supersaturation of the cloud parcel is expected to increase with height. Once appropriate saturation conditions are reached (i.e. $RH \cong 1$ and $s \cong 0$) condensation may occur. In this case, the release of latent heat and the decrease of the vapor mass lead to a decrease of the supersaturation. It is evident that the evolution of s in a cloud parcel may be easily represented using a production - condensation model of the type

$$\frac{ds}{dt} = \underbrace{Q_1\frac{dz}{dt}}_{P} - \underbrace{Q_2\frac{dLWC}{dt}}_{C} \tag{2.7}$$

the LWC being the liquid water content of the cloud parcel, often measured in g/m^3. A detailed derivation of equation 2.7 and of the coefficient Q_2 can be retrieved in Rogers and Yau, 1996, pp. 105-112. This expression however does not take into account the transport of advection and diffusion of water vapor at the droplet surface (*ventilation effects*) but considers the supersaturation as a bulk property of the cloud parcel.

2.2.2 Isobaric processes

Processes occurring under constant pressure conditions p imply that relative variations of static and potential temperature remain the same. Assuming $dp = 0$ in equation 2.5 one gets

$$\frac{d\theta}{\theta} = \frac{dT}{T}$$

If a parcel of moist air is brought to a lower temperature, its saturated vapor pressure e_s decreases because of the Clausius-Clapeyron law 2.3. Saturation is

reached once the partial pressure of the vapor equals the saturated pressure $e = e_s$. The temperature that satisfies this condition is known as dew-point temperature T_d. For isobaric processes the stability criterion (equation 2.6) reduces to $dT/dz > 0$.

The production term in equation 2.7 is obviously null for this specific case. No steady updraft is considered and the evolution of supersaturation is dictated by the variation of the liquid water content alone (Lu et al., 2018), that is

$$\frac{ds}{dt} = -Q_2 \frac{dLWC}{dt}$$

coefficient Q_2 must be in the form of an inverse density m^3/kg. It can be derived analitically by considering that

$$ds = \frac{de}{e_s} - \frac{e}{e_s^2} de_s$$

using equations 2.2 and 2.3 one gets

$$\frac{ds}{dt} = \frac{1}{\rho_{sv} T} \left(\rho_v \frac{dT}{dt} + T \frac{d\rho_v}{dt} \right) - \frac{\rho_v}{\rho_{vs}} \frac{L_w}{R_v T^2} \frac{dT}{dt}$$

the temperature terms dT/dt account for the variation of T due to the release (absorption) of the latent heat of condensation L_w and can be expressed

$$\frac{dT}{dt} = -\frac{L_w}{c_p \rho_0} \frac{d\rho_v}{dt}$$

as a function of the variation of the local vapor density, with $\rho_0 \cong \rho_a$ being the bulk density of the mixture. By denoting $C_v = d\rho_v/dt$, the equation becomes

$$\frac{ds}{dt} = -\frac{C_v}{\rho_{sv}} \left[1 - \frac{\rho_v}{\rho_a} \frac{L_w}{c_p T} + \frac{\mathcal{M}_v}{\mathcal{M}_a} \frac{L_w^2}{p c_p T} \rho_v \right] \cong -\frac{C_v}{\rho_{sv}} \left[1 + \frac{\mathcal{M}_v}{\mathcal{M}_a} \frac{L_w^2}{p c_p T} \rho_v \right]$$

which is consistent with the expression for Q_2 reported in Rogers and Yau, 1996, p. 106 and with the analogous formulation adopted by Lu et al., 2018. The second term in the RHS of this equation is of order one and should not be omitted. However, one may neglect it to simplify the problem. The phase transition occurs between the vapor field and the droplets that are contained inside a reference volume $\Omega_{x,\delta}$

$$\frac{ds}{dt} \cong -\frac{C_v}{\rho_{sv}} = -\frac{1}{\rho_{sv}} \frac{1}{\Omega_{x,\delta}} \sum_{x_k \in \Omega_{x,\delta}} \frac{dm_k}{dt} \tag{2.8}$$

m_k being the mass of the k-th droplet.

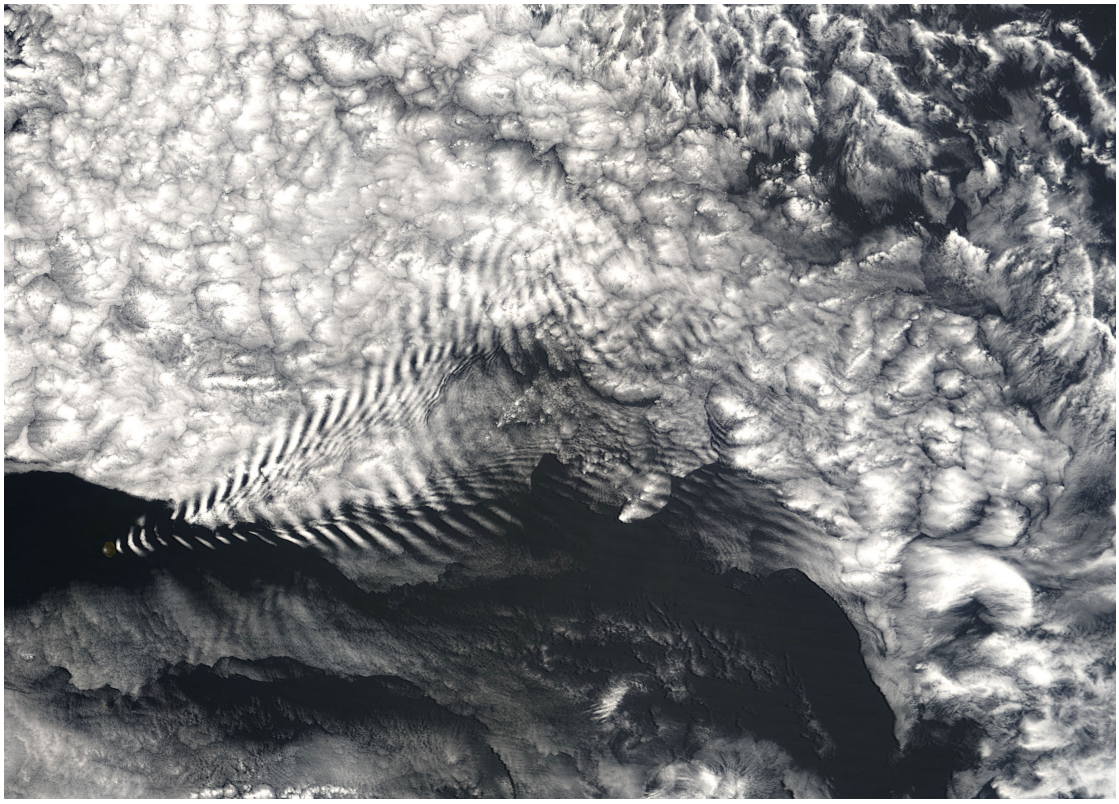

Figure 2.2: The effect of internal waves is depicted in this satellite image taken over the South Indian ocean in 2005. Parcels of moist air are advected ENE in the atmospheric stratified environment and forced to move upwards as they encounter the Amsterdam Island (bottom left). Since the system is stable, the parcel will undergo a wavy motion, reaching saturation at each updraft. A fraction of the water vapor will condense periodically with frequency $\mathcal{N}$. The nubes that form are known as *lenticular clouds* (picture by NASA Earth Observatory https://earthobservatory.nasa.gov/images/6151/wave-clouds-near-amsterdam-island).

2.3 Vertical stability in stratified flows

Clouds, as much as many other geophysical systems, are often subject to vertical variation of the density ρ. In the case of stable stratification, density decreases with height and arising vertical updraughts will be thus inhibited. The quantitative behavior of a stratified flow can be estimated through the internal Froude number

$$Fr_i^2 = \frac{U^2}{\left(\frac{g}{\rho_0}\frac{d\rho}{dz}\right) L} \tag{2.9}$$

with U and L being characteristic velocity and spatial scale of the phenomenon, ρ_0 its initial reference density. High Fr_i indicate that density gradients are weak comparing to the inertial forces, thus allowing vertical displacements. On the other hand, steep density gradients induce low values of Fr_i that do not permit intense vertical updraughts or downdraughts to arise (Tritton, 1988). In literature it is often used the inverse of the internal Froude number, the Richardson number Ri

$$Ri^2 = \frac{1}{Fr_i^2}$$

In general, density gradients can be often expressed as functions of potential (static) temperature gradients in the atmosphere. Non-dimensional parameters like Fr_i and Ri describe the response of a parcel of moist or dry air towards small external disturbances in a cloudy stratified environment. If one considers the forces acting on a parcel with density ρ_p that is displaced vertically in the z-direction (for small perturbations and constant $\nabla\rho$)

$$\rho_p \ddot{z} + g\frac{d\rho}{dz}z = 0$$

will get a differential equation for the vertical displacements z of the type

$$\ddot{z} + \mathcal{N}^2 z = 0$$

with $\mathcal{N}$

$$\mathcal{N}^2 = -\frac{g}{\rho_0}\frac{d\rho}{dz} \tag{2.10}$$

Real values of $\mathcal{N}$ (i.e. $\mathcal{N}^2 > 0$) account for a stable stratification, whilst imaginary values of $\mathcal{N}$ (i.e. $\mathcal{N}^2 < 0$) imply that the motion of the parcel will be amplified by the surrounding environment (Holton, 2004; Tritton, 1988). If one further assumes that, for small perturbations, the variation of density can be linearly related to the vertical temperature gradient

$$\frac{d\rho}{dz} = \frac{d}{dz}\left[\rho_0 - \rho_0\alpha\left(\theta - \theta_0\right)\right]$$

and that $\alpha = 1/T_0$, then will get the same stability criterion given by equation 2.6. The quantity $\mathcal{N}$ 2.10 is measured in Hz and is known as the **Brunt-Väisälä frequency** (Vallis, 2006). For positive values of $\mathcal{N}$, the advected parcel will be subjected to an oscillatory motion with this frequency and the disturbance will propagate as an *internal wave*. The internal Froude number can be expressed as a function of the Brunt-Väisälä frequency

$$Fr_i^2 = \frac{U^2}{L^2\mathcal{N}^2}$$

Again, positive values Fr_i^2 (or Ri^2) are associated to a stable stratification, while negative values of Fr_i^2 (or Ri^2) account for an unstable stratification.

2.4 Droplet growth by condensation

Growth of spherical water droplets in a humid environment is influenced by both Kelvin and Raoult effects. The droplet growth rate takes account of both these effects along with the local value of the supersaturation s. Following (Ghan et al., 2011; Howell, 1949; Köhler, 1922), a good estimate of the droplet growth rate is provided by the relation

$$\frac{dr}{dt} = \frac{C_r}{r}\left(s - \frac{A}{r} + \frac{r_{dry}^3}{r^3}\right) \tag{2.11}$$

with r being the droplet radius, s the supersaturation. The Kelvin coefficient A

$$A = \frac{2\sigma_{s/a}}{R_v T \rho_w} \tag{2.12}$$

is a function of the local thermodynamic properties of water vapor and liquid water, as long as of the surface tension at the solution-air interface $\sigma_{s/a}$ (Petters & Kreidenweis, 2007). A good estimate for the surface tension is provided by the empiric relation [2]

$$\sigma_{s/a} = 235.6\,(1 - T_{mean0}647.096)^{1.256}\left(1 - 0.625\frac{1-281}{647.096}\right)10^{-3} \tag{2.13}$$

r_{dry} is the dry radius, i.e. the mean volume radius of the dispersed aerosols (e.g. Seinfeld and Pandis, 2016, p. 982). The relative humidity over an acqueous solution droplet with radius r is given by (Petters & Kreidenweis, 2007):

$$RH = \frac{1 - \left(\frac{r_{dry}}{r_{vd}}\right)^3}{1 - \left(\frac{r_{dry}}{r_{vd}}\right)^3(1-\kappa)}\, exp\left(\frac{2\sigma_{s/a}}{R_v T \rho_w r}\right) \tag{2.14}$$

The droplet growth coefficient C_r, given by (e.g. Rogers and Yau, 1996, p. 102)

$$C_r = \left[\left(\frac{L_w}{R_v T} - 1\right)\frac{L_w \rho_w}{K' T} + \frac{\rho_w R_v T}{D' e_s(T)}\right]^{-1} \tag{2.15}$$

is related to the modified thermal conductivity K' and water vapor mass diffusivity D' are computed through the scheme reported by (Ghan et al., 2011; Pruppacher & Klett, 2010)

$$D_\nu^{'} = \frac{D_\nu}{\frac{r}{r + \Delta_\nu} + \frac{D_\nu}{\alpha_c r}\sqrt{\frac{2\pi \mathcal{M}_w}{RT}}} \tag{2.16}$$

[2] A typical value for the surface tension $\sigma_{s/a}$ is $\cong 70 \cdot 10^{-3}$ N/per/meter (see this IAPSW report http://www.iapws.org/relguide/Surf-H2O-2014.pdf).

The modified vapour thermal conductivity is:

$$K_\nu^{'} = \frac{K_a}{\frac{r}{r+\Delta_T} + \frac{K_a}{\alpha_T r \rho_a c_p}\sqrt{\frac{2\pi\mathcal{M}_w}{RT}}} \tag{2.17}$$

Chapter 3

Cloud turbulence

The fact that warm clouds in the lower atmosphere are turbulent should not astound. Devenish et al., 2012 pointed out that any considerable estimate of the Reynolds number in such flows is much higher than the typical critical values for transition. By assuming $u \sim 1\ \mathrm{m\,s^{-1}}$, $L \sim 100$ m and $\nu \sim 10^{-5}\ \mathrm{m^2/s}$ the large scale Reynolds number

$$Re = \frac{UL}{\nu} \tag{3.1}$$

is of the order $\sim 10^7 \div 10^8$. The sharp boundaries of a cloud are the sign of turbulent activity (Raymond A. Shaw, 2003), with turbulent kinetic energy being produced at the large scales near the cloud boundaries by shear and buoyancy-driven instabilities (e.g. Kelvin-Helmoltz and Reyleigh-Taylor instabilities) (Devenish et al., 2012). Values for the longitudinal and transverse structure functions have been computed through several measurement campaigns (e.g. H. Siebert, Gerashchenko, et al., 2010; H. Siebert, Lehmann, and Wendisch, 2006; H. Siebert, Shaw, and Warhaft, 2010) their ratio showing being close to 4/3, as predicted by the Kolmogorov's classical theory for homogeneous and isotropic turbulence (HIT). The measured structure functions also show that intermittency is observed at the small scales, with values for the kurtosis that significantly depart from Gaussian and scaling exponents being close to those predicted by Obukhov's refined similarity hypothesis (H. Siebert, Gerashchenko, et al., 2010). In general, intermittent behavior is associated to very localized yet strong and highly-coherent events whose statistics considerably deviate from the Gaussian turbulent field in the background (Jiménez, Wray, Saffman, & Rogallo, 1993; She, Jackson, & Orszag, 1990). Experimental evidence suggests that these tube-like coherent structures - which are characterized by enormous vorticity - are present in real clouds and could have an impact on cloud microphysics (e.g. Raymond A. Shaw, 2000; Raymond A. Shaw et al., 1998).

Cumulus clouds can extent up to a few kilometers both in the horizontal and vertical directions (Rogers and Yau, 1996, p. 64). However, the typical turbulent

structures are estimated to be somewhat smaller $\sim 10^2$ m. In three-dimensional flows and for sufficiently high Reynolds numbers, turbulent structures are expected the break up and transfer kinetic energy and momentum from large to the small scales through the direct cascade. Following the first similarity hypothesis for stationary HIT, one can estimate the range of spatial scales involved in this process (Monin and Yaglom, 2013, p. 349, Frisch and Kolmogorov, 1995, p. 105)

$$\frac{\ell}{\eta} = Re_\ell^{\frac{3}{4}} \tag{3.2}$$

which is defined by the large scales Reynolds Re_L. The smallest scale that is reached by the cascade, η, is called the Kolmogorov scale. For typical cloud conditions one gets $\eta \sim 10^{-3}$ m (Devenish et al., 2012). The average turbulent kinetic energy (TKE) dissipation rate is assumed to be the same for all scales

$$\varepsilon \sim \frac{U_\ell^3}{\ell}$$

and is expected to be of the order of 10^{-2} m^2/s^3 (or 100 cm^2/s^3). Both large scale velocity and TKE dissipation rate estimates are in good agreement with values provided through aircraft measurements (e.g. MacPherson and Isaac, 1977, Rogers and Yau, 1996 chapter 5 and references therein). Kolmogorov's similarity hypothesis states that - for sufficiently high Reynolds numbers - small scale turbulent motions are isotropic and that the dynamical properties of the universal equilibrium range only depend on the flux of energy through the direct cascade. All directional biases that could be inherited by the large anisotropic scales - where TKE is produced - are lost during the transfer through the energy cascade (Pope, 2000, p. 184). Provided that dissipation is roughly the same for all scales in the inertial subrange

$$\varepsilon \sim \frac{U_\ell^3}{\ell} \sim \frac{u_\eta^3}{\eta} \tag{3.3}$$

the small scales quantities (i.e. scale η, velocity u_η and time τ_η) can be obtained by equation 3.3, by assuming the viscous dissipation to act directly at the end of the cascade, that is

$$Re_\eta = \frac{u_\eta \eta}{\nu} \sim 1$$

One gets

$$\eta \sim \left(\frac{\nu^3}{\varepsilon}\right)^{\frac{1}{4}} \quad u_\eta \sim (\varepsilon\nu)^{\frac{1}{4}} \quad \tau_\eta \sim \left(\frac{\nu}{\varepsilon}\right)^{\frac{1}{2}} \tag{3.4}$$

In stationary HIT, TKE is distributed among the scales in the inertial subrange following the energy spectrum

$$E(\kappa) = C\overline{\varepsilon}^{\frac{2}{3}}\kappa^{-\frac{5}{3}} \tag{3.5}$$

depends only on the average value of ε and the wavenumber κ (Monin and Yaglom, 2013, p. 355.). This is known as Kolmogorov's *five thirds* law.

Another spatial scale, the Taylor microscale λ, is often used in HIT-related studies. The Taylor microscale lies somewhere at the bottom of the inertial subrange, but is much larger than η. It is thus defined as (Tennekes and Lumley, 1972 pp. 67-68)

$$u_{rms} \sim \lambda S_{ij}$$

with S_{ij} being the local strain rate tensor. λ has not a specific physical meaning, but it is commonly related to several phenomena occurring at the small scales. For instance, P. A. Vaillancourt and Yau, 2000 define λ as the "*characteristic length scale of the mean spatial extension of the velocity gradients*" $\lambda^2 \sim u_{rms}^2 \nu/\varepsilon$. The Taylor-based Reynolds number

$$Re_\lambda = \frac{u_{rms}\lambda}{\nu} \tag{3.6}$$

can be interpreted as the ratio between the eddy turnover time of the large scales $\sim \ell/u_{rms} \sim \lambda^2/\nu$ and the time scale of the strain rate fluctuations (Tennekes and Lumley, 1972, p. 68). Typical values of Re_λ are of the order $\sim 10^3$ in stratocumulus and 10^4 in cumulus clouds (Devenish et al., 2012).

Again, turbulent flows are highly intermittent and all estimates for the quantities hitherto discussed - such as ε or those defined in 3.4 - must be interpreted as values averaged over cloud scales. Deviations are expected to become significant at much smaller spatial scales (P. A. Vaillancourt & Yau, 2000).

3.1 In situ measurements

In situ measurements are an important tool for cloud research. Investigating cloud properties is crucial to studying many aspects of cloud turbulence, microphysical properties and evolution. Estimates of many parameters, such as Re_λ, N, the LWC, θ and ε can be derived in such experiments but, unfortunately, the number of studies reporting the results of airborne measurments is still relatively small (Devenish et al., 2012). The set-up of numerical simulations must rely on the available data in order to mimic real cloud conditions. In many cases, the observation and analysis of cloud droplets has been performed using the Forward Scattering Spectrometer Probe (FSSP), and ground-based holographic imagery (HODAR) (P. A. Vaillancourt & Yau, 2000).

Some pioneering experiments were conducted by MacPherson and Isaac, 1977 and Schemenauer, MacPherson, Isaac, and Strapp, 1980 over Canada and Northwest United States. Some of these results were also reviewed in Rogers and Yau, 1996. Two equipped aircraft were flown through several stratocumulus and cumulus clouds.

A large amount of data was provided. In both studies, cloud base lied above 2000 meters of altitude (above freezing level) and the recorded static temperature was negative. The amount of detected liquid water (~ 1 g/m^3) content was observed to increase with height, but was still lower than that predicted from the adiabatic theory. Droplet concentration ($\sim 200 \div 500$ cm^{-3}) was shown to vary significantly with the mean radius, being higher for small radii and lower for relatively large droplets. These studies suggest that also the TKE dissipation rate ($\sim 10 \div 10^2$ cm^2/s^3) and the rms velocity ($\sim 0.1 \div 1$ m s^{-1}) may slightly increase with height above the cloud base, hence reaching a peak at cloud top. As a result of processes involving droplet growth during adiabatic ascent, the peaks of the spectral DSD were observed to shift to higher values with increasing altitude (Schemenauer et al., 1980, Rogers and Yau, 1996, pp. 65-69).

Rangno and Hobbs, 2005 sampled cumuliform clouds from a Convair-580 aircraft in the Marshall Islands. In their study, they also investigated the properties of small cumulus and cumulonimbus in which no subfreezing region was observed. In some cases, the lowest recorder temperature was of 9 and 10 °C. The average droplet concentration of these marine clouds barely exceeded 90 cm^{-3}. H. Siebert et al., 2006 estimated $\varepsilon \sim 10^{-3}$ m^2/s^3 and $Re_\lambda = 40000$ for cumulus humilis and shallow cumulus clouds. Burnet and Brenguier, 2007 investigated the thermodynamical and microphysical properties of warm marine cumulus and stratocumulus clouds. Droplet concentration was reported to be in the order of $200 \div 400$ cm^{-3} and the MVD was equal to 15 µm for the stratocumulus and 30 µm for the cumulus clouds. The *adiabatic* liquid water mixing ratio $q_{la} = LWC_a/\rho_a$[1] was found to be 0.7 in the stratocumulus case and much higher (~ 4) for the cumulus clouds. In their work on trade-wind cumuli, Gerber, Fricks, Jensen, and Hudson, 2008 reported $\varepsilon \sim 10$ cm^2/s^3, fluctuations of the vertical velocity $\sigma_w \sim 1$ m s^{-1}, $N \cong 10^2$ cm^{-3} and MVD ~ 10 µm. However, droplet spectra resulted to remain approximately constant with height above the LCL (lifting condensation level). Lehmann et al., 2009 obtained similar results using the ACTOS payload, an helicopter-tethered probe, with $\varepsilon \lesssim 10$ cm^2/s^3. Also H. Siebert, Shaw, and Warhaft, 2010 estimated relatively low values of $\epsilon \sim 1$ cm^2/s^3.

3.2 Water drops and interphase coupling

Cloud flows fall under the category of multiphase turbulent flows. Air and water vapor are the main constituents of the gaseous medium in which water drops and CCN (aerosols) are immersed. The air-water vapor field is referred to as the *carrier*

[1] q_{la} and LWC_a denote adiabatic quantities, whereas ρ_a refers to the ambient air, carrier flow density.

flow and liquid and solid particles are the the *dispersed phase*. The distributed particles can collide, coalesce, undergo phase transition or break-up. It is important to determine to what extent the carrier flow and the dispersed phase can interact with each other through mass, momentum and energy coupling. Hence, a few non-dimensional parameters are used to estimate the relative influence of the carrier flow over the dispersed phase and vice-versa (Balachandar & Eaton, 2010; P. A. Vaillancourt & Yau, 2000). The mass loading Φ_m is defined as the ratio of the total mass of the dispersed phase and the total mass of the carrier phase. Similarly, the volume fraction Φ_v accounts for the volume that is occupied my the dispersed phase relatively to the total volume of the fluid flow. The ratio D_v/η is used as a reference to determine whether the characteristic spatial magnitude of the carrier flow and the dispersed particles are well separated. Finally, the Stokes number St (i.e. the ratio between the droplet inertial response time and the Kolmogorov time) is used to quantify the sensitivity of a dispersed particle to the perturbations of the carrier flow.

In general, values of the LWC of the order $\lesssim 1$ g/m^3 are observed in warm clouds[2], thus implying small values for both Φ_m and Φ_v. This allows to neglect the effects produced by the droplet distribution on the turbulent flow to a good approximation. In addition, the majority of cloud drops has a mean radius of a few micrometers, well below η, thus ensuring a good separation of scales. Under these conditions, the effects of structures of all turbulent scales on a single droplet can be described analitically. The force exerted by the carrier flow on a small spherical droplet moving in the Stokes regime $Re_d \lesssim 1$ is thus given by (e.g. Raymond A. Shaw, 2003, Balachandar and Eaton, 2010 and references therein)

$$\rho_w \Omega_d \frac{D\boldsymbol{v}}{Dt} = \underbrace{6\pi\mu r\left(\boldsymbol{V}-\boldsymbol{v}\right)}_{\text{Stokes drag}} + \underbrace{\frac{1}{2}\rho_a\Omega_d\left(\dot{\boldsymbol{V}}-\dot{\boldsymbol{v}}\right)}_{\text{added mass}} + \underbrace{6r^2\sqrt{\pi\rho_a\mu}\int_o^t \frac{\dot{\boldsymbol{V}}(t')-\dot{\boldsymbol{v}}(t')}{\sqrt{t-t'}}dt'}_{\text{Basset's history force}} + \\ + \underbrace{\rho_w\Omega_d\boldsymbol{g}}_{\text{gravity}} + \underbrace{\rho_a\Omega_d\left(\dot{\boldsymbol{V}}-\boldsymbol{g}\right)}_{\text{shear stress and buoyancy}} \tag{3.7}$$

with r begin the droplet radius, $\Omega_d = 4/3\pi r^3$ the droplet volume, $\boldsymbol{V}$ the flow velocity, $\boldsymbol{v}$ the droplet velocity, $\mu = \nu\rho_a$ the dynamic viscosity of air. The Faxén term may also be considered. In fact, under the conditions that are considered in this work most of the terms in equation such as the added mass, Basset's history force, Faxén's and the shear stress terms can be neglected (Götzfried, Kumar, Shaw, & Schumacher, 2017). This leads for the widely used expression for the droplet

[2]See Rogers and Yau, 1996, p. 68 and references therein, Lehmann et al., 2009.

acceleration

$$\frac{D\boldsymbol{v}}{Dt} = \frac{9}{2}\frac{\mu}{\rho_w r^2}(\boldsymbol{V} - \boldsymbol{v}) + \left(1 - \frac{\rho_a}{\rho_w}\right)\boldsymbol{g} \tag{3.8}$$

where $\tau_d = \frac{2}{9}\frac{\rho_w r^2}{\mu}$ is the droplet inertial response time. According to equation 3.8 small droplets will respond more readily to the flow comparing to large ones. τ_p determines the particle inertial response to the carrier flow that is exerted by the Stokes drag. The non-dimensional parameter that is used to quantify the droplet response to the smallest structures of the turbulent flow is the Stokes number St

$$St = \frac{\tau_d}{\tau_\eta} \tag{3.9}$$

For $St \to 0$ the particle field acts as a passive scalar, while in the limit $St \to \infty$ (but under the hypothesis of $d \ll \eta$) the particle does not interact effectively with the flow. τ_d only depends on the fluid properties (μ) and on the droplet radius, whereas St is defined as a function of both τ_d and τ_η, which scales as $1/\sqrt{\varepsilon}$.

A simple analytical solution of equation 3.4 can be found by neglecting relative motion of the carrier flow and buoyancy

$$\frac{D\boldsymbol{v}}{Dt} \cong -\frac{\boldsymbol{v}}{\tau_d} + \boldsymbol{g}$$

that is

$$\boldsymbol{v}(t) = \underbrace{\boldsymbol{g}\tau_d}_{\boldsymbol{V_T}}\left[1 - exp\left(-\frac{t - t_0}{\tau_d}\right)\right]$$

with $\boldsymbol{V}_T = \tau_d \boldsymbol{g}$ being the droplet terminal velocity of a particle with zero initial velocity that settles through the fluid in a non-turbulent environment. It is often normalized with respect to the local Kolmogorov velocity v_η

$$Sv = \frac{V_T}{v_\eta}$$

which can be interpreted as the ratio between τ_η and the time taken by a droplet to settle across a small scale eddy η/V_T. The ratio of St to Sv is, not surprisingly, the Kolmogorov-scale Froude number Fr_η

$$\frac{St}{Sv} = Fr_\eta$$

(Devenish et al., 2012) which should not be confused with the internal Froude number defined in 2.9. The small scale Froude number Fr_η

$$Fr_\eta = \frac{u_\eta^2}{g\eta} \sim \frac{\varepsilon^{\frac{3}{4}}}{g\nu^{\frac{1}{4}}} \tag{3.10}$$

expresses the magnitude of the turbulent motions relative to gravity. The Froude number scales with the TKE dissipation rate ε, meaning that as turbulence intensity increases droplets are less likely to settle. For typical levels of TKE dissipation rate that found in clouds $Fr_\eta \sim 10^{-2} \div 10^{-1}$ and droplet sedimentation is expected to be the predominant phenomenon.

3.2.1 Preferential concentration

Droplet acceleration in equations 3.7 and 3.8 is expressed with the lagrangian derivative. The reason for doing this is that it may be convenient to treat the droplet phase as a continuum with variable density N, N being the droplet concentration. It was shown in the previous section that as the turbulence intensity increases, so does the Froude number. Small scale vortices become more intense and can interact effectively with the particle phase. Now, it is important to understand the effect of such interaction. Following Raymond A. Shaw, 2003, if one solves equation 3.8 under the assumption of small τ_d and takes the divergence then gets

$$\nabla \cdot \boldsymbol{v} \cong -\tau_d \nabla \cdot \frac{D\boldsymbol{V}}{Dt} + \tau_d \nabla \cdot \boldsymbol{g}$$

The gravity field $\boldsymbol{g}$ is assumed to be locally solenoidal and the carrier flow is supposed to be incompressible. The latter equation becomes

$$\nabla \cdot \boldsymbol{v} \cong -\tau_d \nabla \cdot (\boldsymbol{V} \cdot \nabla \boldsymbol{V}) \tag{3.11}$$

Increasing values of $\nabla \cdot \boldsymbol{v}$ may thus account for increasing droplet concentration N

$$\frac{DN}{Dt} = -N \nabla \cdot \boldsymbol{v}$$

It can be shown (see Devenish et al., 2012; Raymond A. Shaw, 2003 and references therein) that droplets preferentially segregate in regions of high dissipation and tend to be ejected out of regions of high vorticity. Equation 3.11 can be expressed as a function of the Stokes number St of the droplets (Devenish et al., 2012)

$$\nabla \cdot \boldsymbol{v} \sim -St\,(\varepsilon - \mathcal{E})$$

This phenomenon is known as preferential concentration or droplet clustering and is expected to have an impact on droplet growth by collision-coalescence. However, its role on droplet growth by condensation in real clouds is still a matter of discussion (Grabowski & Vaillancourt, 1999; Raymond A. Shaw, 2000; Raymond A. Shaw et al., 1998).

3.3 Entrainment and interfacial mixing

Entrainment-mixing processes have been regarded as a key to understanding the evolution of cloud-droplet spectra and the conundrum of warm rain initiation (Khain, Pinsky, & Magaritz-Ronen, 2018; Lu, Liu, & Niu, 2011). Entrainment occurs continuously as ambient air is advected into the cloud; the opposite process, detrainment, is the transfer of cloudy air to the external environment. Turbulent eddies that are present at the cloud interface engulf blobs of external air that are subsequently dispersed across it. The blobs are stretched into filaments and subsequently stirred. Entrainment-mixing is often described as three-stage processes (e.g. Dimotakis, 2005; Lu et al., 2018; Tölle and Krueger, 2014), the first stage being the engulfment of external air by the large eddies. In the second phase (known as *turbulent stirring*) the direct cascade provides larger and larger interfacial areas between the filaments. Eventually, the entrained substance can diffuse effectively at the small scales. The whole process is regarded as a pretty complex type of turbulent mixing, featuring momentum and energy transfers, phase changes and positive feedbacks (coupling) between the dispersed particles (that is, the water drops) and the carrier flow at the small scales. In their early studies Latham and Reed, 1977 and Baker and Latham, 1979 (see also references therein) provided a yet "*simplistic*" (sic) description, by distinguishing two conceptual types of mixing between a parcel of cloudy air and the environment. By relying on experimental data, they noticed that the entrained subsaturated air could affect the growth of all droplets in the mixed parcel or just of a part of them. Mixing can be homogeneous when all droplets are subject to the same degree of saturation deficit and shrink at a comparable rate (equation 1.1). The opposite occurs when only a portion of the droplet population is affected by the external air. In this case a few influenced drops will completely evaporate, the mean radius will remain constant and the total number of liquid particles will decrease. The mixing that results is inhomogeneous (Devenish et al., 2012). Both homogeneous and inhomogeneous mixing are ideal concepts, each one representing a path to reduce the local liquid water content by keeping constant either the droplet concentration or the mean volume radius (MVD).

Mixing of cloudy air with subsaturated air is often represented through a mixing diagram (see figure 3.1). The axes show droplet concentration and mean volume normalized with respect to their adiabatic values. Every mixing path starts at point (1,1) that represents the adiabatic parcel at its initial state. The possible paths depend on the relative humidity of the entrained air. The inhomogeneous limit is represented by the horizontal line (constant mean volume), while the purely inhomogeneous mixing can be represented by a vertical line (constant droplet concentration, not shown). For increasing relative humidities of the entrained air the process undergoes progressive transition from being purely homogeneous to

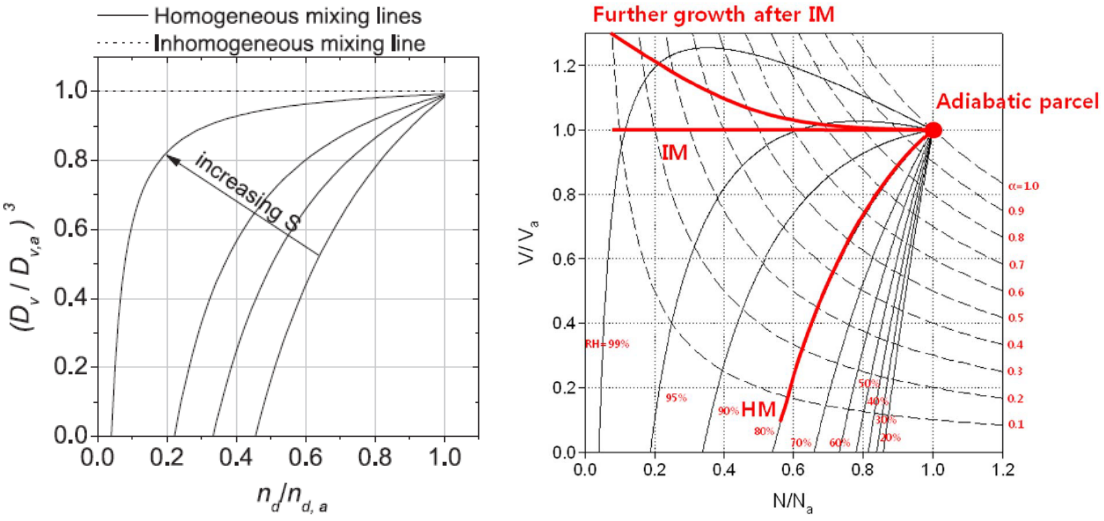

Figure 3.1: Examples of schematic $r - N$ mixing diagrams (left picture from Lehmann, Siebert, and Shaw, 2009, right one from Yum et al., 2015). The example to the right also shows a possible path representing droplet growth beyond the inhomogeneous mixing limit (super-adiabatic growth) that is not considered here.

being extremely inhomogeneous.

By considering spherical droplets, we know that both droplet concentration N and mean volume radius r_v^3 define the liquid water content

$$LWC = \frac{4}{3}\pi\rho_w \overline{r}^3 N \tag{3.12}$$

which is reduced during dilution (Gerber et al., 2008). The ratio of the final LWC with respect to its initial (adiabatic) value

$$\alpha = \frac{LWC}{LWC_a} = \frac{N}{N_a}\frac{r_v^3}{r_{va}^3}$$

is represented by a rectangular hyperbola on the mixing diagram (Burnet & Brenguier, 2007; Pawlowska, Brenguier, & Burnet, 2000). Scattered samples of local concentrations and mean volumes can be plotted over such diagrams in order to estimate the static (i.e. istantaneous) behavior of an entrainment-mixing process (Burnet & Brenguier, 2007), which is sometimes considered a limitation. (Baker & Latham, 1979) also suggested that the mixing behavior is determined by the local time scales for turbulence, droplet growth and diffusion. In the homogeneous limit, the turbulent time scales are negligible with respect to the microphysics time scales. All filaments are rapidly stirred and all droplets experience the same saturation ratio, hence growing or shrinking at the same rate. On the other hand,

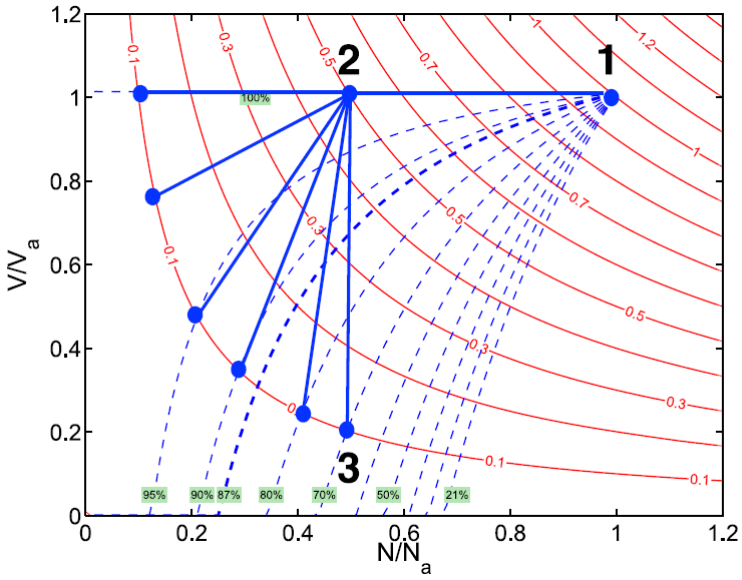

Figure 3.2: The three phases of the entrainment-mixing process (Dimotakis, 2005) in the $r - N$ diagram. The mixing regime determines the position of the third-stage point (picture taken from Tölle and Krueger, 2014).

turbulent eddies may be slow compared to the local microphysics, which could evolve at a faster rate. Some droplets will completely evaporate, while others will not be affected at all, making the mixing extremely inhomogeneous. (Burnet & Brenguier, 2007) conducted airborne measurements of top mixing in warm marine cumulus and stratocumulus clouds. The estimated turbulent time scales and evaporation time scales showed good agreement with the resulting scattered plots, thus supporting the time-scales hypothesis. (Andrejczuk, Grabowski, Malinowski, & Smolarkiewicz, 2004, 2009) ran a series of direct numerical simulations and found a robust correlation between the slope of the plots in the mixing diagrams in figure 3.1 and the ratio of the turbulent mixing and droplet evaporation temporal scales when the latter ranged between $10^{-1} \div 10^{1}$. The ratio between the turbulence and the microphysical time-scales is often used as a simple parametrization to quantify the mixing regime (Devenish et al., 2012; Lu et al., 2018 and references therein) and, by analogy with reacting flows (Dimotakis, 2005) an appropriate Damköhler number

$$Da = \frac{\tau_{turbulence}}{\tau_{microphysics}} \tag{3.13}$$

is defined. For $Da \ll 1$ the mixing process is expected to lie in the homogeneous regime, for $Da \gg 1$ in the inhomogeneous one (Devenish et al., 2012).

As mentioned earlier, the picture provided by the $r - N$ plots being static results

in a considerable limitation, thus making their physical interpretation difficult. Scattered plots obtained through in situ measurements do not give any information related to the state of the evolution of such processes (Burnet & Brenguier, 2007). (Khain et al., 2018) pointed out that interpretation of such diagrams may be misleading in defining the mixing regime. Yet, they also argued that a series made of several static diagrams can effectively describe the transient evolution of an entrainment-mixing process.

The curves in the $r - N$ diagram can be obtained by solving the equations for mass and energy conservation for water vapor and liquid water in the mixing parcel. The mixing process takes place at constant relative humidity for both the entrained cloudy and clear air and under isobaric conditions. The mixing parcel is supposed to be adiabatic, the cloudy air to be saturated (that is $RH_c = 1$). One gets (Yang et al., 2016)

$$\begin{cases} m_{vi} + m_{ai} + m_{li} = m_{vf,m} + m_{af,m} + m_{lf,m} \\ T_{vi} - \dfrac{L_w}{c_p} q_{li} = T_{vf,m} - \dfrac{L_w}{c_p} q_{lf,m} \end{cases}$$

Subscripts refer to liquid, vapor and air phases in their initial i and final f conditions. m stands for mixing. By further assuming that the mixing takes place in a fixed volume and that the carrier flow is incompressible (i.e. $\nabla \cdot \boldsymbol{V} = 0$ and ρ_a is a non-zero constant) we can divide by ρ_a and get (Gerber et al., 2008; Lehmann et al., 2009)

$$q_{vi} + q_{li} = q_{vf} + q_{lf}$$

Under conditions, a fixed fraction χ of cloudy air entrains a fixed fraction $1 - \chi$ of environmental air:

$$\begin{cases} (q_{vi} + q_{li})\,\chi + q_{ve}\,(1-\chi) = q_{vf,m} + q_{lf,m} \\ \left(T_{vi} - \dfrac{L_w}{c_p} q_{li}\right)\chi + (1-\chi)\,T_e = T_{vf,m} - \dfrac{L_w}{c_p} q_{lf,m} \end{cases}$$

q_{vi} is supposed to be saturated at and $\cong q_{vs}\,(T_c)$. Subscripts c and e denote the cloud and the environment quantities respectively. The environmental air vapor mass ratio is a function of the ambient temperature and saturation deficit

$$q_{ve} = q_{vs}\,(T_e)\ RH_e$$

with T_c, T_e and RH_e being assumed constant to a good approximation throughout the process. The final conditions are given by (Gerber et al., 2008; Yum et al., 2015)

$$\begin{cases} q_{lf,m} = \chi\,(q_{li} - q_{vs}\,(T_e)\,RH_e + q_{vs}\,(T_c)) + q_{vs}\,(T_e)\,RH_e - q_{vs}\,(T_{f,m}) \\ T_{f,m} = \chi\left(T_c - T_e - q_{lc}\dfrac{L_w}{c_p}\right) + T_e + q_{lf,m}\dfrac{L_w}{c_p} \end{cases} \tag{3.14}$$

The equations in the system 3.14 are non-linearly coupled since they introduce the Clausius-Clapeyron equation 2.3 and can be solved using an iterative scheme for values of χ ranging between 0 and 1 (Yum et al., 2015). The droplet concentration of the final mixture is homogeneously reduced by a factor χ with respect to its initial adiabatic value

$$N = \chi N_a \tag{3.15}$$

The liquid water content of the final mixture is homogeneously reduced by a factor α with respect to its initial adiabatic value and is given by (Gerber et al., 2008)

$$LWC_{f,m} = \rho_a \, q_{lf,m} \tag{3.16}$$

The final droplet mean volume is given by

$$\overline{r}^3 = \frac{LWC_f}{\frac{4}{3}\pi\rho_w N} \tag{3.17}$$

The $r - N$ curves can be plotted by solving the system 3.14 for different values of RH_e. As RH_e increases, the curves will tend to the inhomogeneous mixing line, shifting to the homogeneous limit only for small χ (Devenish et al., 2012). In the case of isobaric mixing, the initial values of N, LWC and $\overline{r}^3$ are represented by the adiabatic values. The final mixing diagram is shown in figure 3.3.

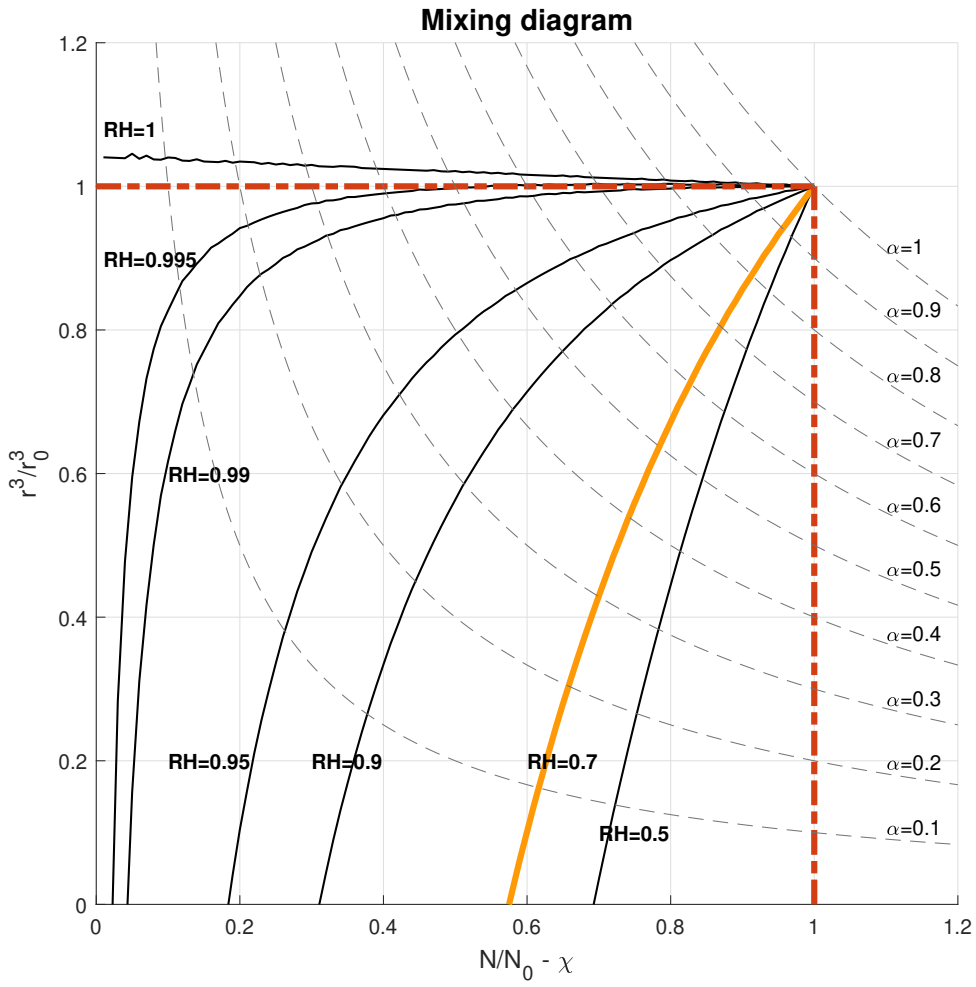

Figure 3.3: Different solutions for the system 3.14. The highlighted orange curve is drawn for the $RH_e = 0.7$ case. Little super-adiabatic growth is predicted for curves drawn for $RH = 0.99$, $RH = 0.995$. Super-adiabatic growth for $RH = 1$ results in good agreement with the diagrams represented by (Lehmann, Siebert, & Shaw, 2009).

Chapter 4

On the role of temporal scales in cloud physics

A number of different temporal scales are used to characterize droplet growth in turbulent clouds and to seek the most appropriate parameterization. Temporal scales determine how fast physical processes are. When a number of interacting processes take place in a physical system it is often important to determine which one will occur more readily and whose effect will be the most impactful on cloud evolution. The comparison of several time-scales allows to estimate which of the many processes involved occurs within a shorter time or with a higher frequency. For instance (Sedunov, 1974) solved a set of three convection-diffusion equations and defined three time-scales in order to characterize the diffusion of water vapor at the surface of an isolated droplet and temperature inside and outside the droplet. All the three time scales were a function of the droplet surface (which is $\propto r^2$) and the thermal and mass diffusivities of liquid water, water vapor and ambient air (Devenish et al., 2012). P. A. Vaillancourt, Yau, and Grabowski, 2001 estimated shorter relaxation times for the ambient phase (i.e. water vapor and outside temperature) than for the temperature of the liquid water. Following Kinzer and Gunn, 1951, P. A. Vaillancourt et al., 2001 also pointed out that another time-scale should be taken into account whenever the droplet surface temperature (also known as the psychrometric temperature) is not assumed to remain the same. Release and absorption of latent heat during condensation and evaporation at the droplet surface can change the local temperature. The psychrometric temperature will subsequently relax to a quasi-steady state value in a time of the order of

$$\tau_{psychro} = \frac{c_w \rho_w r^2}{3K_a \left(1 + \frac{\rho_{vs} D_v L_w^2}{K_a R_v T^2}\right)} \tag{4.1}$$

The psychrometric time-scale τ_{psycho} increases with increasing radii and results to be among the slowest diffusive time-scales even for the relatively small droplets. Anyway P. A. Vaillancourt et al., 2001 argued that for droplet with radii $\lesssim 20$ µm and for relatively low TKE dissipation rates - such as those found in shallow cumulus and stratocumulus clouds $\varepsilon \lesssim 100$ cm^2/s^3 - the psychrometric temperature will relax to its steady-state value rapidly enough to not to interact with the small scale turbulence. The Kolmogorov time scale is the faster temporal scale that characterizes the motion of small turbulent structures in the dissipative range and it is shown (equation 3.4) to inversely scale with the local TKE dissipation rate. If $\tau_{psychro}$ and the diffusive time scales are much faster even if compared to the fastest time scale describing the local turbulent structures, τ_η, then one would be tempted to treat those microphysical processes as instantaneous and to focus on the evolution of turbulence alone. In general, it is usually assumed that processes that are completed within a shorter time are less prone to interaction with slower physical phenomena occurring in the same place.

Time scales are commonly used in entrainment-mixing studies to determine the nature of the mixing regime and its impact on droplet growth by condensation (Baker, Corbin, & Latham, 1980; Baker & Latham, 1979; Burnet & Brenguier, 2007; Lehmann et al., 2009). As reported in chapter 3, the time scale dependent Stokes number determines the effectiveness of droplet clustering, a phenomenon which is expected to enhance the collision rate between preferentially concentrated droplets (e.g. Raymond A. Shaw, 2003; P. A. Vaillancourt and Yau, 2000; P. A. Vaillancourt, Yau, Bartello, and Grabowski, 2002; P. A. Vaillancourt et al., 2001. The impact of small scale turbulence and intermittency on condensational growth has been the object of several studies (e.g. Grabowski and Vaillancourt, 1999; Pinsky, Khain, and Levin, 1999; Raymond A. Shaw, 2000; Raymond A. Shaw et al., 1998, 1999) which discussed the role of both the diffusion time scales and the lifetime of coherent structures on droplet growth by condensation (Devenish et al., 2012).

4.1 Temporal scales in entrainment-mixing processes

(Baker et al., 1980; Baker & Latham, 1979) first suggested that temporal scales may be a good way to parameterize the microphysical response to turbulent interfacial mixing. Observational studies such as those lead by (Burnet & Brenguier, 2007) and (Lehmann et al., 2009) investigated the parameterization of homogeneous and inhomogeneous mixing conditions through the estimated local temporal scales. The Damköhler number 3.13 - defined as the ratio of the turbulence and microphysical time scales - is widely used to quantify the homogeneous mixing degree Ψ that has

been first introduced by (Lu, Liu, Niu, Krueger, & Wagner, 2013) (!!! also check morrison and graboski 2008). (Andrejczuk et al., 2009) found a high correlation between the slope of the mixing diagram and the local value of Da. The turbulent time scale that is used to compute Da is usually identified with the eddy turnover time τ_ℓ (Lu et al., 2018) which is defined as the ratio between the characteristic eddy length scale and the local eddy velocity. For the largest scales of the flow one has

$$\tau_\ell \cong \frac{\ell}{u_{rms}} \sim \frac{\ell}{\sqrt{\mathcal{K}}} \tag{4.2}$$

with ℓ being the integral scale and

$$u_{rms} = \frac{2}{3}\sqrt{\mathcal{K}}$$

$\mathcal{K}$ being the kinetic energy per mass unit of the flow. The denominator of Da only depends on the local microphysics whereas different eddy turnover times are defined for different spatial scales of the turbulent structures. As pointed out by (Kumar et al., 2013), a set of Damköhler numbers can be defined for all the scales lying in the inertial subrange

$$Da_\eta \ll Da \ll Da_\ell$$

For turbulence and microphysical times being of the same order (i.e. $Da \sim 1$) a transition or critical length scale L^* can be defined

$$L^* = \sqrt{\varepsilon \tau^3_{microphysics}} \tag{4.3}$$

larger-than-L^* vortices are expected to foster inhomogeneous mixing. If the transition length scale lies somewhere within the spectrum covered in the inertial subrange, then both homogeneous and inhomogeneous mixing will likely take place in the same turbulent system (Devenish et al., 2012). For warm cloud conditions, the transition length scale is of the order of several meters. Kumar et al., 2018 have run direct numerical simulations of a cloud-clear air interface and found that the width of the computational domain, for constant droplet concentration and droplet mean radius has a considerable impact on the nature of the mixing and on the relative dispersion of the droplet radius PDF that arises.

Several studies have identified the microphysical time scale with the evaporation time, the phase relaxation time or the reaction time (e.g. Andrejczuk et al., 2009; Baker and Latham, 1979; Chandrakar et al., 2016; Kumar et al., 2013; Lehmann et al., 2009; Lu et al., 2011). The effects of these time scales, as long as their correlation with the local homogeneous mixing degree Ψ, have been examined in a comprehensive work by (Lu et al., 2018).

4.1.1 Evaporation time

The evaporation time scale is defined as the time that it takes for a droplet to completely evaporate in a constant-RH environment. By considering the simplified model for droplet growth without taking into account the Kelvin and Raoult effects (equation 2.11) one gets

$$\frac{dr^2}{dt} \cong 2C_r s$$

if the droplet is kept in a subsaturated environment at a constant RH (that is, a constant supersaturation or saturation deficit $s_0 = RH_0 - 1$) the above equation can be integrated

$$\int_0^{\tau_{evap}} dt = \int_{r_0}^{0} \frac{dr^2}{2C_r s_0}$$

giving

$$\tau_{evap} = -\frac{r_0^2}{2C_r s_0} \tag{4.4}$$

with r_0 being the initial radius, s_0 the saturation deficit, C_r the droplet growth coefficient 2.15.

The evaporation time is defined for droplets loitering in subsaturated regions and does not account for variable supersaturation, nor for the influence of Kelvin and Raoult effect, which both become important for small spherical droplets. However, it's been widely used to (e.g. (Andrejczuk et al., 2009; Baker et al., 1980; Burnet & Brenguier, 2007)) to define the Damköhler number Da.

4.1.2 Phase relaxation time

The supersaturation equation in absence of updraughts and for isobaric mixing conditions reduces in the form 2.8

$$\frac{ds}{dt} \cong -\frac{C_v}{\rho_{sv}} = -\frac{1}{\rho_{sv}} \frac{1}{V_{x,\delta}} \sum_{x_k \in \Omega_{x,\delta}} \frac{dm_k}{dt}$$

the condensation rate C_v depends on the mass variation of all the droplets contained in the volume $\Omega_{x,\delta}$. Assuming all droplets are relatively small ($\lesssim$ 50 µm) and spherical, it is easy to find that

$$\frac{dm_k}{dt} = \frac{4}{3}\pi\rho_w 3r_k^2 \frac{dr_k}{dt}$$

and, by recalling equations 1.1 and 2.11

$$r_k \frac{dr_k}{dt} \cong C_{rk} s$$

One can therefore express the temporal evolution of supersaturation as a function of supersaturation itself. The supersaturation equation 2.7 can be thereby resolved by separation of variables, and takes the form

$$\frac{ds}{dt} \cong -\underbrace{\frac{1}{\rho_{sv}} \frac{1}{\Omega_{x,\delta}} 4\pi\rho_w \sum_{x_k \in \Omega_{x,\delta}} r_k C_{rk}}_{\tau_{phase}^{-1}} \; s \tag{4.5}$$

that is (Devenish et al., 2012)

$$\frac{ds}{dt} = -\frac{s}{\tau_{phase}}$$

The phase relaxation time τ_{phase} modulates the intensity of the overall source or sink of supersaturation due to the contribution of all the spherical droplets that are enclosed in a finite volume of space. By solving the simplified form of the supersaturation equation by separation of variables one gets

$$\int_{s_0}^{s} \frac{ds}{s} = -\int_{0}^{t} \frac{dt}{\tau_{phase}}$$

and

$$ln\frac{s}{s_0} = -\frac{t}{\tau_{phase}}$$

If both droplet concentration and mean radius are considered constant to a good approximation, then after a time $t = \tau_{phase}$ the local supersaturation will have dropped by a factor $1/e$, reaching the 37% of its initial value. Supersaturation will relax more readily in regions with higher droplet concentration and larger mean droplet radius.

The phase relaxation time has been widely used in cloud physics (Lu et al., 2018). For a parcel of a warm cloud in vertical motion in a steady updraft Korolev and Mazin, 2003 found a solution of the supersaturation equation for constant droplet sizes under the quasi-steady approximation. They found that the fluctuating supersaturation field relaxes to its quasi-steady state value s_{qs} in a time of the order of τ_{phase}. They also discussed the behavior of supersaturation fluctuations to due droplet concentration in the context of a turbulent environment in which turbulent fluctuations also appear. To do so, they defined τ_{phase} as the microphysical time scale. A similar approach was used in the observational study of the birth of shallow cumulus clouds by Holger Siebert and Shaw, 2017. The authors argued that for low Da (that is, for large τ_{phase}) supersaturation fluctuations due to turbulent mixing were weakly buffered by the droplet growth over the typical eddy turnover time. Since the growth of a droplet is defined by its *supersaturation history* (see equation

1.1 and the introduction in Burnet and Brenguier, 2007) the slow microphysics ($Da \ll 1$) regime was expected to foster spectral broadening. This is consistent with the results of the laboratory experiments conducted by Chandrakar et al., 2016. In this experiment, steady-state Rayleigh-Bénard convection was forced in a moist environment confined in a cylindrical chamber. Dry aerosols were injected at constant rates. In the limit of relatively low aerosol/droplet concentration, the droplet spectra was observed to broaden significantly following the relation

$$\frac{d\sigma_{r^2}^2}{dt} = \frac{8C_r^2\sigma_{s0}^2\tau_L}{(1+Da)^2}$$

Saturation time

Lu et al., 2018 pointed out that one of the limitations of the phase relaxation time is that it only provides information for the relative behavior of the supersaturation, regardless of the initial value of the relative humidity. The initial relative humidity is a crucial parameter in entrainment-mixing studies (as seen in chapter 3). To overcome this limitations, Lu et al., 2018 introduced a saturation time τ_{satu} which is defined as the time taken by the supersaturation to reach the final value of -0.005 parting from $s_0 < 0$. τ_{satu} is proportional to τ_{phase}:

$$\tau_{satu} = \tau_{phase} ln \frac{s_0}{-0.005} \tag{4.6}$$

4.1.3 Reaction time

The evaporation time is computed assuming constant relative humidity, while the phase relaxation time assumes constant $N\overline{r}$, that is the first moment of the droplet distribution (Rogers and Yau, 1996, pp. 110-114, Khvorostyanov and Curry, 2014, pp. 144-148). These limitations were pointed out in the observational study by Lehmann et al., 2009. They found that measured values of τ_{evap} and τ_{phase} could differ significantly. In order to understand which was the best time scale to define the microphysics regime, they introduced a reaction time scale τ_{react} which they defined as the elapsed time for complete evaporation ($\tau_{react,ev}$) or for the saturation deficit to reach -0.005 when both droplet growth and supersaturation evolution are taken into account (Lehmann et al., 2009; Lu et al., 2018)

$$\begin{cases} \dfrac{dr^2}{dt} \cong 2C_r s \\ \dfrac{ds}{dt} \cong -\dfrac{s}{\tau_{phase}} \end{cases} \tag{4.7}$$

They found that the reaction time scale was close to the smaller of τ_{phase} and τ_{evap}.

Chapter 5

Direct numerical simulations of a cloud-clear air interface

The aim of direct numerical simulations (DNS) codes is to reproduce the evolution of a turbulent flow field by resolving the Navier Stokes equations for all the scales that are encompassed by the energy cascade. To that end, the computational domain must be built up so that both its global extent and grid resolution allow to reconstruct the largest and the smallest structures of the flow together. Provided that appropriate initial and boundary conditions are adopted along with a suitable and fitting mathematical model, the DNS approach guarantees the highest level of accuracy among modern simulation techniques (Pope, 2000, p. 344).

However, as a result of the enormous amount of computational resources involved, their use is limited to relatively low-to-moderate Reynolds numbers. This aspect represents a major drawback since clouds typically extend over hundreds of meters, with Re of the order of 10^7. The major problem is that, by simulating a small cloud parcel one is forced to neglect the effect of the large scale vortices, whose dynamics are coupled with the small scale ones. Also, the initial conditions of these numerical experiments are usually idealized and far from reality. In this regard, Andrejczuk et al., 2004 pointed out that the spirit of DNS - whose results should always be extrapolated carefully to laboratory or real cloud conditions - is to focus more on the qualitative behavior of the transient, rather than to provide an exact numerical description of complex single or multiphase fluid phenomena.

In spite of these issues, DNS have been widely used in the past twenty years to investigate the role played by small scale turbulence on cloud physics (Gao et al., 2018). P. A. Vaillancourt et al., 2002; P. A. Vaillancourt et al., 2001 conducted numerical experiments to study a droplet-seeded turbulent environment, droplet

clustering and gravitational settling. They adopted the Boussinesq approximation along with a lagrangian tracking system for the dispersed droplets. Andrejczuk et al., 2004, 2006, 2009 studied cloud-clear air mixing on cube-shaped domains at moderate Reynolds numbers. Their simulations did not include a lagrangian description of the droplets trajectories and the standard bulk approximation was assumed instead. Lanotte, Seminara, and Toschi, 2009 ran two series of simulations over cubic domains. Their setup included a lagrangian tracker for the droplet phase and an equation for the evolution of supersaturation (the Twomey model) which has also been used by Sardina, Picano, Brandt, and Caballero, 2015, 18. Kumar et al., 2013 ran DNS to study the relaxation process of the droplet phase following the entrainment of dry air in a cloudy environment, but did not take into account the temperature field and the response of the system to evaporative cooling. Their analysis followed the case of horizontal shearless mixing across a cloud-clear air interface parallel to the direction of gravity. Kumar et al., 2018; Kumar et al., 2014 included the evolution of internal energy and analysed the droplet trajectories in the mixing diagrams and the effect of the domain size on the Damköhler number. In these works, the initial turbulent state included a central cloud slab surrounded by clear-air regions and the TKE dissipation rate ε was kept constant by an external homogeneous and isotropic forcing term. To further study cloud-clear air turbulence, Götzfried et al., 2017 adopted a different configuration: two cubes are attached together in order to model two adjacent regions, the cloud and the clear air, with a planar interface in between. Since no mean flow is included, the mixing that develops is of the shearless type. Gravity is parallel to the interfacial plane and the mixing region widens in the horizontal direction. The same domain was chosen by Tordella and Iovieno, 2011, 19 and M. Iovieno, Di Savino, Gallana, and Tordella, 2014 in their studies of turbulent shearless mixing. Recently, Gao et al., 2018 solved a 0.512^3 m^3 turbulent field with 256^3 grid points to study the influence of different microphysical parameters on the nature of the mixing regime. A similar approach is shown in the work by Li et al., 2020, in which both condensational and collisional growth are taken into account.

In this study, results from a set of eighteen direct numerical simulations of a cloud-clear air interface are presented. The numerical model is similar to the one adopted by Li et al., 2020, while the computational domain consists of two cubes that represent the cloud and the clear-air region, respectively. The domain is identical to the one in Götzfried et al., 2017, but vertically oriented. That is, gravity is normal to the interface. The cloud slab (cube) is located at the bottom to mimic a shearless mixing process at the cloud top. The code, which includes condensational and collisional growth and neglects droplet break up, is a new version of `TurIsMis`, which has been recently used by Bhowmick and Iovieno, 2019. The new version of such code features the Howell model for the condensational growth of small droplets (equation 2.11) and a non-periodic distribution of the

temperature field. Three simulations (`B012`, `B017` and `B018`) also introduced a fluctuating vapor field to study the effect of supersaturation fluctuations on the evolution of the droplet spectrum.

5.1 Mathematical model

5.1.1 Boussinesq Navier-Stokes equations

The Navier-Stokes equations for mass, momentum and energy describe the macroscopic motion of a fluid for low Knudsen numbers (i.e. $Kn \ll 1$). The Navier-Stokes equations consist in a set of partial differential equations for mass, momentum and energy conservation whose 2D and 3D solutions often include turbulence. In this section the complete form of such equations is derived. A simplified form, often used for problems of stratification and thermal convection at low Mach numbers and known as the Boussinesq approximation, is introduced (see Tritton, 1988, pp. 188-196).

Mass and momentum conservation equations

Let's consider an arbitrary spatial volume Ω. The mass conservation law is

$$\frac{\partial}{\partial t}\oint_{\Omega}\rho\, d\Omega + \oint_{\partial\Omega}\rho\boldsymbol{V}\cdot\boldsymbol{n}d(\partial\Omega) = \oint_{\Omega}Q_m d\Omega$$

Q_m being the fluid mass injection rate into the volume Ω. It can be written in the differential form

$$\frac{\partial\rho}{\partial t} + \nabla\cdot(\rho\boldsymbol{V}) = Q_m \tag{5.1}$$

The same can be done to derive the momentum conservation equation for the fluid flow

$$\frac{\partial}{\partial t}\oint_{\Omega}\rho\boldsymbol{V}d\Omega + \oint_{\partial\Omega}\rho\boldsymbol{V}\boldsymbol{V}\cdot\boldsymbol{n}\, d(\partial\Omega) = \oint_{\partial\Omega}\boldsymbol{\Pi}\, d(\partial\Omega) + \oint_{\Omega}\left(\rho\boldsymbol{f} + Q_m\boldsymbol{V}\right)d\Omega$$

Here $\boldsymbol{\Pi} = -p\boldsymbol{I} + \boldsymbol{\tau}$ is the stress tensor, p is the pressure (which coincides with the thermodynamic pressure under Stokes' hypothesis) and $\boldsymbol{\tau}$ the viscous shear stress tensor. Because of equation 5.1, the momentum conservation can be written in the more compact differential form

$$\rho\frac{D\boldsymbol{V}}{Dt} = \nabla\cdot\boldsymbol{\Pi} + \rho\boldsymbol{f} \tag{5.2}$$

Total energy

The total energy E per unit mass is the sum of the internal energy ⌉ per unit mass and the kinetic energy $1/2V^2$ per unit mass. Its conservation equation

$$\frac{\partial}{\partial t}\oint_{\Omega}\rho E\,d\Omega+\oint_{\partial\Omega}\rho E\boldsymbol{V}\cdot\boldsymbol{n}\,d(\partial\Omega)=\oint_{\partial\Omega}\boldsymbol{\Pi}\cdot\boldsymbol{V}\,d(\partial\Omega)+\oint_{\Omega}(\rho\boldsymbol{f}\cdot\boldsymbol{V}+Q_mE)\,d\Omega+ \\ -\oint_{\partial\Omega}\boldsymbol{q}\cdot\boldsymbol{n}\,d\boldsymbol{\Omega}+\oint_{\Omega}Q_w d\Omega$$

can be written in the differential form

$$\rho\frac{DE}{Dt}=\underbrace{-\boldsymbol{V}\cdot\nabla p+\boldsymbol{V}\cdot(\nabla\cdot\boldsymbol{\tau})+\rho\boldsymbol{f}\cdot\boldsymbol{V}}_{\text{kinetic terms}}\underbrace{-p\nabla\cdot\boldsymbol{V}+(\boldsymbol{\tau}\cdot\nabla)\cdot\boldsymbol{V}-\nabla\cdot\boldsymbol{q}+Q_w}_{\text{thermodynamic terms}} \tag{5.3}$$

The total energy equation can be split in two contributions. The first one, the kinetic energy equation, is derived by multiplying the momentum equation 5.2 by the velocity $\boldsymbol{V}$

$$\rho\frac{D}{Dt}\frac{\boldsymbol{V}\boldsymbol{V}}{2}=-\boldsymbol{V}\cdot\nabla p+\boldsymbol{V}\cdot(\nabla\cdot\boldsymbol{\tau})+\rho\boldsymbol{f}\cdot\boldsymbol{V} \tag{5.4}$$

The second one accounts for the thermodynamic processes occurring in the fluid flow and can be expressed as a function of the internal energy per mass unit e[1]

$$\rho\frac{De}{Dt}=-p\nabla\cdot\boldsymbol{V}+(\boldsymbol{\tau}\cdot\nabla)\cdot\boldsymbol{V}-\nabla\cdot\boldsymbol{q}+Q_w \tag{5.5}$$

or of the static enthalpy $h=e+p/\rho$

$$\rho\frac{Dh}{Dt}=\underbrace{\frac{\partial p}{\partial t}+\boldsymbol{V}\cdot\nabla p}_{Dp/Dt}+(\boldsymbol{\tau}\cdot\nabla)\cdot\boldsymbol{V}-\nabla\cdot\boldsymbol{q}+Q_w \tag{5.6}$$

Equations 5.4 and 5.6 are coupled by the term $\boldsymbol{V}\cdot\nabla p$. Equations 5.5 and 5.6 are both functions of the static temperature T (recall that $h=c_pT$, $e=c_vT$ and $c_p-c_v=R/\mathcal{M}$)

$$\rho c_v\frac{DT}{Dt}=-p\nabla\cdot\boldsymbol{V}+(\boldsymbol{\tau}\cdot\nabla)\cdot\boldsymbol{V}-\nabla\cdot\boldsymbol{q}+Q_w$$
$$\rho c_p\frac{DT}{Dt}=\frac{Dp}{Dt}+(\boldsymbol{\tau}\cdot\nabla)\cdot\boldsymbol{V}-\nabla\cdot\boldsymbol{q}+Q_w$$

[1]Not to be confused with the vapor pressure e.

Additional equations

Additional equations are required to close the Navier-Stokes system. The perfect gas law 2.1

$$\frac{p}{\rho} = \frac{R}{\mathcal{M}} T$$

the Fourier law (heat transfer)

$$\boldsymbol{q} = -K \nabla T \tag{5.7}$$

with K denoting the thermal conductivity and the stress tensor

$$\boldsymbol{\tau} = \mu \left(\nabla \boldsymbol{V} + [\nabla \boldsymbol{V}]^T \right) - \frac{2}{3} \mu \left(\nabla \cdot \boldsymbol{V} \right) \boldsymbol{I} \tag{5.8}$$

The code solves the Navier-Stokes equations for mass, momentum and energy for incompressible flows under the Boussinesq approximation. The Boussinesq approximation assumes that variations of both the fluid density and viscosity are ignored. Small perturbations of the density field, though, are taken into account in the buoyancy terms.[2]

The mass conservation law reduces to the known incompressible form:

$$\nabla \cdot \boldsymbol{u} = 0 \tag{5.9}$$

Conservation of momentum becomes:

$$\frac{D\boldsymbol{V}}{Dt} = -\frac{1}{\rho_0} \nabla P + \nu \nabla^2 \boldsymbol{V} + B\boldsymbol{g} \tag{5.10}$$

with ρ_0 being the nominal density, sometimes referred to as Boussinesq density (e.g. Andrejczuk et al., 2004). B accounts for density variations with respect to ρ_0 and can be splitted into two main contributions

$$B = B_\theta + B_\rho. \tag{5.11}$$

that is the generation or depletion of water vapor B_ρ and/or increasing or decreasing potential temperature B_θ. P is the overall flow pressure and accounts for both the dynamic pressure p and Stevin's term $\rho_0 \boldsymbol{g} \boldsymbol{z}$, with $\boldsymbol{z}$ being the elevation in the local domain (Tritton, 1988).

$$P = p + \rho_0 \boldsymbol{g} \boldsymbol{z}$$

[2]See also Holton, 2004 p. 117 and p. 197. On the applicability of the Boussinesq approximation see Tritton, 1988 pg. 16 and Holton, 2004, p. 117.

The energy equation reduces to the simpler Boussinesq form:[3]

$$\frac{\partial T}{\partial t} + \boldsymbol{V} \cdot \nabla T = \kappa \nabla^2 T + \frac{J}{\rho_0 c_p} \tag{5.12}$$

with J denoting the source term per unit mass [$\mathrm{J\,kg^{-1}}$].

Non-dimensional form of the equations

The terms in 5.1 5.10 5.12

$$\widetilde{x} = \frac{x}{L_{ref}} \quad \widetilde{\boldsymbol{V}} = \frac{\boldsymbol{V}}{U_{ref}} \quad \widetilde{\boldsymbol{g}} = \boldsymbol{g}\frac{L_{ref}}{U_{ref}^2} \quad \Theta = \frac{T - T_{ref}}{T_{ref}}$$

Equations (5.9) (5.10) and (5.12) become:

$$\begin{cases} \tilde{\nabla} \cdot \tilde{\boldsymbol{V}} = 0 \\ \dfrac{D\widetilde{\boldsymbol{V}}}{D\tilde{t}} = -\widetilde{\nabla}\tilde{P} + \dfrac{1}{Re_{ref}}\widetilde{\nabla}^2\widetilde{\boldsymbol{V}} + B\tilde{\boldsymbol{g}} \\ \dfrac{D\Theta}{D\widetilde{t}} = \dfrac{1}{Pr}\dfrac{1}{Re_{ref}}\widetilde{\nabla}^2\Theta + \widetilde{\left(\dfrac{J}{\rho_0 c_p}\right)} \end{cases} \tag{5.13}$$

Buoyancy terms

The momentum equation 5.10 in the positive vertical-z direction takes the form

$$\frac{Dw}{Dt} = -\frac{1}{\rho_0}\nabla p - \frac{\Delta\rho}{\rho_0}\,|g| + \nu\nabla^2 w$$

The total density of the mixture ρ, averaged over the volume of the computational domain, is the sum of the contributions of both air and saturated vapour

$$\rho = \rho_a + \rho_v \tag{5.14}$$

---

[3] By considering the internal energy equation for inviscid flows (with viscous effects being neglected in the thermal balance) one can write:

$$\rho_0 \frac{Dh}{Dt} = \frac{Dp}{Dt} + Q$$

h being the enthalpy per unit mass and Q a volume source of internal energy. One gets

$$\rho c_p \frac{DT}{Dt} = \frac{Dp}{Dt} + Q \approx Q = J + k\nabla^2 T$$

The material derivative for the pressure can be neglected (see Tritton, 1988, chapter 14, appendix).

By writing everything in the differential form one gets

$$\rho = \rho_0 + \frac{\partial \rho}{\partial T}\Delta T + \frac{\partial \rho}{\partial \rho_v}\Delta \rho_v + \frac{\partial \rho}{\partial \rho_a}\Delta \rho_a$$

By considering only small perturbations of both temperature and density one has $\partial\rho/\partial T \sim -\rho_0\alpha \sim 1/T_0$ and

$$\rho = \rho_0 - \rho_0 \frac{\Delta T}{T_0} + \Delta \rho_a + \Delta \rho_v \tag{5.15}$$

so that

$$B = B_\theta + B_v = -\left|\boldsymbol{g}\right| \left(1 - \frac{\Delta T}{T_0} + \frac{\Delta \rho_a}{\rho_0} + \frac{\Delta \rho_v}{\rho_0}\right) \tag{5.16}$$

Buoyancy due to temperature

The impact that small perturbations of temperature in equation 5.15 can be linearly described a simple linear model

$$\rho = \rho_0 \left[1 - \frac{1}{\theta_0}\left(\theta - \theta_0\right)\right]$$

with $\alpha \sim 1/\theta_0$ being the expansion coefficient (Rogers & Yau, 1996). The DNS code simulates an overall isobaric process and, from now on, the equations will consider the static temperature instead of the potential temperature (see equation 2.5). If one introduces the non-dimensional temperature

$$\Theta = \frac{T - T_{ref}}{T_{ref}}$$

with T_{ref} being an arbitrary reference temperature which corresponds to saturated vapor reference values (see equation 2.3), one can express the temperature contribution in a non-dimensional form

$$B_\theta = \left.\frac{\rho - \rho_0}{\rho_0}\right|_{M_v = const} = -\frac{\Theta}{\Theta_0 + 1} \underbrace{-\frac{1}{\Theta_0 + 1} + 1}_{\text{constant}} \tag{5.17}$$

The constant term in the above equation describes a global displacement of the whole domain and is included in the a_0 coefficient of the Fourier series as it is transformed in the spectral domain

$$\widehat{B_\theta}(\boldsymbol{\kappa}) = -\frac{\widehat{\Theta}(\boldsymbol{\kappa})}{\Theta_0 + 1}$$

Buoyancy due to production or depletion of water vapor

The density of the single i-th species ρ_i^* and the density of the species taken over the computational volume ρ_i are defined as follows

$$\rho_i^* = \frac{M_i}{V_i} \quad \rho_i = \frac{M_i}{V_{tot}}$$

If one considers the single species on its own occupied volume, the perfect gas relation accounts for the global pressure p and the constant temperature T_0:

$$p = \rho_i^* \frac{R}{\mathcal{M}_i} T_0$$

conversely, if one considers the single species on its computational volume, only the partial pressure will be taken into account

$$p_i = \rho_i \frac{R}{\mathcal{M}_i} T_0$$

of course, $V_i = M_i/\rho_i^*$. Rearranging the two perfect-gas relations, we will get

$$V_i = \frac{RT_0}{p} \frac{M_i}{\mathcal{M}_i}$$

The Boussinesq approximation is based on the incompressibility of the carrier flow. This implies that the total volume occupied by the gas shall coincide with the computational volume at any time, i.e.

$$V_{tot} = \frac{RT_0}{p} \sum_i \frac{M_i}{\mathcal{M}_i} = const$$

That is, the following condition must be satisfied

$$\frac{1}{V_{tot}} \frac{RT}{p} \sum_i \frac{M_i}{\mathcal{M}_i} = 1$$

and, of course,

$$\frac{\Delta\rho_a}{\mathcal{M}_a} + \frac{\Delta\rho_v}{\mathcal{M}_v} = 0$$

The latter condition results in the expression for mixture-related density variations (at a constant temperature).

$$\rho - \rho_0|_{T=const} = \Delta\rho_a + \Delta\rho_v = \left(1 - \frac{\mathcal{M}_a}{\mathcal{M}_v}\right) \Delta\rho_v$$

where $\Delta\rho_v = \rho_v(T) - \rho_v(T_0)$. This can be rewritten as

$$\rho - \rho_0|_{T=const} = \rho_v\left(T_0\right)\left(1 - \frac{\mathcal{M}_a}{\mathcal{M}_v}\right)\left(\frac{\rho_v\left(T\right)}{\rho_v\left(T_0\right)} - 1\right) \tag{5.18}$$

One can non-dimensionalize equation 5.18 with respect to the saturated vapor reference density $\rho_{vs}(T_{ref})$ that was given in chapter 2

$$\left.\frac{(\rho - \rho_0)}{\rho_0}\right|_{T=const} = \frac{\rho_v(T_0)}{\rho_{vs}(T_{ref})}\frac{\rho_{vs}(T_{ref})}{\rho_0}\left(1 - \frac{\mathcal{M}_a}{\mathcal{M}_v}\right)\left(\frac{\rho_v\left(T\right)}{\rho_{vs}\left(T_{ref}\right)}\frac{\rho_{vs}\left(T_{ref}\right)}{\rho_v\left(T_0\right)} - 1\right)$$

rearranging one gets

$$\left.\frac{\rho - \rho_0}{\rho_0}\right|_{T=const} = \widetilde{\rho}_v(T_0)\frac{\rho_{vs}(T_{ref})}{\rho_0}\left(1 - \frac{\mathcal{M}_a}{\mathcal{M}_v}\right)\left(\frac{\widetilde{\rho}_v(T)}{\widetilde{\rho}_v(T_0)} - 1\right) \tag{5.19}$$

Constant terms of equation 5.19 are included in the a_0 coefficient of the Fourier series when as they are transformed in the spectral domain. This allows the buoyancy term $\widehat{B_v}$ to be computed as follows

$$\begin{aligned}\widehat{B_v}(\boldsymbol{\kappa}) &= -|g|\left.\frac{\widehat{\rho - \rho_0}}{\rho_0}\right|_{T=const} \\ &= -|g|\frac{\rho_{vs}(T_{ref})}{\rho_0}\left(1 - \frac{\mathcal{M}_a}{\mathcal{M}_v}\right)\hat{\rho}_v(\boldsymbol{\kappa}, T)\end{aligned} \tag{5.20}$$

5.1.2 Droplet dynamics and vapor field

Saturated vapor

The saturated vapor density inside the cloud is related to the local temperature through the Clausius-Clapeyron law 2.4

$$\rho_{sv}\left(T\right) = \frac{p_{sv}\left(T_{ref}\right)}{R_v T}\, exp\left[\frac{L}{R_v^*}\left(\frac{1}{T_{ref}} - \frac{1}{T}\right)\right] \tag{5.21}$$

with $R = 8314\ \mathrm{J\,kg^{-1}\,kmol}$ universal constant, $L_w = 2272\ \mathrm{kJ\,kg^{-1}}$ the water evaporation latent heat, $\mathcal{M}_v = 18\ \mathrm{kg\,kmol^{-1}}$ the vapour molar mass. Again, reference values are set for $T_{ref} = 273.15$ K and its vapour pressure $p_{sv}\left(T_{ref}\right) = 611.3$ Pa.

By introducing the non-dimensional temperature

$$\Theta = \frac{T - T_{ref}}{T_{ref}}$$

one can get to the non-dimensional form of the 2.4:

$$\tilde{\rho}_{sv}\left(\Theta\right) = \frac{\rho_{sv}\left(\Theta\right)}{\rho_{sv}\left(T_{ref}\right)} = \frac{1}{1+\Theta}\, exp\left[\frac{L}{R_v T_{ref}}\frac{\Theta}{1+\Theta}\right] \tag{5.22}$$

Droplet momentum equation

Water drops are assumed to be spherical and to be subject to the interaction of the Stokes drag and buoyancy forces only (Raymond A. Shaw, 2003). Following chapter 3, one can assume that the forces acting on a spherical droplet moving through the air in the low-Reynolds Stokes regime are the Stokes drag $\boldsymbol{D}$ and the buoyancy forces $\boldsymbol{B}$:

$$m_d \frac{D\boldsymbol{v}}{Dt} = \boldsymbol{D} + \boldsymbol{B}$$

m_d being the droplet mass and $\boldsymbol{v}$ the droplet velocity. These assumptions lead to the well known equation for the motion of a spherical droplet 3.8

$$\frac{D\boldsymbol{v}}{Dt} = \frac{1}{\tau_d}(\boldsymbol{V} - \boldsymbol{v}) + \left(1 - \frac{\rho_a}{\rho_w}\right)\boldsymbol{g}$$

Such equation can be non-dimensionalized by taking, as usual,

$$\widetilde{v} = \frac{v}{U_{ref}} \quad \widetilde{t} = \frac{tU_{ref}}{L_{ref}} \quad \widetilde{r} = \frac{r}{R_{ref}} \quad \widetilde{g} = \frac{gL_{ref}}{U_{ref}^2}$$

getting

$$\frac{D\widetilde{\boldsymbol{v}}}{D\widetilde{t}} = \frac{9}{2}\frac{\rho_a}{\rho_w}\frac{\nu}{U_{ref}L_{ref}}\frac{L_{ref}^2}{R_{ref}^2}\frac{\widetilde{\boldsymbol{V}} - \widetilde{\boldsymbol{v}_d}}{\widetilde{\boldsymbol{r}}^2} + \left(\frac{\rho_a}{\rho_w} - 1\right)\widetilde{\boldsymbol{g}}$$

This formulation introduces the non-dimensional reference radius R_{ref}/L_{ref} and the reference Reynolds number Re_{ref}:

$$\frac{D\widetilde{\boldsymbol{v}}}{D\widetilde{t}} = \frac{9}{2}\frac{\rho_a}{\rho_w}\frac{1}{Re_{ref}}\frac{1}{\widetilde{R}_{ref}^2}\frac{\widetilde{\boldsymbol{V}} - \widetilde{\boldsymbol{v}}}{\widetilde{r}^2} + \left(\frac{\rho_a}{\rho_w} - 1\right)\widetilde{g} \tag{5.23}$$

The water vapor balance equation

The mass conservation law for the vapour in the cloud parcel can be written as follows

$$\frac{D\rho_v}{Dt} + \rho_v \nabla \cdot \boldsymbol{V} = \kappa_v \nabla^2 \rho_v - C_v$$

with C_v being the condensation term. As the vapor condenses (positive C_v) the local amount of vapor decreases. Since we're dealing with incompressible flows, the mass balance equation acquires the form

$$\frac{D\rho_v}{Dt} = \kappa_v \nabla^2 \rho_v - C_v \tag{5.24}$$

with ρ_v being the vapor density. The condensation term can be expressed as the droplet mass rate averaged on a sphere with center in $\boldsymbol{x}$ and radius δ. In this volume, the total liquid water mass accounts for the contribution of the k-th droplet

$$C_v = \frac{1}{\Omega_{\boldsymbol{x},\delta}} \sum_{x_k \in \Omega_{\boldsymbol{x},\delta}} \frac{dm_k}{dt} = \frac{1}{\Omega_{\boldsymbol{x},\delta}} \sum_{x_k \in \Omega_{\boldsymbol{x},\delta}} \frac{d}{dt}\left(\rho_w \frac{4}{3}\pi r_k^3\right) = \frac{4\pi}{3}\frac{\rho_w}{\Omega_{\boldsymbol{x},\delta}} \sum_{x_k \in \Omega_{\boldsymbol{x},\delta}} 3r_k^2 \frac{dr_k}{dt}$$

in the DNS code the arbitrary volume $\Omega_{\boldsymbol{x},\delta}$ will coincide with the mesh grid cell, a cube with volume Δx^3. Therefore, the condensation rate can be expressed as follows

$$C_v = \frac{4\pi}{3}\frac{\rho_w}{\Delta x^3} \sum_{x_k \in \Delta x^3} 3r_k^2 \frac{dr_k}{dt} \tag{5.25}$$

Equations 5.24 and 5.25 can be written in the non-dimensional forms

$$\frac{\rho_{sv}(T_{ref})U_{ref}}{L_{ref}} \frac{D\widetilde{\rho}_v}{D\widetilde{t}} = \kappa_v \widetilde{\nabla}^2 \widetilde{\rho}_v \frac{\rho_{sv}(T_{ref})}{L_{ref}^2} - \widetilde{C}_v \frac{\rho_{sv}(T_{ref})U_{ref}}{L_{ref}}$$

$$\frac{\rho_{sv}(T_{ref})U_{ref}}{L_{ref}} \widetilde{C}_v = \frac{4}{3}\pi \frac{\rho_w}{\Delta x^3} \frac{1}{\rho_{sv}(T_{ref})} \frac{L_{ref}^3}{L_{ref}^3} \sum_{\Delta x^3} \widetilde{R}_{ref}^3 3\widetilde{r}_k^2 \frac{d\widetilde{r}_k}{d\widetilde{t}} \frac{\rho_{sv}(T_{ref})U_{ref}}{L_{ref}}$$

that is

$$\frac{D\widetilde{\rho}_v}{D\widetilde{t}} = \frac{1}{Sc_v} \frac{1}{Re_{ref}} \widetilde{\nabla}^2 \widetilde{\rho}_v - \widetilde{C}_v \tag{5.26}$$

$$\widetilde{C}_v = 4\pi \frac{\rho_w}{\rho_{sv}(T_{ref})} \frac{\widetilde{R}_{ref}^3}{\widetilde{\Delta x}^3} \sum_{\Delta x^3} \widetilde{r}_k^2 \frac{d\widetilde{r}_k}{d\widetilde{t}} \tag{5.27}$$

with Sc_v being the water vapor Schmidt number, usually $\cong 0.61$. The implementation of the condensational droplet growth rate dr_k/dt is shown in the next section.

No aerosol model is included in code and once a droplet is eliminated it will not appear again. Secondary activation may be implemented in future versions of the code.

Droplet killing reasons include complete evaporation (the droplet radius reduces below the critical value $r_c = 0.04$ µm), gravitational settling below the lower boundary (droplet position for $x_2 \leq 0$) or droplet collision. The code assumes full collision efficiency and as the droplet collide, one of them is deleted.

Droplet growth by condensation

Droplet radii are updated at each time step by computing the istantaneous growth rate given by the Howell's model (equation 2.11), which can be non-dimensionalized

with respect to the reference length L_{ref}, flow velocity U_{ref} and droplet radius R_{ref}. Again, also the non-dimensional radius $\widetilde{R}_{ref} = R_{ref}/L_{ref}$ can be used. One gets

$$\frac{R_{ref}^2 U_{ref}}{L_{ref}} \widetilde{r} \frac{d\widetilde{r}}{d\widetilde{t}} = C_r \left(s - \frac{A}{r} + k \frac{r_{dry}^3}{r^3} \right)$$

$$\widetilde{r} \frac{d\widetilde{r}}{d\widetilde{t}} = \frac{C_r L_{ref}}{R_{ref}^2 U_{ref}} \left(s - \frac{A}{r} + k \frac{r_{dry}^3}{r^3} \right)$$

and eventually

$$\frac{d\widetilde{r}}{d\widetilde{t}} = \frac{\widetilde{C_r}}{\widetilde{r}} \left(s - \frac{A}{r} + k \frac{r_{dry}^3}{r^3} \right) \tag{5.28}$$

with

$$\widetilde{C_r} = \frac{C_r}{U_{ref} L_{ref} \widetilde{R}_{ref}}$$

The Kelvin coefficient A is computed from equation 2.12. The surface tension is computed via 2.13 as a function of the mean initial temperature T_{mean0}. For $T_{mean0} = 281$ K one gets $\sigma_{s/a} = 74.5 \cdot 10^{-3}$ J/m^2 and $A = 2.45 \cdot 10^{-4}$ m. Values of the hygroscopicity parameter $k = 0.7$ and $r_{dry} = 0.01$ µm are set for all the simulations (for typical ranges of the hygroscopicity parameter see Petters and Kreidenweis, 2007).

Droplet growth by collision-coalescence

The DNS code includes a droplet collision detection algorithm that scans a small portion of the domain in search of possible impacts between droplets at each time step. It only scans a small portion in order to reduce the number of operations $\sim n^2$ which would be requested to compute mutual distances between every pair of drops. The code assumes full collision efficiency. If two droplets have come across at a distance lower than the sum of the two radii then droplet coalescence is supposed to have taken place. The droplet with the lower ID is subsequently killed and the two original volumes sum in the remaining droplet, which will have grown[4].

[4]More details on the algorithm can be found at the official page of the Philofluid Research Group (https://areeweb.polito.it/ricerca/philofluid/software/252-collision).

5.1.3 Conservation of the internal energy

Under the assumptions of the Boussinesq approximation the evolution of the temperature field is governed by the relation 5.12

$$\frac{\partial T}{\partial t} + \boldsymbol{V} \cdot \nabla T = \kappa \nabla^2 T + \frac{J}{\rho_0 c_p}$$

In this case, the source term J expresses the release (absorption) of latent heat by the ambient phase as condensation (evaporation) occurs. The latent heat L_w is ceased during transition between the phases, its amount being proportional to the amount of mass involved. For liquid water and vapor, a good estimate can be $L_w \cong 2.5 \cdot 10^6$ J kg^{-1} (Kumar et al., 2013). One gets

$$J = L_w C_v$$

and

$$\frac{DT}{Dt} = \kappa \nabla^2 T + \frac{L_w C_v}{\rho_0 c_p} \tag{5.29}$$

with C_v from 5.25. By introducing the non-dimensional temperature $\Theta = T/T_{ref} - 1$ and recalling from 5.27

$$C_v = \widetilde{C}_v \frac{\rho_{sv}(T_{ref}) U_{ref}}{L_{ref}}$$

one can write

$$\frac{U_{ref} T_{ref}}{L_{ref}} \frac{D\Theta}{Dt} = \kappa \widetilde{\nabla}^2 \Theta \frac{T_{ref}}{L_{ref}^2} + \frac{L_w}{\rho_0 c_p} \widetilde{C}_v \frac{T_{ref}}{T_{ref}} \frac{\rho_{sv}(T_{ref}) U_{ref}}{L_{ref}}$$

which results in

$$\frac{D\Theta}{Dt} = \frac{1}{Pr} \frac{1}{Re_{ref}} \widetilde{\nabla}^2 \Theta + \frac{L_w \rho_{sv}(T_{ref})}{\rho_0 c_p T_{ref}} \widetilde{C}_v \tag{5.30}$$

Supersaturation evolution

The relative humidity and the supersaturation are defined as (see 2)

$$RH = \frac{e}{e_s} = \frac{\rho_v}{\rho_{sv}(T)}$$

$$s = RH - 1 = \frac{e}{e_s} - 1 = \frac{\rho_v}{\rho_{vs}(T)} - 1$$

and the supersaturation evolution can be estimated by solving equations 5.26 and 5.30 in combination with the non-dimensional Clausius-Clapeyron equation 2.4

$$q_{sv}(\Theta) = \frac{\rho_{vs}(\Theta)}{\rho_{sv}(T_{ref})} = \frac{1}{1+\Theta} exp\left[\frac{L_w}{R_v T_{ref}} \frac{\Theta}{1+\Theta}\right] \tag{5.31}$$

The ratio ρ_v/ρ_{sv} can be expressed in the non-dimensional form

$$\frac{\rho_v}{\rho_{sv}} = \frac{\rho_v(T)}{\rho_{sv}(T_{ref})}\frac{\rho_{sv}(T_{ref})}{\rho_{sv}(T)} = \frac{q_v(\Theta)}{q_{sv}(\Theta)}$$

5.2 Computational domain

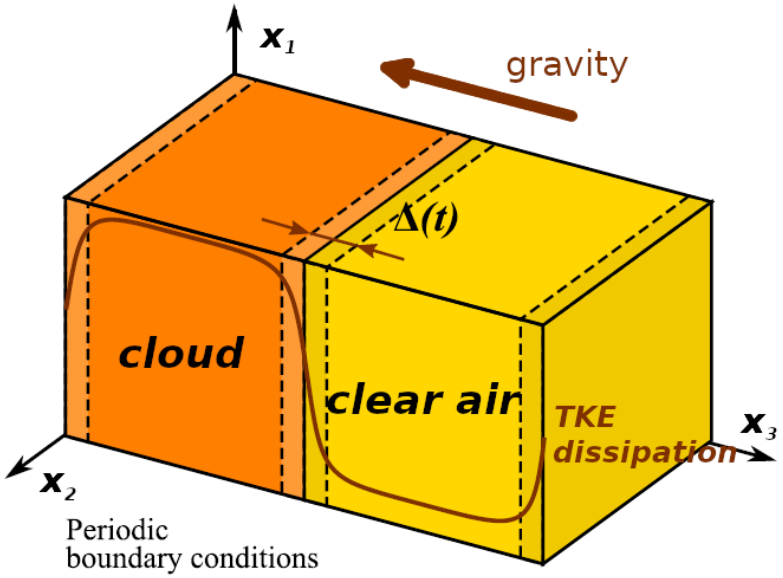

Figure 5.1: Scheme of the computational domain (adapted from Tordella and Iovieno, 2011, 19). The thick brown line shows the qualitative trend of both TKE and TKE dissipation rate across the interface. The mixing width Δ is expected to increase with time. The integral scale is the same in both regions.

The computational domain (figure 5.1) consists in a parallelepiped made up by two adjacent cubes. The mesh is uniform and each cell is a 1 mm-edge cube ($\Delta x = 1$ mm). Each cube edge is divided into $n = 512$ cells. The parallelepided is thus made up with $512^2 \times 1024$ cells. Each cube edge has a dimensional length of $H = n\Delta x = 0.512$ m.

The reference length is chosen to be equal to $L_{ref} = \dfrac{H}{2\pi} = 0.0815$ m. The non-dimensional domain cube edge length is then $\dfrac{H}{L_{ref}} = 2\pi$ and the computational domain is $(2\pi)^2 \times 4\pi$ wide.

The domain in the physical space is represented by a vector field $\begin{bmatrix} x_1 & x_3 & x_2 \end{bmatrix}^T$, $x3$ being the non-homogeneous direction parallel to the largest (4π) parallelepiped

length. The non-homogeneous direction is normal to the two cubes interface, which models the cloud-clear air region interface.

The DNS code uses a slab parallelization, which is realized by dividing the parallelepiped into n_{procs} slices of width $n_{loc} = n/n_{procs}$ and length $2n$, that are floored as tiles one over the other in the x_2 homogeneous direction in the physical space. In order to compute the 3D FFT of such domain, a parallel transposition must be executed between the cores. The Fourier space domain is represented through a vector field $\begin{bmatrix} \kappa_1 & \kappa_2 & \kappa_3 \end{bmatrix}^T$, κ_3 being again the non-homogeneous direction parallel to the largest (4π) parallelepiped length. In the Fourier space, the longest direction is distributed among the cores (M. Iovieno, Cavazzoni, & Tordella, 2001; Tordella & Iovieno, 2006; Tordella, Iovieno, & Bailey, 2008).

5.2.1 Initial conditions

Synthetic turbulent field

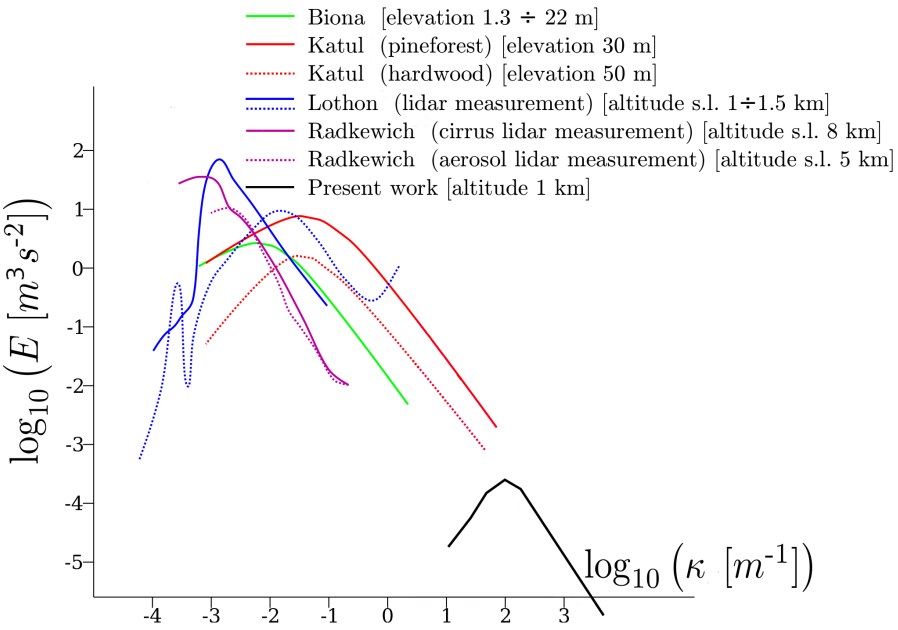

Figure 5.2: In this figure the turbulent spectrum used to generate the synthetic velocity field is plotted (black solid line) and compared to other spectra obtained via in-situ measurements (Biona, Druilhet, Benech, & Lyra, 2001; Katul, Geron, Hsieh, Vidakovic, & Guenther, 1998; Lothon, Lenschow, & Mayor, 2009; Radkevich, Lovejoy, Strawbridge, Schertzer, & Lilley, 2009). Image adapted from Gallana, 2016.

Two synthetic homogeneous and isotropic turbulent cubes are generated and attached together to build the initial flow field. Each turbulent cube is initialized as a zero-mean fluctuating field with an arbitrary amount of TKE. In order to generate such fields, a potential field $\boldsymbol{W}$ is obtained by allocating the kinetic energy content over all the scales of motion following a model spectrum (see also Pope, 2000, pp. 232-234) defined by

$$\begin{cases} E(\kappa) \sim \kappa^{\alpha} & \kappa < \kappa_{peak} \\ E(\kappa) \sim \kappa^{-5/3} & \kappa \geq \kappa_{peak} \end{cases}$$

with the exponent α and the peak wavenumber κ_{peak} being set as simulation parameters. The incompressible (soleinoidal) velocity field is then obtained by taking the rotor of the potential field

$$\boldsymbol{V} = \nabla \wedge \boldsymbol{W}$$

by recalling that $\nabla \cdot (\nabla \wedge (\cdot)) = 0$. The total energy allocated for each wavenumber is subsequently renormalized to get the correct amount of total energy. The process can be repeated for all the velocity components. By setting the average root mean square velocity u_{rms} one gets the total kinetic energy

$$\mathcal{K} = \frac{3}{2} u_{rms}^2$$

Finally, the turbulent parallelepiped is obtained by matching the two cubes together. The intensity of the final turbulent field is modulated spatially in the non-homogeneous direction (x_3) as done by Götzfried et al., 2017; M. Iovieno et al., 2014; Tordella and Iovieno, 2011, 19; Tordella et al., 2008

$$\widetilde{\mathcal{K}} = \widetilde{\mathcal{K}}_1 - \widetilde{\mathcal{K}}_2 \, p(\widetilde{x_3})$$

with

$$p(\widetilde{x_3}) = tanh\left(55\frac{\widetilde{x_3}}{4\pi}\right) tanh\left(55\left(\frac{\widetilde{x_3}}{4\pi} - \frac{1}{2}\right)\right) tanh\left(55\left(\frac{\widetilde{x_3}}{4\pi} - 1\right)\right)$$

a smooth distribution of this kind prevents the arising of the Gibbs phenomenon (M. Iovieno et al., 2014). The choice of both the model spectrum shape (k_{peak} and α) and the energy content determines the amplitude of the integral scale and the velocity fluctuations, respectively. Using the description of homogeneous and isotropic turbulence provided by Monin and Yaglom, 2013, we have that the integral scale of an homogeneous isotropic solenoidal velocity field can be expressed as a function of the energy spectrum $\widehat{\mathcal{K}}$

$$\ell = \frac{3\pi}{4} \frac{\int_0^\infty \kappa^{-1} E(\kappa)\, d\kappa}{\int_0^\infty E(\kappa)\, d\kappa} \tag{5.32}$$

The parameters can be tuned in order to get the desired average TKE dissipation rate $\varepsilon \sim u_{rms}^3/\ell$.

The parallelepiped-shaped domain that results is used to get the initial turbulent fields that will be read by the code at each run. To do so, each synthetic field - one for each velocity component - is integrated for a few time steps. The energy content is practically the same, but the flow field is now more realistic, having been generated by the Boussinesq Navier-Stokes equations.

Water vapor and temperature fields

The initial mean temperature of the domain is set to $T_0 = 281$ K, with a temperature difference between the cloud core and the clear air ΔT =-2 K.[5] The non-dimensional temperature is related to the dimensional temperature $T = T_{ref}\,(1 + \Theta)$, (the non-dimensional mean temperature being $\Theta_0 = (T_0 - T_{ref})\,/T_{ref}$). The non-dimensional temperature in each slab is

$$\Theta_{cloud} = \frac{1}{T_{ref}}\left(T_0 - \frac{\Delta T_0}{2} - T_{ref}\right) \quad \Theta_{air} = \frac{1}{T_{ref}}\left(T_0 + \frac{\Delta T_0}{2} - T_{ref}\right)$$

The vapor density in each slab is computed from the relative humidity RH, which is an arbitrary parameter, and the saturated vapor density, which depends on the local temperature (computed via the non dimensional Clausius-Clapeyron equation 2.4)

$$\tilde{\rho}_v = RH\tilde{\rho}_{vs} = \frac{RH}{1+\Theta}\,exp\left(\frac{L}{R_v T_{ref}}\frac{\Theta}{1+\Theta}\right)$$

The temperature gradient is fixed and equal to

$$\tilde{\nabla}\Theta = \frac{\Theta_{air} - \Theta_{cloud}}{n_3\Delta x}L_{ref}$$

The Brunt-Väisälä frequency 2.10

$$\mathcal{N} = \sqrt{\frac{g}{T_0}\frac{\Delta T_0}{n_3\Delta x}}$$

and the internal Froude number 2.9

$$Fr_{int}^2 = \frac{u_{rms}^2}{\ell^2\mathcal{N}^2}$$

[5]Steep spatial temperature gradients are common in cumulus clouds (see Andrejczuk et al., 2004 and references therein). In situ measurements (e.g. MacPherson and Isaac, 1977) detected lower temperatures near the cloud core, the region outside the cloud being warmer.

The non-dimensional initial temperature and water vapor density distributions are set as follows

$$\Theta(z) = \tilde{\nabla}\Theta \frac{2H}{L_{ref}} \left(tanh\left(55\left(\frac{\widetilde{x_3}}{4\pi} - \frac{1}{2}\right)\right) - \left(\frac{\widetilde{x_3}}{4\pi} - \frac{1}{2}\right)\right) + \Theta_0 \tag{5.33}$$

$$\begin{aligned}\widetilde{\rho}_v =& \frac{\widetilde{\rho}_{v,cloud} + \widetilde{\rho}_{v,air}}{2} + \\ &- \frac{\widetilde{\rho}_{v,air} - \widetilde{\rho}_{v,cloud}}{2} tanh\left(55\frac{\widetilde{x_3}}{4\pi}\right) tanh\left(55\left(\frac{\widetilde{x_3}}{4\pi} - \frac{1}{2}\right)\right) tanh\left(55\left(\frac{\widetilde{x_3}}{4\pi} - 1\right)\right)\end{aligned}$$

and are displayed in figure 5.3 and 5.4.

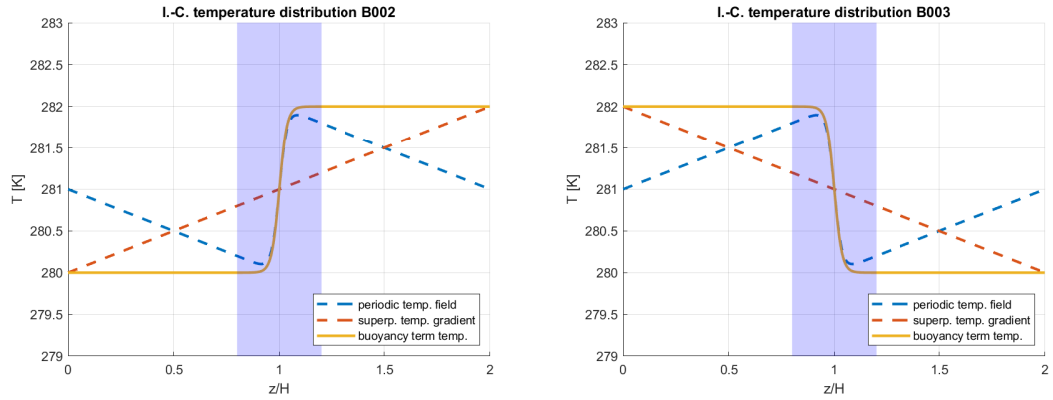

Figure 5.3: Initial conditions of temperature for stable (left) and unstable (right) stratification. The mixing is located approximately in the the highlighted area. The spectral code sees periodic boundary conditions for the temperature field. The buoyancy forcing term in the Navier-Stokes equations is subject to an additional temperature gradient (red dashed line). The physical, non-periodic temperature field is shown in yellow.

The temperature distributions in figure 5.3 need further discussion. The aim of the code is to simulate non-periodic temperature conditions (yellow curve) in order to consider a single stratified interface at the center. However, this configuration can't be used because of the onset of the Gibbs phenomenon. One possible solution consists in setting a periodic temperature field (blue dashed line) whose evolution can be computed through equation 5.30 with no dispersion-related issues. In order to compute the supersaturation and the buoyancy terms (equation 5.17) a constant virtual temperature gradient (orange dashed curve) is superposed to such periodic field. Basically, different code segments read different temperature fields in order to overcome this issue. The main drawback of this strategy is that, for long simulations, the periodic temperature field may be smoothed completely

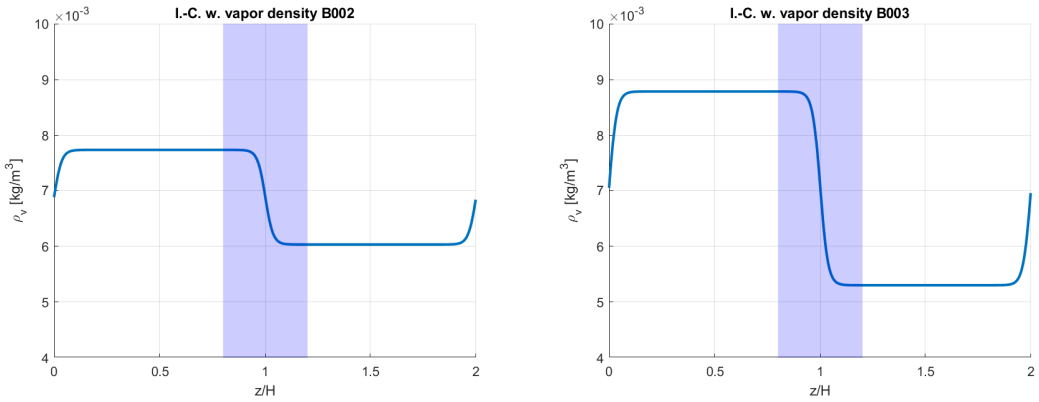

Figure 5.4: Initial conditions for the water vapor density in the computational domain. The relative humidity in the cloud and clear air slab is the same for both the stable (neutral) and unstable cases. The relative humidity in the cloud and clear air slab is chosen to be the same for the two cases.

(internal energy diffusion). If the simulation proceeds, the buoyancy terms and the supersaturation would be affected by the virtual gradient alone, leading to non-physical results. However this is not an issue in our cases, the total time of most simulations being equal or lower to 10 initial eddy turnover times.

In a few cases (see table 5.2) the initial vapor fields were set as turbulent scalar. The reason is that a fluctuating supersaturation field is more realistic and permits to study the impact of supersaturation variance in the broadening of the PDF in the cloud core region. The turbulent spectra that was used to generate such fields is similar to that described in the previous section for the velocity fields. Stationary supersaturation spectra were obtained from DNS by Lanotte et al., 2009 ($Re_\lambda \sim 200$) and showed a $-5/3$ power law in the inertial subrange.

Droplet distribution

These simulations use two type of initial conditions for the liquid phase. For both cases the particles are randomly distributed in the cloud slab, that is in the lower cube of the domain. Particle size distribution may be either monodisperse or polydisperse. In the monodisperse case, the LWC is uniformely distributed among all droplets, which will have the same radius. For instance, if one sets $LWC_0 = 0.8$ g/m^3, $H = 0.512$ m and $n_0 = 10^7$ and chooses a monodisperse distribution, the

algorithm will generate a set of randomly distributed drops with radius

$$r_{mono} = \left(\frac{LWC_0}{\frac{4}{3}\pi\rho_w \frac{n}{H^3}} \right)^{\frac{1}{3}} \cong 13.7\mu\text{m}$$

A polydisperse distribution can be generated by allocating the available LWC among a set of volume classes. The same fraction of LWC will be assigned to the same class and a larger amount of smaller droplets will be generated. To satisfy this condition, non-dimensional radius follows

$$\widetilde{r} = \frac{1}{R_{ref}} \frac{3}{4\pi} \left[\left(\Omega_{d,max} - \Omega_{d,min} \right) g(r) + \Omega_{d,min} \right]^{\frac{1}{3}}$$

with $g(\Omega)$ being a random function of the form

$$g(r) = \frac{exp\left(A_{poly} \cdot rand\,[0,1] \right) - 1}{exp\left(A_{poly} \right) - 1}$$

$rand\,[0,1]$ is a random number in the interval between 0 and 1 and A_{poly} an empiric constant given by

$$A_{poly} = 2.22 \left(log_{10} \frac{\Omega_{d,max}}{\Omega_{d,min}} - 2 \right) + 4.55$$

all particles are then normalized in order to get the desired total LWC.

5.3 Simulation parameters

Kinetic energy, integral scale and dissipation rate

The integral scale is chosen to be the same both in the cloud and in the clear air region, while the kinetic energy is higher in the former, resulting in different initial TKE dissipation rates for the two cubes. Periodic boundary conditions are adopted in all directions. The average TKE dissipation rate ε is chosen to be of the order of $\sim 200 \div 400$ cm^2/s^3 in the cloud cube (MacPherson & Isaac, 1977). Reference quantities are set by choosing a reference Reynolds number equal to 800. As stated below, the reference length is fixed as the ratio between the dimensional and non-dimensional box widths, that is $L_{ref} = H/(2\pi) \cong 0.082$ m. Hence, having

$$Re_{ref} = \frac{U_{ref} L_{ref}}{\nu} = 800$$

implies $U_{ref} = 0.14\ \mathrm{m\,s^{-1}}$. ν is the kinematic viscosity of the air $\cong 1.5 \cdot 10^{-5}\ \mathrm{m^2/s}$. The u_{rms} and the ratio between the kinetic energy levels in each cube are chosen for each simulation. By assuming the Kolmogorov similarity hypothesis for HIT, one can make an estimate of the Kolmogorov lengthscale for the more intense region by setting an average value of ε in such region. The initial u_{rms} velocity in the cloud region is set to $0.1\ \mathrm{m\,s^{-1}}$. By recalling equations 3.4 and assuming $\varepsilon \cong 400\ \mathrm{cm^2/s^3}$ one gets

$$\eta \sim \left(\frac{\nu^3}{\epsilon}\right)^{1/4} \cong 0.7\,\mathrm{mm} \sim \Delta x$$

A first estimate of the initial integral scale can be obtained estimated quantities for the more energetic region ℓ (equation 3.3)

$$\ell \sim \frac{u_{rms}^3}{\varepsilon} \cong 0.025\,\mathrm{m}$$

Again, the integral scale is the same across the interface. As in M. Iovieno et al., 2014, the kinetic energy ratio between the cloud and the clear air interface is set to $\mathcal{K}_{cloud}/\mathcal{K}_{air} \cong 6.7$. The initial eddy turnover time is estimated (following Bhowmick and Iovieno, 2019) as the ratio between the integral scale ℓ and the root mean square velocity u_{rms} of the more energetic slab (e.g. Kumar et al., 2018):

$$\tau_\ell \sim \frac{\ell}{u_{rms}} \cong 0.3\,\mathrm{s} \tag{5.34}$$

Computational scheme

The code integrates the system of equations () in the Fourier space using the pseudo-spectral algorithm first introduced in M. Iovieno et al., 2001. The lowest wavenumber κ_0 is defined with respect to the cube edge H (Pope, 2000 p. 345)

$$\kappa_0 = \frac{2\pi}{H} = \frac{1}{L_{ref}} \cong 12.27\,\mathrm{m^{-1}}$$

while the highest resolved wavenumber κ_{max}

$$\kappa_{max} = \frac{n}{2}\kappa_0 = \frac{\pi n}{H} = \frac{\pi}{\Delta x}$$

At least the low-order statistics of the flow at the small scales should not be sensitive to the value of κ_{max} associated to the mesh. This is verified (Ishihara, Gotoh, & Kaneda, 2009) if $\kappa_{max}\eta \gtrsim 2$. In order to satisfy this criterion, one can mesh each of the two cubes with an uniform grid made by 512^3 points. The mesh is the same for both the physical and the Fourier space. The grid resolution is $\Delta x = H/n = 10^{-3}$ m, that is

$$\kappa_{max}\eta \cong 2.2$$

which is acceptable.

The integration time step is set by considering the CFL condition (Pope, 2000, p. 348)

$$\Delta t = \frac{1}{20}\frac{\Delta x}{u_{rms,c}}$$

with respect to the most energetic region of the domain, that is the cloud. With $u_{rms,c} \cong 0.1\ \mathrm{m\,s^{-1}}$ one gets $\Delta t \cong 4.7 \cdot 10^{-4}$ s and $\widetilde{\Delta t} = \dfrac{U_{ref}}{L_{ref}}\Delta t \cong 9 \cdot 10^{-4}$.

The vertical temperature gradient $\widetilde{\nabla}\Theta$ across the interface also expresses a criterion for the local stratified stability. The initial mixing width can be estimated as done by Tordella and Iovieno, 2011, 19; Tordella et al., 2008 and turns out to be of the same order of the integral scale $\Delta \sim \ell$. By taking $\Delta \cong 0.02$ m (see figure 5.3), the temperature gradient across the interface can be estimated

$$\nabla T|_{mix} = \pm\frac{1\,\mathrm{K}}{\Delta} \cong \pm 48.83\,\mathrm{K\,m^{-1}}$$

The Brunt-Väisälä frequency is then computed out of the interfacial gradient. The squared internal Froude number that results

$$Fr_{int}^2 = \frac{u_{rms}^2}{\mathcal{N}^2 \ell_{mix}^2} \cong \pm 7$$

can be either positive or negative depending on the sign of $\mathcal{N}^2$. A negative value of Fr_{int}^2 is the hallmark of unstable stratification, which results in positive buoyancy for the interfacial parcel (Burnet & Brenguier, 2007). The experiment simulates decaying turbulence and hence Fr_{int}^2 is expected to tend to zero with time.

Parameters common to all simulations			
Quantity	Symbol	Value	Unit
Computational cube edge	H	0.512	m
Grid points (x1,x2)	n	512	-
Grid points (x3)	n_3	1024	-
Reference length	L_{ref}	8.15	cm
Reference velocity	U_{ref}	14.73	$\mathrm{cm\,s^{-1}}$
Kinematic viscosity (air)	ν	$1.5 \cdot 10^{-5}$	$\mathrm{m^2/s}$
Reference static temperature	T_{ref}	273.15	K
Reference droplet radius	R_{ref}	1	µm
Rerefence saturation pressure	$e_s(T_{ref})$	611	Pa
Reference saturated vapor density	$\rho_{sv}(T_{ref})$	4.8	$\mathrm{g/m^3}$
Kolmogorov length scale	η	0.7	mm
Grid resolution	Δx	1	mm
Average rms velocity	u_{rms}	0.078	$\mathrm{m\,s^{-1}}$
Average TKE dissipation rate	ε	0.04	$\mathrm{m^2/s^3}$
Taylor microscale Reynolds number	Re_λ	50	-
Physical parameters			
Dry air density at 1000 m	ρ_a	1.11	$\mathrm{kg/m^3}$
Boussinesq density at 1000 m	ρ_0	1.11	$\mathrm{kg/m^3}$
Liquid water density	ρ_w	1000	$\mathrm{kg/m^3}$
Gravity acceleration	g	9.81	$\mathrm{m/s^2}$
Initial mean temperature	T_{mean0}	281	K
Interfacial internal Froude number	Fr_{int}	± 7	-
Air-water vapor mass diffusivity	κ_v	$2.53 \cdot 10^{-5}$	$\mathrm{m^2/s}$
Thermal conductivity of air	K	0.028	$\mathrm{W\,m^{-1}\,K^{-1}}$
Schmidt number for water vapor	Sc_v	0.625	-
Prandtl number for clear air	Pr	0.72	-
Relative humidity (cloud cube)	RH_c	1.02	-
Relative humidity (clear air cube)	RH_a	0.7	-
Gas constant for water vapor	R_v	461.9	$\mathrm{J\,kg^{-1}\,K^{-1}}$
Gas constant for dry air	R_a	286.7	$\mathrm{J\,kg^{-1}\,K^{-1}}$
Water latent heat (liquid-vapor)	L_w	2.48	$\mathrm{MJ\,kg^{-1}}$
Specific heat at constant pressure	c_p	1146.8	$\mathrm{J\,kg^{-1}\,K^{-1}}$
Init. liquid water content (cloud)	LWC_0	0.8	$\mathrm{g/m^3}$
Init. droplet concentration (cloud)	N_0	74.5	$\mathrm{cm^{-3}}$
Kelvin coefficient	A	$2.45 \cdot 10^{-4}$	m
Hygroscopicity	k	0.7	-
Aerosol dry radius	r_{dry}	0.01	µm

Table 5.1: Parameters defined for all runs.

Direct numerical simulations: details					
Run	Fr_{int}^2	$t_{tot}/\tau_{\ell 0}$	DSD	Seeding	σ_{s0}
B001	∞	(test)	monodisperse	lower cube	0
B002	∞	13.9	polydisperse	lower cube	0
B003	-7	7.5	polydisperse	lower cube	0
B004	-7	10.4	monodisperse	lower cube	0
B005	-7	5.3	polydisperse	full domain	0
B006	-7	6	monodisperse	full domain	0
B007	7	7.3	polydisperse	lower cube	0
B008	-7	-	monodisperse	lower cube	0
B009	-7	-	monodisperse	full domain	0
B010	∞	-	monodisperse	full domain	0
B011	-7	-	monodisperse	lower cube	0
B012	-7	9.2	polydisperse	lower cube	0.022
B013	-7	6	monodisperse	lower cube	0
B014	-7	6	monodisperse	lower cube	0
B015	-7	6	polydisperse	lower cube	0
B016	-7	(test)	polydisperse	lower cube	0.022
B017	-7	7.3	polydisperse	lower cube	0.045
B018	-7	7.3	polydisperse	lower cube	0.045

Table 5.2: Specific parameters for the set of simulations.

5.4 Algorithm

The DNS have been carried out via the pseudo-spectral incompressible Navier-Stokes solver `TurIsMis`. Spectral methods are extremely accurate and widely used for HIT applications (Pope, 2000, p. 344). Derivatives (and so gradients, divergences and curls) are local operations in the Fourier space and do not require the access to data stored in neighbor cells in the physical mesh. A new minor release from version 14p (where p stands for particles) was written to include the Howell model (equation 2.11), the non-periodic temperature distribution (figure 5.3) and the polydisperse droplet distribution based on volume classes. The original software was developed by the Philofluid research group at Politecnico di Torino[6] basing on the parallel dealiased pseudospectral algorithm presented in M. Iovieno et al., 2001. Dealiasing is based on the 3/2-rule. Spectral discretization is achieved with a Fourier-Galerkin weighted residuals method. Time integration is carried out with a fourth-order Runge Kutta scheme (RK4). Boundary conditions in the physical space are periodic in all directions, that is (M. Iovieno et al., 2001)

$$V_i\left(\boldsymbol{x} + H\boldsymbol{e}_j, t\right) = V_i\left(\boldsymbol{x}, t\right) \quad \forall i, j$$

for both velocity (generic component V_i) and scalars. A parallel transposition is required to compute the convective term of the momentum equation. Three-dimensional fast Fourier transform is included via the FFTW package (http://www.fftw.org/). The code is written in Fortran and parallelized with the Message Passage Interface (MPI) standard. All runs were carried out on the Marconi Tier-0 system at CINECA between September 2019 and January 2020. Part of the post-processing activity was completed on the Hactar HPC cluster at Politecnico di Torino (http://hpc.polito.it/sistemi_hpc.php).

[6]Visit the official web page for a resume of the software releases https://areeweb.polito.it/ricerca/philofluid/software/95-turbulent-flows.html.

Chapter 6

Post-processing and results

The present work focuses on the evolution of flow and droplet statistics along the non-homogeneous direction across the interface (Bhowmick & Iovieno, 2019; M. Iovieno et al., 2014; Tordella & Iovieno, 2006, 2011, 19; Tordella et al., 2008). Basically, each statistical property is computed for a squared slice of the parallelepiped in figure 5.1. Each one of the n_3 slices is a set of samples that are used to compute the statistical moments and correlation coefficients.

Flow properties are point-wise and defined for each one of the $n^2 \times n_3$ points of the computational domain. Hence, for most cases - such as the flow fields, droplet concentration, inverse phase relaxation and saturation times - the set of samples is made with all the n^2 points of a plane. On the other hand some droplet properties - droplet mean radii, surfaces and volumes and growth coefficients - are defined only in non-void cells of the domain.

Each grid cell may contain a number of droplets. The cell-averaged values of the droplet properties (e.g. mean radius, mean concentration, mean growth coefficient etc...) are assigned to the cell itself. Therefore, a scalar field that defines the spatial distribution of a property is generated, and local statistics can be computed.

The inverse phase relaxation time 4.5 is considered to be meaningful over a statistically significant sample of droplets that are contained inside an arbitrary large volume (Khvorostyanov & Curry, 2014). Hence, in some DNS studies (e.g. Andrejczuk et al., 2009; Gao et al., 2018; Kumar et al., 2013; Kumar et al., 2014) evaporation and phase relaxation time scales are treated as global properties of each run. The same is done for the droplet concentration, mean volume and homogeneous mixing degree Ψ. Kumar et al., 2014 computed the trajectories of a set of droplet samples taken over 4 and 16 subvolumes (parallelepiped-shaped subslabs) in the $r - N$ mixing diagram. They verified that the mixing diagram trajectories that were computed over a larger number of thus smaller subslabs showed enhanced variability (which is somewhat expected) no substantial difference in the final $r - N$ coordinates was observed. Conversely, in the present work all

statistics will be computed over squared thin slices to show the variability across the interface. This may be important since two different adjacent turbulent regions are represented here in figure 5.1.

Statistics consider mean, standard deviation, skewness and kurtosis. The correlation coefficient of two properties X and Y is computed following the definition

$$\rho_{XY} = \frac{cov\,[X,Y]}{\sigma_X \sigma_Y} \tag{6.1}$$

with $cov\,[X,Y]$ being the covariance, which is linked to the correlation function R_{XY}

$$cov\,[X,Y] = R_{XY} - \overline{X}\,\overline{Y}$$

$\bar{\cdot}$ being the expected value operator.

6.1 Shearless mixing: flow field

Turbulence

Estimates of the kinetic energy, dissipation rate and enstrophy can be obtained through the saved velocity fields. Each component of the Fourier-space velocity field $\hat{\boldsymbol{V}} = \begin{bmatrix} \hat{u} & \hat{v} & \hat{w} \end{bmatrix}$ is stored in a $n^2 \times n_3$ array and saved into a binary file. The post-processing algorithm reads the binaries and computes the values for the local TKE [m^2/s^2],

$$\mathcal{K} = \frac{1}{2}\left(u^2 + v^2 + w^2\right)$$

TKE dissipation rate

$$\varepsilon = \frac{1}{\rho_0}\left(\boldsymbol{\tau} \cdot \nabla\right) \cdot \boldsymbol{V}$$

recalling equation 5.8, for $\nabla \cdot \boldsymbol{V} = 0$ one gets

$$\begin{aligned}
\frac{\varepsilon}{\nu} &= 2\left(\left(\nabla \boldsymbol{V} + [\nabla \boldsymbol{V}]^T\right)^T \cdot \nabla\right) \cdot \boldsymbol{V} = \\
&= \left(\begin{bmatrix} 2\dfrac{\partial u}{\partial x} & \left(\dfrac{\partial v}{\partial x} + \dfrac{\partial u}{\partial y}\right) & \left(\dfrac{\partial w}{\partial x} + \dfrac{\partial u}{\partial z}\right) \\ \left(\dfrac{\partial v}{\partial x} + \dfrac{\partial u}{\partial y}\right) & 2\dfrac{\partial v}{\partial y} & \left(\dfrac{\partial w}{\partial y} + \dfrac{\partial v}{\partial z}\right) \\ \left(\dfrac{\partial w}{\partial x} + \dfrac{\partial u}{\partial z}\right) & \left(\dfrac{\partial w}{\partial y} + \dfrac{\partial v}{\partial z}\right) & 2\dfrac{\partial w}{\partial z} \end{bmatrix} \cdot \begin{bmatrix} \left(\dfrac{\partial}{\partial x}\right) \\ \left(\dfrac{\partial}{\partial y}\right) \\ \left(\dfrac{\partial}{\partial z}\right) \end{bmatrix}\right)^T \cdot \begin{bmatrix} u \\ v \\ w \end{bmatrix}
\end{aligned}$$

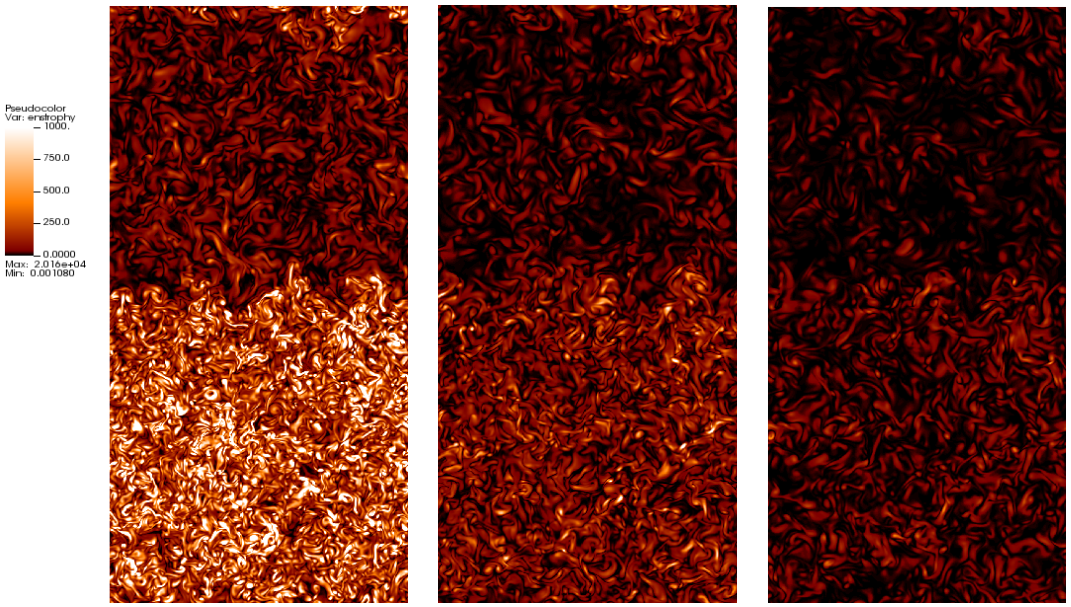

(a) 0.27 s ($t/\tau_0 \cong 0.9$) (b) 0.82 s ($t/\tau_0 \cong 2.7$) (c) 1.34 s ($t/\tau_0 \cong 4.5$)

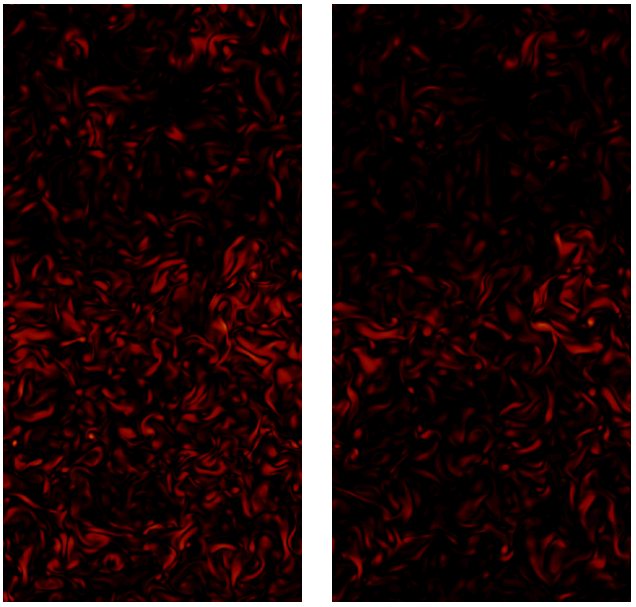

(d) 1.9 s ($t/\tau_0 \cong 6.3$) (e) 2.45 s ($t/\tau_0 \cong 8.2$)

Figure 6.1: Non-dimensional enstrophy for simulation B012. Legend shows values of $\widetilde{\mathcal{E}}$ ranging from 0 to 1000. Localized coherent bursts of vorticity can be observed (e.g. (a) and (b)). The cloud region is located at bottom of each figure.

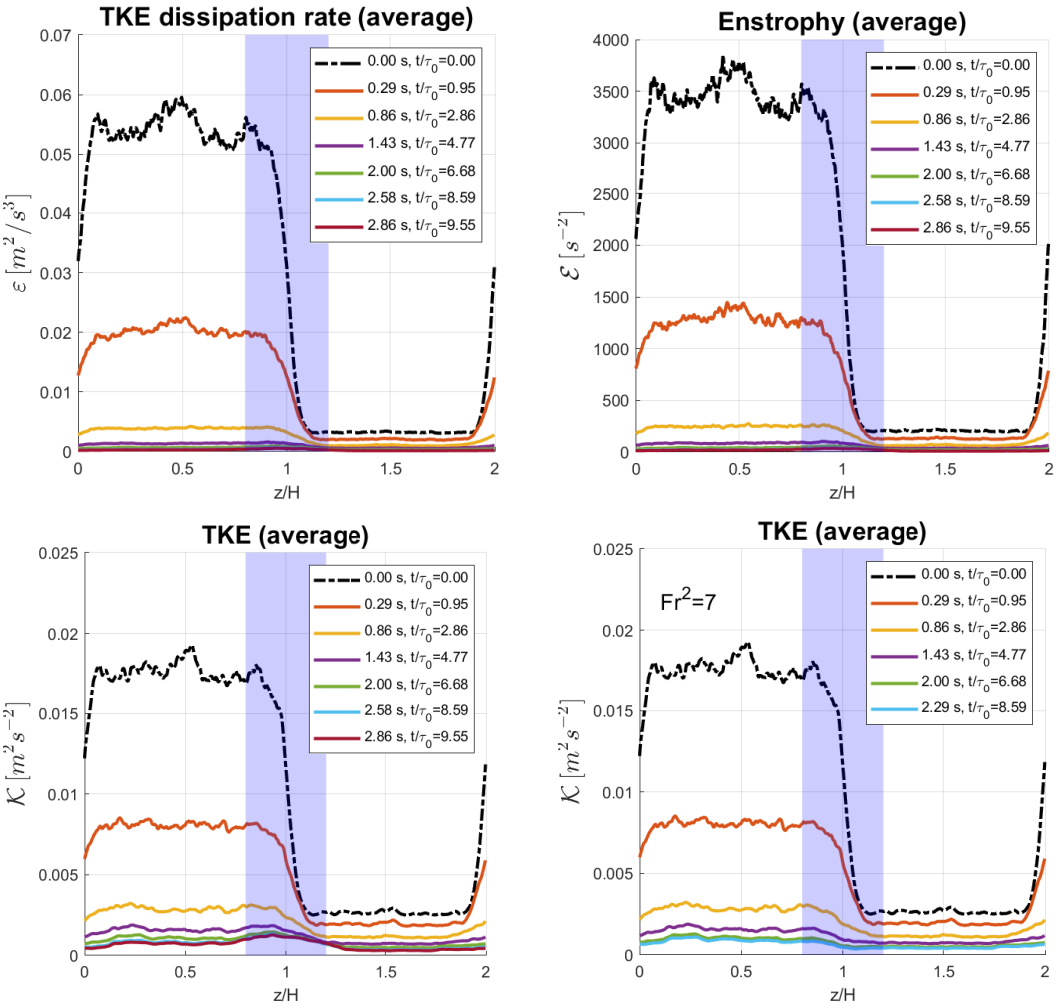

Figure 6.2: Trend of the homogeneous plane averages for ε, $\mathcal{E}$ and $\mathcal{K}$ for simulation B012. Bottom-right: evolution of the kinetic energy under stable-stratified conditions (B017). The effect of the internal Froude number is visible for $t/\tau_0 > 6$. Dash-dotted solid black lines represent the initial conditions ($t = 0$ s).

and

$$\frac{\varepsilon}{2\nu} = \left(\frac{\partial u}{\partial x}\right)^2 + \left(\frac{\partial v}{\partial y}\right)^2 + \left(\frac{\partial w}{\partial z}\right)^2 + \frac{1}{2}\left(\frac{\partial v}{\partial x} + \frac{\partial u}{\partial y}\right)^2 + \\ + \frac{1}{2}\left(\frac{\partial w}{\partial x} + \frac{\partial u}{\partial z}\right)^2 + \frac{1}{2}\left(\frac{\partial w}{\partial y} + \frac{\partial v}{\partial z}\right)^2 \tag{6.2}$$

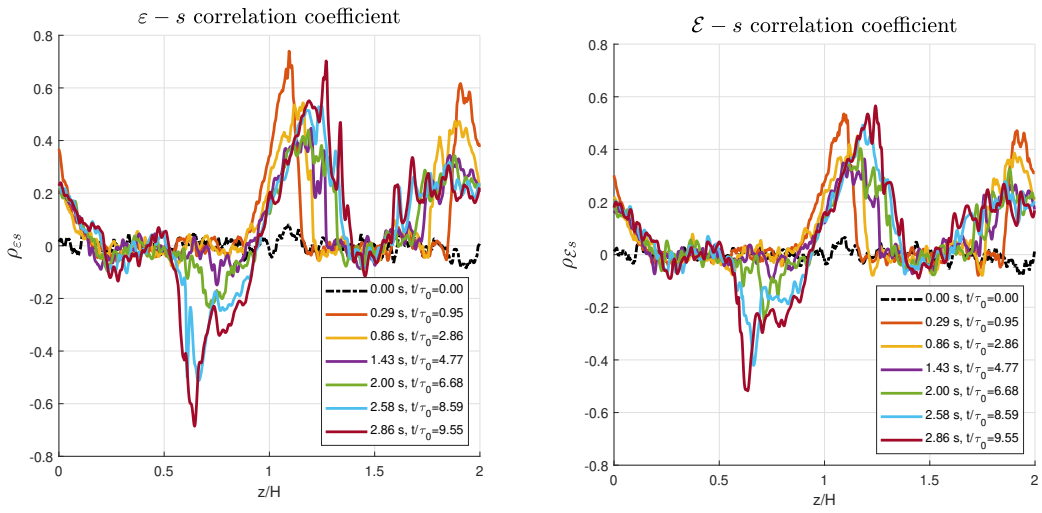

Figure 6.3: Dissipation-supersaturation and enstrophy-supersaturation correlation coefficient computed for each homogeneous plane across the interface for simulation B012.

and the enstrophy

$$\mathcal{E} = \frac{1}{2}\left[\left(\frac{\partial w}{\partial y} - \frac{\partial v}{\partial z}\right)^2 + \left(\frac{\partial u}{\partial z} - \frac{\partial w}{\partial x}\right)^2 + \left(\frac{\partial v}{\partial x} - \frac{\partial u}{\partial y}\right)^2\right]$$

Both quantities are defined as functions of the velocity derivatives therefore represent small scale properties of the turbulent flow. The derivatives are computed pointwise from the velocity fields saved in the Fourier space by multiplying the value of the velocity by the associated wavenumber. A parallel transposition is required during this process.

The trend of both the TKE dissipation rate, the enstrophy and the dissipation rate computed for the run B012 are shown in figures 6.2. The average value for each homogeneous plane defined by the vertical coordinate $x_3 = z$ is drawn as a function of the ratio z/H, H being the cube edge. The dissipation rate is higher in the cloud region and all quantities decrease rapidly during the first phase of the transient. After approximately three eddy turnover times, ε reaches values of the order of 10 cm^2/s^3 that are commonly found in cumulus and stratocumulus clouds (H. Siebert et al., 2006). Beyond this point, the kinetic energy, the enstrophy and the dissipation rate decrease slowly will reach a quasi-steady, globally homogeneous state across the interface. Hence, gravitational settling of the seeded particles is expected to occur being ($Fr_\eta \sim \varepsilon^{3/4}$). However, simulation B012 was run with an unstable initial temperature gradient, the cloud region being warmer than the

outside. This results in a little hump of the kinetic energy, a slight increase of its average value across the mixing region compared to both the cloud and the clear air slabs. The warmer air at the interface convects upwards and gains velocity. This injection of kinetic energy at the cloud interface may affect the mixing process by advecting some particles upwards in the subsaturated region. Also, the carrier advects the water vapor and the temperature (equations 5.26 and 5.29), which may lead to the detrainment of high-RH regions in the clear-air slab. Figure 6.3 show that both ε and $\mathcal{E}$ become positively correlated with the supersaturation above the interface as the shearless mixing progresses. The correlation coefficient (equation 6.1) is computed for each homogeneous plane. Both correlation coefficients show the same trends with close values, with some more intense peaks (both positive and negative) for the $\varepsilon - s$ case during the transient. Droplet clustering is unlikely to be significant as the simulation progresses, and no correlation between preferential concentration and supersaturation fluctuations is to be found. However, the fact that supersaturated regions may be significantly detrained above the interface be impact the growth of the droplet spectrum and mixing dynamics.

Snapshots of the enstrophy field in a $x_1 - x_3$ plane are shown in figure 6.1. Colors have been rescaled in order to provide a clear visualization of the low-energy structures that become more significant along the transient. The first picture is taken after approximately one initial eddy turnover time (that is $t/\tau_0 \sim 1$) and features regions of large enstrophy with peaks of $\widetilde{\mathcal{E}} \cong 60000$. Values of the kurtosis for the enstrophy distribution (not shown here) are around $30 \div 40$ in the cloud region. These values are a the hallmark of intermittency and coherent vortices are likely to exist in the first phases of the transient.

Water vapor, temperature and supersaturation

Runs `B012`, `B017` and `B018` have been initialized with fluctuating supersaturation fields. In order to obtain an appropriate initial variance for the supersaturation, a fluctuating scalar field was superposed to the smooth distribution depicted in figure 5.4. As stated in the previous chapter, temperature and supersaturation fields are non-periodic in the x_3 (vertical, inhomogeneous) direction.

Results from all runs except for the three mentioned below show that no supersaturation fluctuation is generated by the condensation process in the cloud core region. Conversely, the variance becomes non-null as the mixing widens down into the cloud. Anyway, even for the fluctuating runs (e.g. `B012`) the vapor field is smoothened readily by the diffusion (as seen in figures 6.5 and 6.7). Planar snapshots of the evolving supersaturation field from simulation `B012` (figure 6.4) show this attenuation inside the cloud slab.

The variance of the supersaturation σ_s (figure 6.7) decays uniformly in the cloud core. On the other hand, a huge peak appears at the mid-interface ($z/H \cong 1$). This

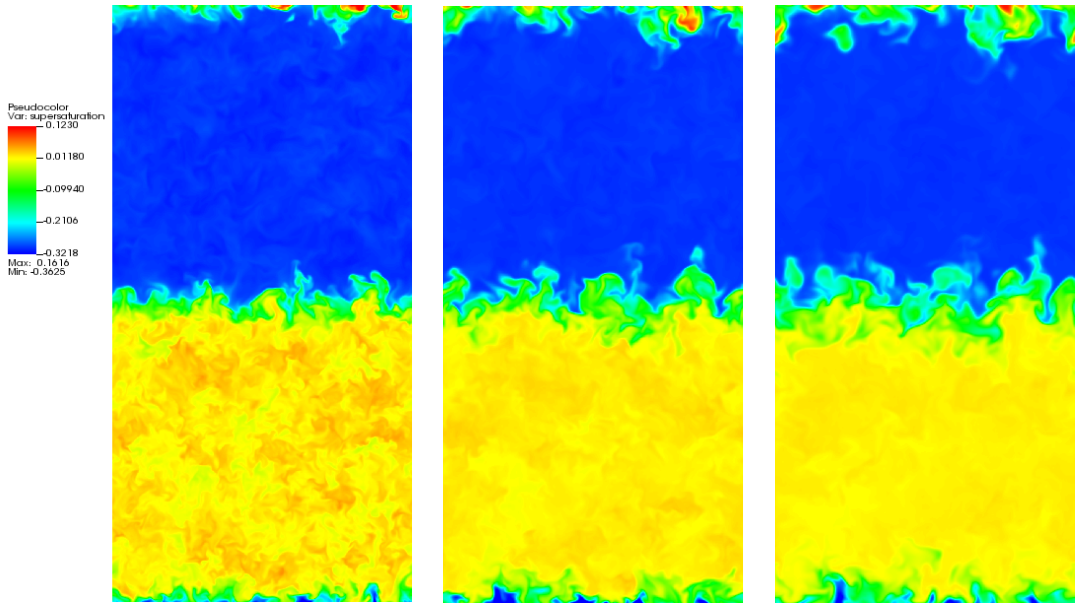

(a) 0.27 s ($t/\tau_0 \cong 0.9$) (b) 0.82 s ($t/\tau_0 \cong 2.7$) (c) 1.34 s ($t/\tau_0 \cong 4.5$)

(d) 1.9 s ($t/\tau_0 \cong 6.3$) (e) 2.45 s ($t/\tau_0 \cong 8.2$)

Figure 6.4: Supersaturation field computed in simulation `B012`. The colorbar ranges from $s = -0.32$ to $s = 0.12$. The cloud slab lies at the bottom.

is a result of the entrainment and detrainment plumes that are generated at the interface. Warmer supersaturated air is advected upwards and cooler, subsaturated

air is entrained downwards. There, floating droplets experience a wide variety of growth conditions that are likely to lead to a broadening of the droplet spectrum, something that is likely to be observed for initial monodisperse distributions.

By comparing the enstrophy and the supersaturation snapshots (figures 6.1 and 6.4) one can notice similar patterns, especially in the interfacial regions for $t \gtrsim 6\tau_0$. The plume originating at mid-right shows a high

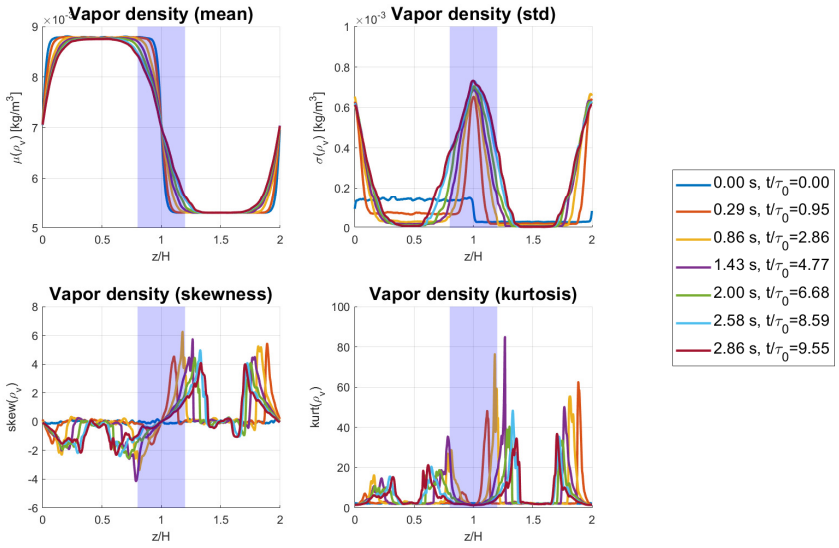

Figure 6.5: Statistics of the water vapor field for simulation B012. In order to generate a fluctuating initial condition for ρ_v, a zero-mean turbulent scalar field was superposed to the smooth distribution of figure 5.4.

6.1.1 Integral length scale

The spectral method: algorithm issues

The integral scale can be computed by extracting the turbulent energy spectrum $E(\kappa)$ from the datasets. To get the spectrum of a specific region of the physical domain (e.g. the full parallelepiped, one of the cubes or a smaller chunk made up with a few homogeneous planes), one must transform the velocity field $\boldsymbol{u}$ of the subdomain into the Fourier space via a 3D Fast Fourier Transform

$$\boldsymbol{V}\left(x_1, x_3, x_2\right) \longrightarrow \hat{\boldsymbol{V}}\left(\kappa_1, \kappa_2, \kappa_3\right)$$

the obtained transformed field must be normalized over the total number of cells (e.g. if one is transforming the full domain, then normalizes the spectral velocity

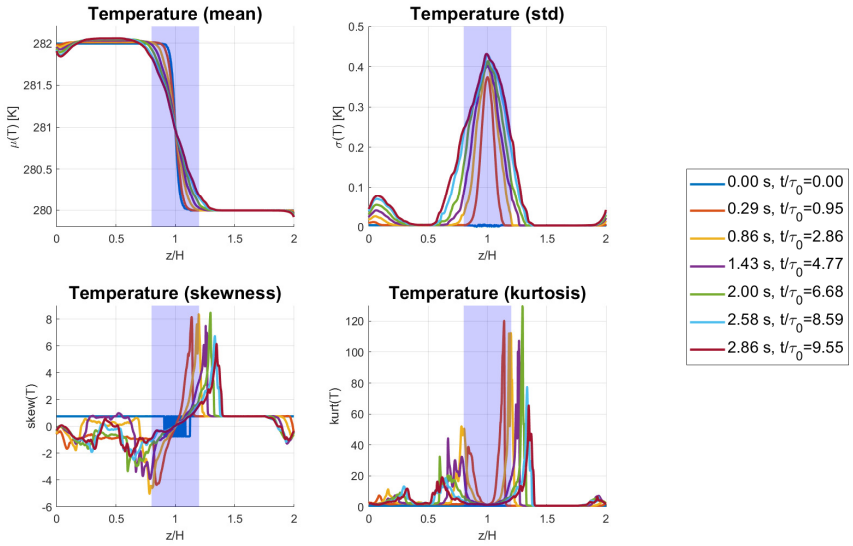

Figure 6.6: Statistics of the non-periodic temperature field for simulation B012 (see also figure 5.3).

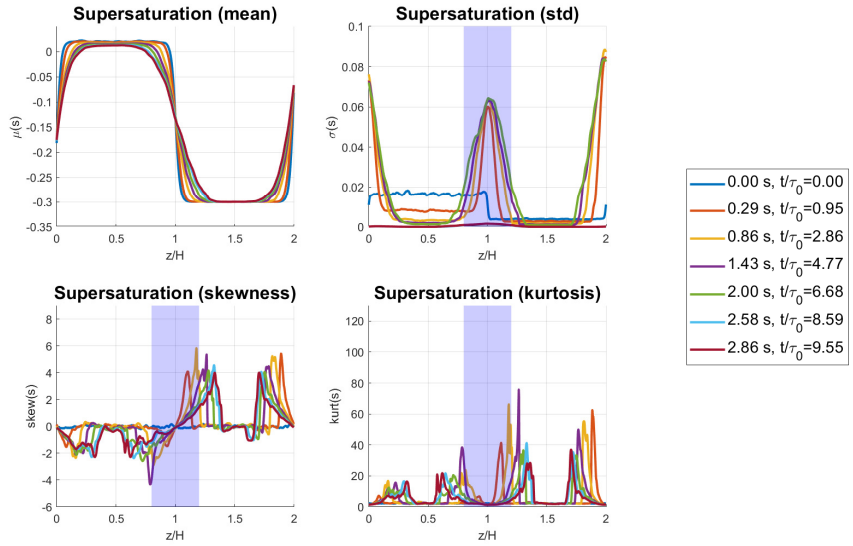

Figure 6.7: Statistics of the non-periodic supersaturation field for the simulation B012. Variance decays in the cores and increases in the mixing regions.

field over $n^2 n_3 = 512^2 \cdot 1024$). Each point of the Fourier field is associated to a set of wavenumbers whose modulus is $|\boldsymbol{\kappa}| = \sqrt{\kappa_1^2 + \kappa_2^2 + \kappa_3^2}$. One can take the squared

modulus $\hat{\boldsymbol{V}}^T\hat{\boldsymbol{V}}$ of each point and add its contribution to the specific wavenumber $|\boldsymbol{\kappa}|$ in the spectrum $E(\kappa)$.[1]

The energy spectrum is related to the mean squared velocity and the kinetic energy of the zero-mean flow velocity turbulent flow, one can follow the definition given in Pope, 2000, chapter 6 and appendices. If the specific subdomain is statistically homogeneous and isotropic the autocorrelation function of the velocity field is

$$\boldsymbol{R}_{VV}(\boldsymbol{r}) = \overline{\left[\boldsymbol{V}(\boldsymbol{x})\,\boldsymbol{V}(\boldsymbol{x}+\boldsymbol{r})^T\right]} \tag{6.3}$$

The autocorrelation of the velocity field can be inverse-Fourier transformed into the power spectral density $E(\kappa)$

$$\boldsymbol{R}_{VV}(r) = \iiint_{-\infty}^{+\infty} \boldsymbol{E}(\boldsymbol{\kappa})\, e^{j\boldsymbol{\kappa}\cdot\boldsymbol{r}} d\boldsymbol{\kappa} \tag{6.4}$$

The integral in equation 6.4 is defined in spherical coordinates in the wavenumber space. However, to make things more simple, the algorithm used here computes an approximation of such integral in rectangular coordinates. Taking $\boldsymbol{r} = 0$ and considering only the wavenumbers' moduli $k = |\boldsymbol{k}|$, the integral 6.4 reduces to

$$R_{VV}(0) = 8\int_0^{+\infty} E(\kappa)\, d\kappa$$

The energy spectrum is computed as described below. Each wavenumber κ is approximated to its nearest integer. By integrating this formulation all over the wavenumber spectrum, one gets an estimate of the kinetic energy.

Once the spectrum is obtained, the longitudinal integral length scale can be estimated as a weighted average of the spectrum contribution over the wavenumbers (Monin and Yaglom, 2013, p. 55)

$$\ell = \frac{3}{4}\pi \frac{\int_0^{\infty} \kappa^{-1} E(\kappa) d\kappa}{\int_0^{\infty} E(\kappa) d\kappa} = 0.0176\, m \tag{6.5}$$

The estimated eddy turnover time can be derived by equation 5.34.

This method provides a good approximation of the turbulent spectrum only when computed over a wide 3D domain, that is when the spectrum domain's aspect ratio is greater or equal to 1. If one uses it to compute the 3D spectrum and the integral scale of a thin slice, some spurious oscillations will appear (see figure 6.9). This may be due to the fact that, in the Fortran routine, the spectrum is

[1]The algorithm that was used has been implemented in a Fortran code by the Philofluid Research Group of the Politecnico di Torino https://areeweb.polito.it/ricerca/philofluid/.

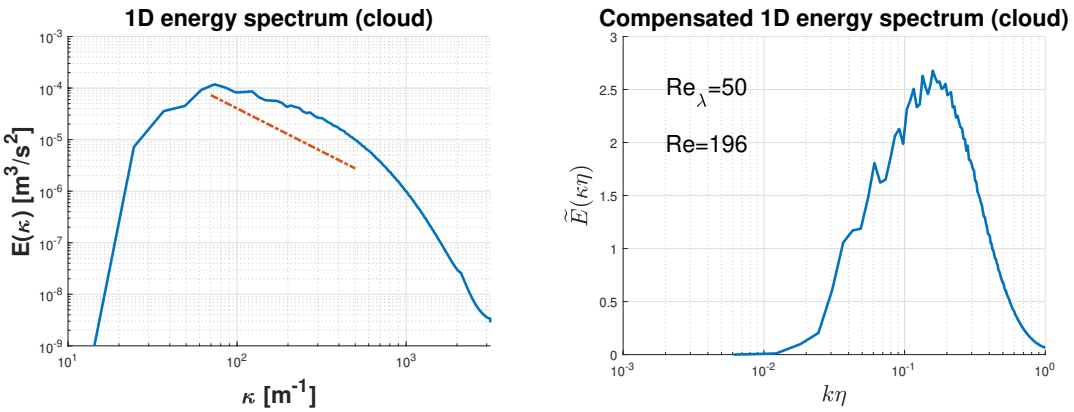

Figure 6.8: Left: one-dimensional energy spectrum of the cloud cube obtained using the Matlab `fftn` function (simulation **B002**, time 0 s). The orange dash-dotted line is the theoretical trend $E(\kappa) = C_\kappa \varepsilon^{2/3} \kappa^{-5/3}$ 3.5 for $\varepsilon \cong 550$ cm^2/s^3 with $C_\kappa = 0.6$. Right: compensated energy spectrum $E(\kappa)\varepsilon^{-2/3}k^{5/3}$. As expected, no stable plateau is observed. The energy bump in $\kappa\eta \sim 0.1$ must not be confused with the inertial subrange. See (Ishihara, Gotoh, & Kaneda, 2009) for a review of the compensated spectra obtained via high-Reynolds DNS.

computed in rectangular coordinates by taking into account the contribution of the wavenumber modulus κ (that is the radius of the spherical coordinate system) over a coarse discretization in the wavenumber space. In any case, by implementing the routine in Matlab (through the use of the library function `fftn`) one observes that the Parseval theorem is satisfied if an appropriate normalization is chosen. This does not occur - for some reasons that we still do not know - in the Fortran routine that uses the FFTW library. This implementation requires further investigation and debugging to find the appropriate normalization.

However, if ones computes the turbulent spectrum over a 512-points-edge cube considering also the wavenumbers in the homogeneous directions, then will get a slightly higher estimate of the integral scale (equation 6.5):

$$\ell = \frac{3}{4}\pi \frac{\int_0^\infty \kappa^{-1} E(\kappa) d\kappa}{\int_0^\infty E(\kappa) d\kappa} = 0.0249\, m$$

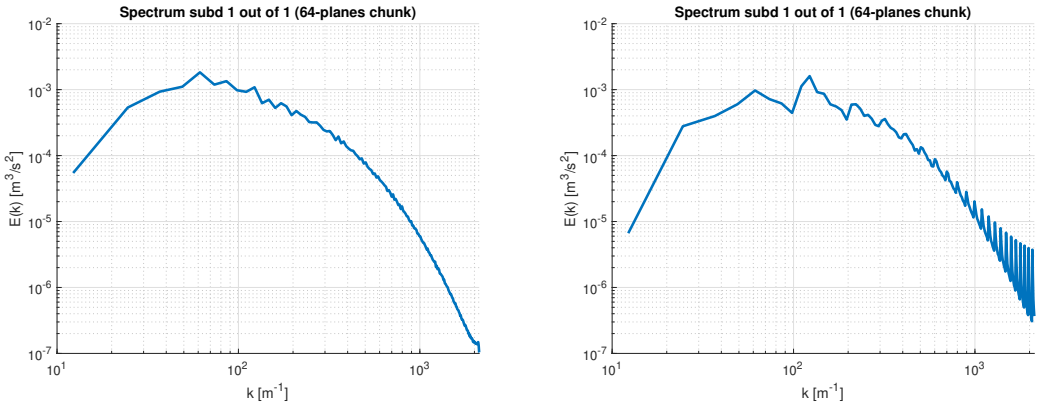

Figure 6.9: The spectrum algorithm can be computed over different chunks (that is slices of the physical domain) each one being made up with several homogeneous planes. In this figure, the three-dimensional spectrum of a 64-plane chunk by neglecting (left) and taking into account (right) the contribution of the wavenumbers in the non-homogeneous direction in the Fourier space. Spurious oscillations appear once the κ_3 wavenumbers contribution is taken into account. They are probably due to the rectangular coordinates approximation and to a coarse wavenumber discretization at the small scales.

Autocorrelation computation

Another way to get an estimate of the integral scale is through its definition based on the autocorrelation (two-point correlation) function (Tordella & Iovieno, 2006)

$$\ell = \frac{1}{3} \sum_{V_i V_i} \frac{\int_0^{+\infty} R_{V_i V_i}(r)\, dr}{R_{V_i V_i}(0)} \tag{6.6}$$

calculated for all the components of the velocity vector field and averaged. In this case we can denote $u = V_i$ as a component of $\boldsymbol{V}$. The autocorrelation function must be computed along each homogeneous direction in the physical space in every point and averaged. The periodic boundary conditions allow for the computation across a finite distance $r = n$ that assumes a cyclic permutation. An algorithm of this kind:

```
Ruu(:)=0.0d0
do r=0,n-1
do j1=0,n-1
do jx=0,n-r-1
    jstart=j1+jx
```

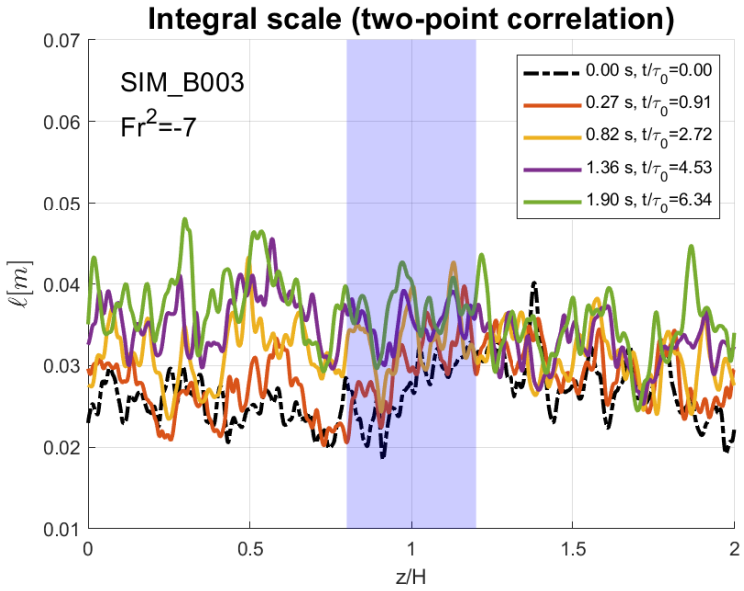

Figure 6.10: Estimates of the two-dimensional longitudinal integral length scale computed for each *homogeneous* $x_1 - x_2$ plane. Equations 6.7 and 6.3. Data retrieved from run `B003`. The solid dash-dotted line indicates the initial condition.

```
      jend=mod(j1+jx+r,n)
      Ruu(r)=Ruu(r)+u(jstart,j3,j2)*u(jend,j3,j2)
   end do
   end do
   Ruu(r)=Ruu(r)/float(n-r)/float(n)
   end do
```

still results too much time-consuming to be adopted. Instead, if one considers the homogeneity of the field then can remove the loop `do j1=0,n-1` by setting `j1=0` and compute the correlations with respect to this point. The operation can be repeated along every parallel row (that is, the rows that are normal to the $x2$ distributed direction). Results obtained by each processor can be subsequently reduced using the `MPI_REDUCE` (`MPI_SUM`) function.

The autocorrelation function over a space interval r of an array-signal made up with n elements is given by (recalling equation 6.3):

$$R_{uu}(r) = \frac{1}{n-r} \sum_{j}^{n-r} u(x_1, x_3, x_2)\, u(x_1 + r, x_3, x_2) \tag{6.7}$$

The integral of the correlation function over different ranges r is given by

$$\int_0^{+\infty} R_{uu}(r)\, dr = \sum_{r=0}^{n} R_{uu}(r)\, \frac{\Delta x}{L_{ref}}$$

Moreover, one must consider that the set of periodic boundary conditions also imply the periodicity of the autocorrelation in every spatial direction (equation 6.7). Thus, in order to get a physical estimate of the integral scale ℓ one should integrate the autocorrelation function over a smaller range of r, typically over half the periodic distance.

To compute the correlation in the distributed direction a parallel transposition between the homogeneous directions is required, and can be obtained using the `MPI_SEND_RECV_REPLACE` function (see the algorithm description in (M. Iovieno et al., 2001)). The process is repeated and the results are averaged with the one obtained in the first direction. Results are shown below and seem to be in good agreement with the estimates that were made in the pre-processing phase.

Results for the first time step show good agreement with the value of the integral scale that was found using the spectral method and taking into account the contribution of the wavenumbers in the homogeneous direction only.

6.2 Droplets and temporal scale

Droplet statistics include concentration, mean radius, mean surface, mean volume, mean growth coefficient. Only relatively small ($r \lesssim 50$ µm) spherical drops are simulated in the present work. Droplet position, velocity and radius are saved at each time step and assigned to a specific cell of the mesh in the physical space. The local droplet concentration is estimated by counting the number of drops in the cell and averaging the total with respect to the cell volume $\Delta x^3 = 1$ mm^3. Statistics are then computed over the homogeneous plane, by taking into account all the n^2 cells.

Mean radius, surface and volume are computed by averaging over the non-void cells of each plane $n^2 - [number\, of\, void\, cells]$. The second, third and fourth-order moments are computed the same way.

The evolution of droplet concentration and mean radius distributions along the vertical direction are shown in figure 6.12. Droplet concentration drops near the mid and bottom interfaces while maintaining a peak close to the initial value for $z/H \cong 0.4$. Droplets that settle below $z/H = 0$ are killed and many small drops that are found in the sub-saturated region at the bottom are likely to evaporate and disappear. Conversely, some droplets are advected within the interfacial updrafts to the clear-air region. The mean radius averaged signal in the interfacial region is noisy, meaning that contiguous planes may have very different average

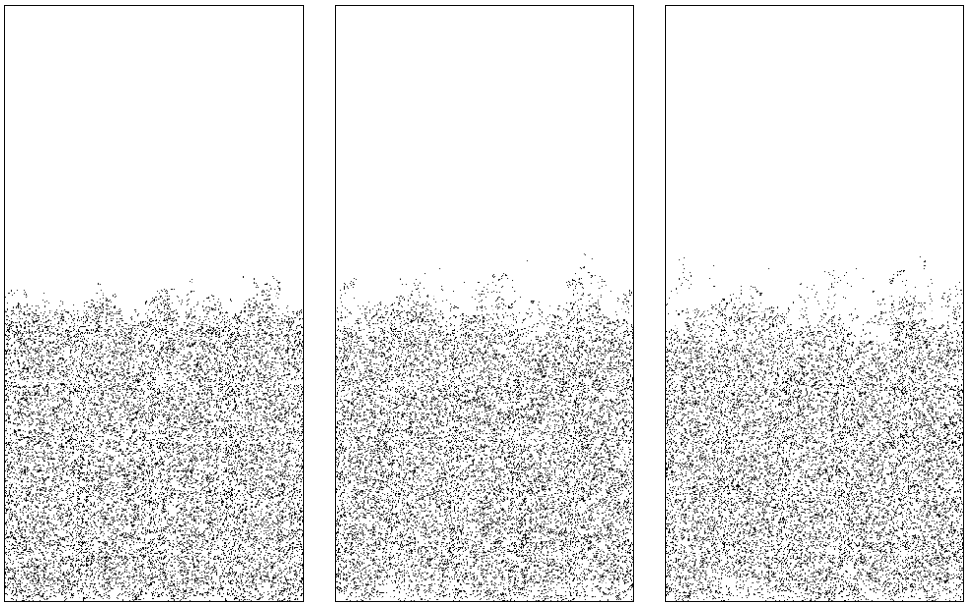

(a) 0.27 s ($t/\tau_0 \cong 0.9$) (b) 0.82 s ($t/\tau_0 \cong 2.7$) (c) 1.34 s ($t/\tau_0 \cong 4.5$)

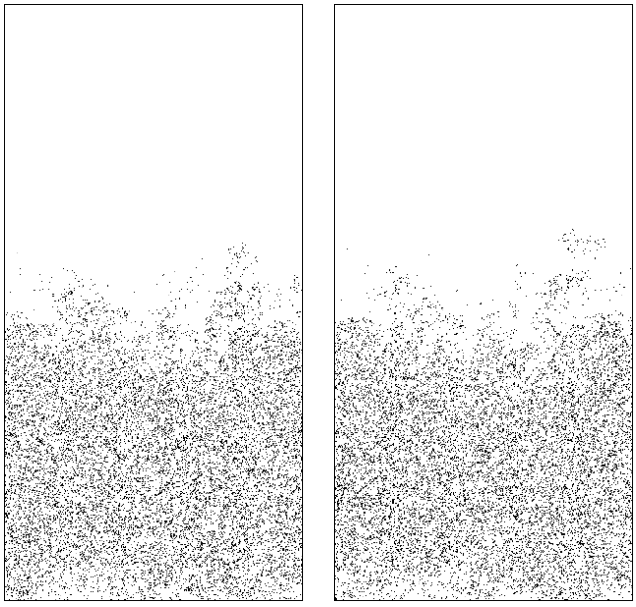

(d) 1.9 s ($t/\tau_0 \cong 6.3$) (e) 2.45 s ($t/\tau_0 \cong 8.2$)

Figure 6.11: Droplet distribution throughout the transient (plane $x_1 - x_3$, $x_2 = 1 \div 3$), run `B012`. Black dots indicate non-void cells.

values. This region is characterized by high level of small scale anisotropy and high supersaturation variance. Hence, droplets are likely to experience a wide variety of

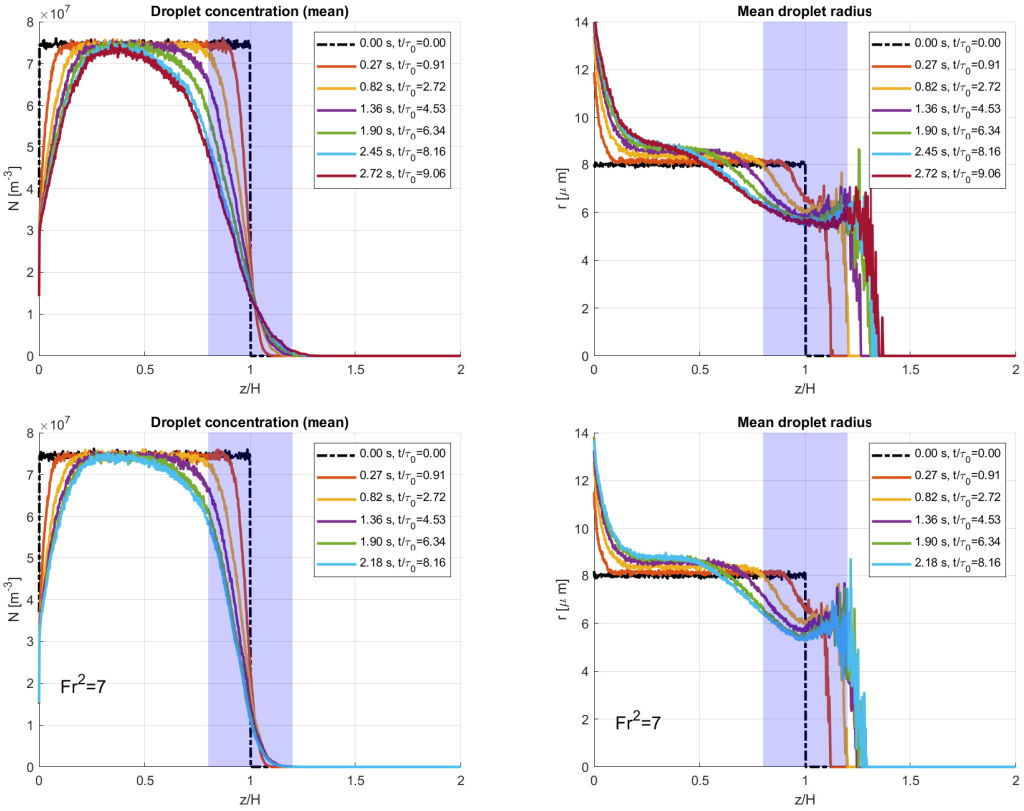

Figure 6.12: Top: droplet concentration and droplet mean radius (right) under unstable stratifications (B012). Bottom: same under stable conditions (B007).

condensational growth conditions. Droplet clustering and collisional growth may be fostered by a local increase of the kinetic energy due to the unstable interfacial temperature gradient ($Fr_\eta \sim \varepsilon^{3/4}$). Droplet clustering may be spotted by observing a snapshot of the droplet field as in figure 6.11. While no large-scale preferential concentration seems to take place, it may be found at smaller scales and (or) in the mixing region. By smoothing the droplet velocity fields and taking the divergence, one could make a valuable estimate of droplet clustering (equations 3.11). This is something that may be done in future DNS studies. However, particles with larger St (larger radii) tend to settle and are subject to slower shrinking rates (recall that by equation 1.1 one has $dr/dt \sim 1/r$), meaning that the mean radius increases monotonically as $z/H \to 0$.

Similar trends are observed for stable and neutral stratification in smooth, non-fluctuating vapor fields, thus suggesting that these conditions do not influence these variable considerably.

It can be shown (Khvorostyanov and Curry, 2014, pp. 144-148) that, if all

psychrometric and kinetic corrections ($\alpha_T \sim 1$) are neglected, under the limit of $K'_v \to \infty$ the condensational growth coefficient C_r 2.15 reduces to

$$C_{rk} \cong \frac{e_s D'_v \mathcal{M}}{\rho_w R T}$$

and the phase relaxation time 4.5 can be expressed as a function of the local droplet mean radius and spatial concentration

$$\tau_p^{-1} = 4\pi D'_v N \overline{r} \tag{6.8}$$

As for the droplet mean radius and concentration, the statistics of the phase relaxation time (equations 4.5 6.8) also show a behavior which is independent of both stratification and supersaturation fluctuations during the simulated transients. The plane-averaged distributions for the inverse phase relaxation time τ_{phase}^{-1} 6.8,

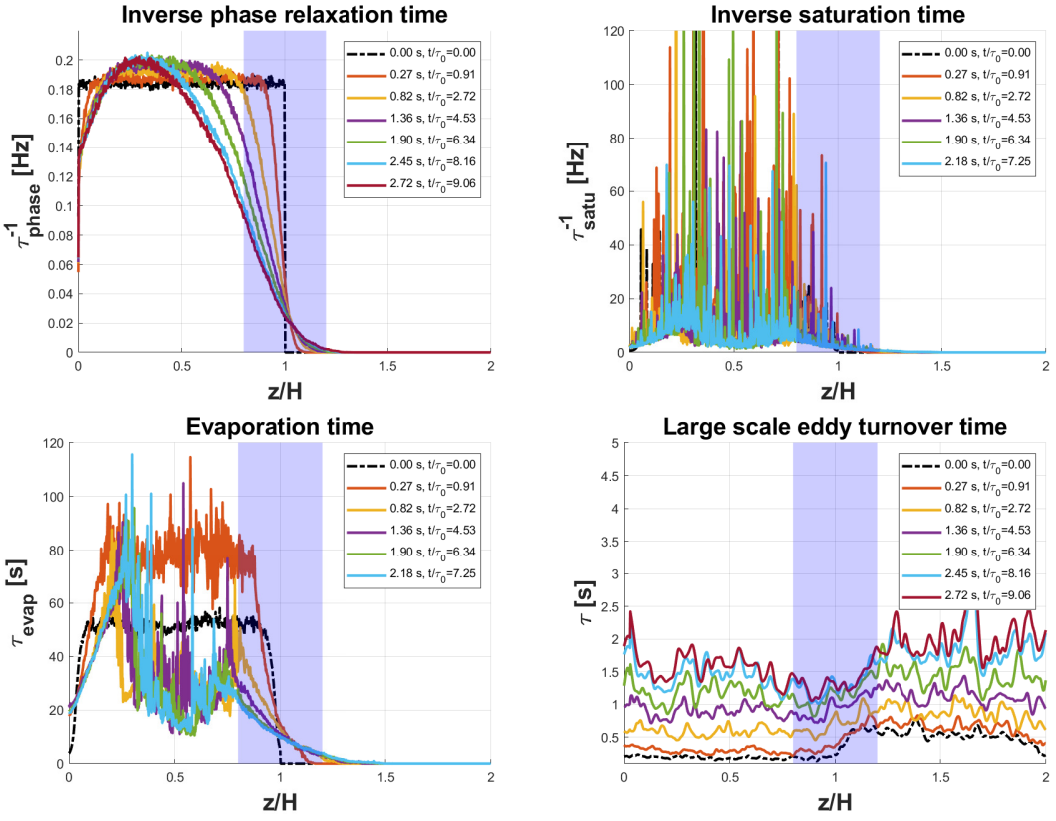

Figure 6.13: Droplet-phase time scales compared to the locally-averaged large scale eddy turnover time τ 5.34.

inverse saturation time τ_{satu}^{-1} 4.6 and evaporation time τ_{evap} 4.4 are shown in figure

6.13. Statistics of τ_{evap} and τ_{satu}^{-1} are obtained as ensemble average of simulations `B012`, `B017` and `B018` and show some noise. These time scales concur in the definition of the large scale Damköhler number Da_ℓ. Several studies have identified the microphysical time scale (equation 3.13 with the phase relaxation, evaporation and reaction time scale.

6.3 DSD spectral broadening

We wish to verify whether the results obtained by Chandrakar et al., 2016 are comparable to the ones that we have listed here or not. In their paper from 2016, Chandrakar et al., 2016 describe a set of experiments they had run in a laboratory chamber where moist Rayleigh-Bénard convection can be generated. The bottom surface of the chamber was maintained at 7 °C and the top at 21 °C. As steady state conditions were reached, aerosol injection began at a fixed rate allowing droplets to nucleate, grow and eventually precipitate. By adopting a stochastic condensation model also used by Sardina et al., 2015, 18 (see for instance Pope, 2000 for the Langevin equation and Khvorostyanov and Curry, 2014 for the Chapman-Kolmogorov model) they found that, under strict statistically steady-state conditions, the variance rate of the droplet surface can be expressed as a function of C_r, σ_s and with the large-scale, phase relaxation time-defined Damköhler number

$$\frac{d\sigma_{r^2}^2}{dt} = \frac{8C_r^2\sigma_{s0}^2\tau}{(1+Da)^2} \tag{6.9}$$

with τ denoting the turbulent correlation time (that is, the eddy turnover time) which was estimated to be around 2 s. The supersaturation was observed to be Gaussian with standard deviation $\sigma_{s0} = 0.014$ in absence of droplets. The droplet growth rate is $C_r = 109 \cdot 10^{-12}$ m^2/s. All factors of the time derivative in equation 6.9 are assumed to remain constant in time, thus allowing to get an estimate of the final surface variance after a typical residence time τ_{res}, that they estimated to be around 10 minutes (600 s). The variance strongly depends on the Damköhler number, and thus on the droplet mean radius and concentration in the chamber. Different Da are associated to different aerosols injection rates.

The object of our simulation is slightly different:

- a transient is investigated in this work. The Langevin equation doesn't describe decaying turbulent flows, therefore the model adopted by Chandrakar et al., 2016 should not describe, in principle, that growth dynamics that characterize these transients.
- the results presented here come from the simulation of the interaction between two turbulent regions having the same integral scale but different kinetic

energy levels. The mixing layer that arises is inhomogeneous, anisotropic and intermittent (Tordella et al., 2008).

- during their experiment, Chandrakar et al., 2016 a constant aerosol injection rate. This allows for statistically-steady droplet concentration and phase relaxation times to be observed in the experimental chamber. Conversely, aerosol activation is not considered here.

- a study by Siebert and Shaw Holger Siebert and Shaw, 2017 also shows that fluctuations of the relative humidity (and the supersaturation) should be normally distributed with a standard deviation close to 1%. This is consistent with the results shown by Chandrakar et al., 2016. Moreover, Holger Siebert and Shaw, 2017 show that - in the slow microphysics regime ($Da \leq 1$) - droplets do not act effectively as *buffers* for the supersaturation field, whose fluctuations become important allowing for different growth conditions. By choosing a 3D homogeneous supersaturation field as initial condition for a DNS, one is not able to observe supersaturation fluctuations due to turbulence in the cloud and clear air cores at low Damköhler numbers, (i.e. for homogeneous mixing conditions). Since all the present simulations reside in the low Da limit, this represents a considerable limit for the time scales analysis.

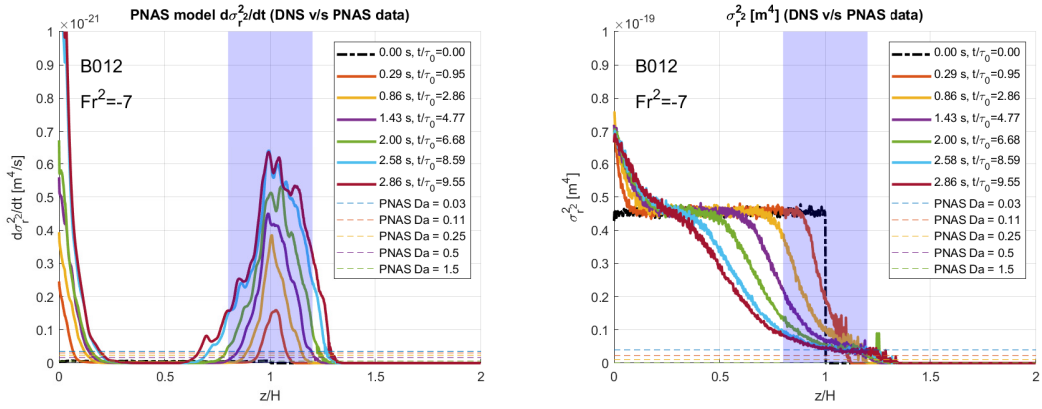

Figure 6.14: Left: spectral broadening rate computed following the steady-state formulation 6.9 by Chandrakar et al., 2016 (left). Right: variance of the mean droplet surface (expressed as mean squared radius) as computed from the simulation results (run B012).

In order to overcome some of these limitations, fluctuating vapor fields have been adopted as initial conditions for the runs B012, B017 and B018. Even in these cases the temperature field had been kept smooth and non-fluctuating. Basically, by modulating the initial amplitude for the vapor field, one can get desired

supersaturation fluctuating conditions. Chandrakar et al., 2016 had found that supersaturation fluctuations were nearly Gaussian with zero-mean and a standard deviation of 0.014. The main issue is that the amplitude of these fluctuations decays readily with the flow, and this is why no match between the condensational growth rate (equation 6.9) and the broadening of the droplet spectrum is found (figure 6.14). However, a small broadening of the DSD spectrum (droplet radii) is found during the simulation, as some large ($\geq$ 30 µm) droplets are found (figure 6.15).

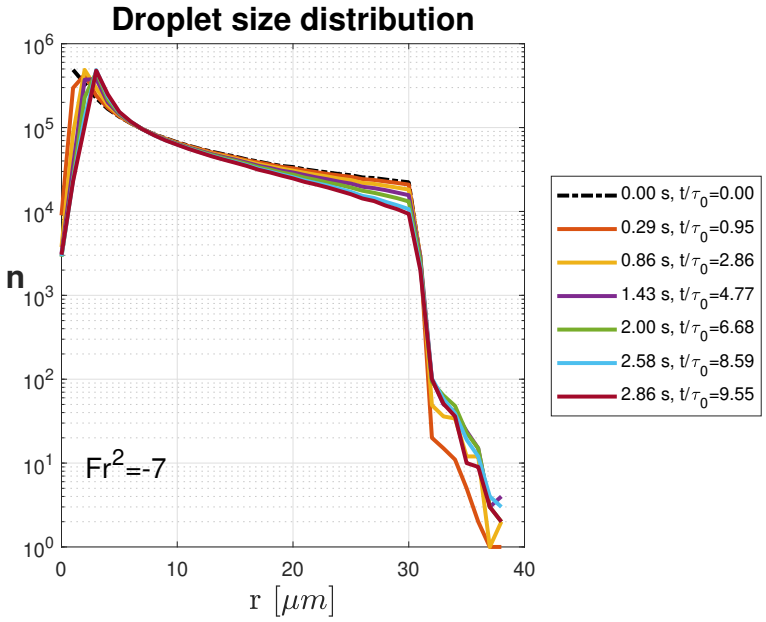

Figure 6.15: Evolution of the DSD distribution for a multidisperse, supersaturation fluctuating run (B012).

The results in figure 6.14 suggest there's probably no direct correlation between the steady-state model and the observed results. The variance of the surface spectrum is reduced in the mixing region as time elapses, probably due to gravitational settling. By contrast, surface variance is found to be higher at the bottom. This can be explained as a combined effect of both droplet sedimentation and the entrainment of subsaturated plumes that shrink small drops.

6.4 Homogeneous mixing degree

One of the most widely used parameters to quantifying the grade of homogeneous mixing on experimental (mostly in-situ or numerical) data is the homogeneous mixing degree Ψ (Gao et al., 2018; Lu et al., 2013). It can be defined as follows

(Lu et al., 2018)

$$\beta = atan\left(\frac{1-\frac{r_c}{r_a}}{\frac{n_0}{n_a}-\frac{n_c}{n_a}}\right) \tag{6.10}$$

and

$$\begin{aligned} \Psi &= \frac{2\beta}{\pi} \qquad n_c < n_0 \\ \Psi &= \frac{2\beta}{\pi} + 2 \quad n_c \geq n_0 \end{aligned} \tag{6.11}$$

with reference to figure 3.2. N_a and r_a are the initial (adiabatic) values. N_0 refers to the concentration reached for a given final value of α as the moist mixing parcel undergoes an extremely homogeneous transformation from point 2 to point 3.

Following Lu et al., 2018, the correlation between local values of the homogeneous mixing degree and the microphysical time scales can be compared. The value of their single-point correlation coefficient can be computed for each squared plane across the interface. This may give some insight on the ability of each of the time scales discussed below (see also figure 6.13) to well represent the mixing dynamics at the interface. Lu et al., 2018 worked on a similar analysis from in-situ made measurements and data provided by a one-dimensional simulation model. Unfortunately, for computational reasons, the point-wise value of the reaction time scale could not be computed. Lehmann et al., 2009 argued that the reaction time, instead of the phase relaxation or the evaporation time, may represent a valuable estimate of the microphysical time scale used to derive the Damköhler number. Following Burnet and Brenguier, 2007, the mixing diagram 3.3 drawn as explained in chapter 3 has been fulfilled with scattered points (experimental data) marking the plane-averaged values of $\overline{r^3}$ and N. The result is shown in figure 6.16. Two

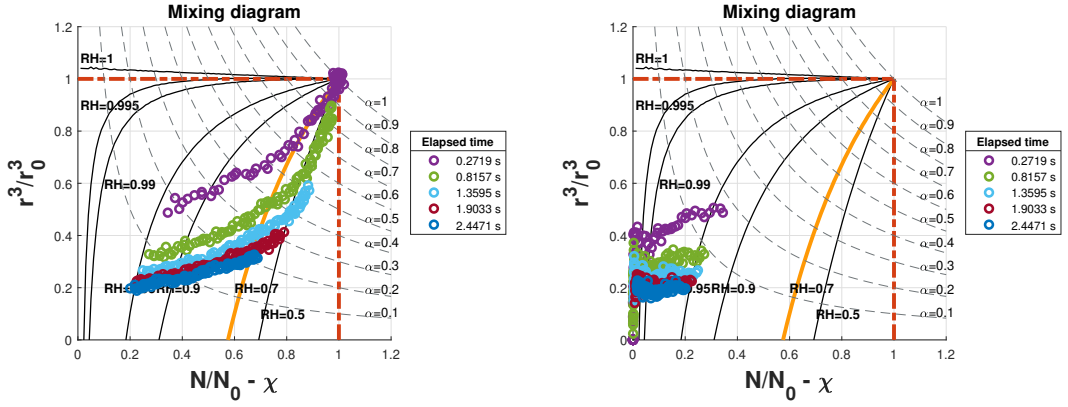

Figure 6.16: Mixing diagrams. Planes $z/H = 0.8 \div 1$ (left) and $z/H = 1 \div 1.2$ (right).

plots have been made, for both the lower and upper part of the mixing region. By taking a look on the plots of the scalars, one can assume that the mixing region extends over the blue-shaded area with $z/H \in [0.8,1.2]$. One can notice that the distribution tends to be more inhomogeneous as time elapses and the value of z/H is increased. The distribution initially follows the homogeneous mixing curve for $RH_e = 0.7$ (with e being the clear air environment value) and subsequently drifts towards more inhomogeneous values. Estimates for the reaction time scale

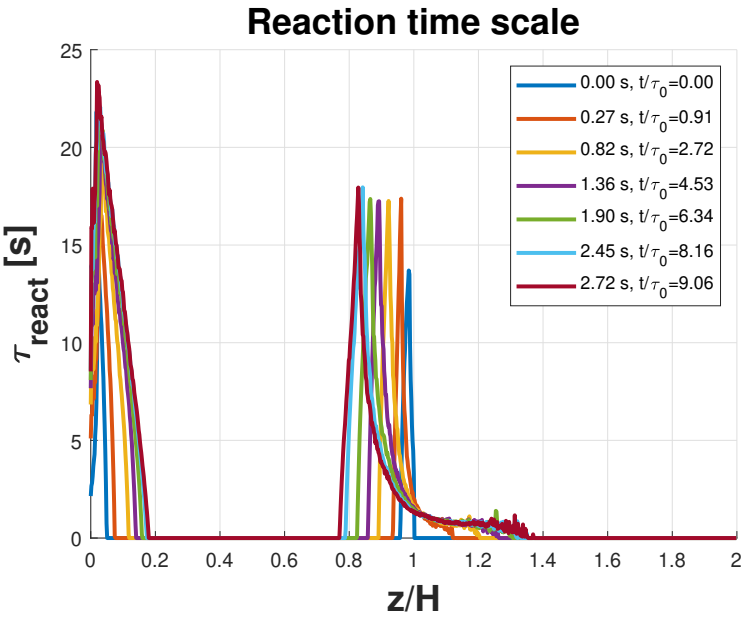

Figure 6.17: Estimated values for τ_{react}, run B012.

4.7 can be computed from the average values of Cr, $\overline{r}$, s and τ_{phase}^{-1}. Results are shown in figure 6.17. τ_{react} decreases above the top interface, meaning that the large scale Damköhler number Da may become of order one or even greater in this region. Also one may assume, by observing the average trends in figure 6.13, the phase relaxation time to be the prevalent temporal scale for $z/H \cong 0.9$. By contrast, the evaporation time may better describe the inhomogeneous nature of the upper part of the mixing region. This is consistent with the fact that in highly subsaturated regions droplet evaporation may occur without sensibly affecting the local vapor density. On the other hand and as pointed out by Lu et al., 2018 the phase relaxation time is the characteristic time of supersaturation variations due to variations of the liquid water content, regardless of whether such variations are due to a change in $\overline{r}$ or N.

Figures 6.16 and 6.17 prove that τ_{react} is a good candidate to correctly represent

the mixing regimes. The correlation between the other time scales and the homogeneous mixing degree may show to what extent higher values of one microphysical time scale can be associated to homogeneous mixing. Results in figure 6.18 are

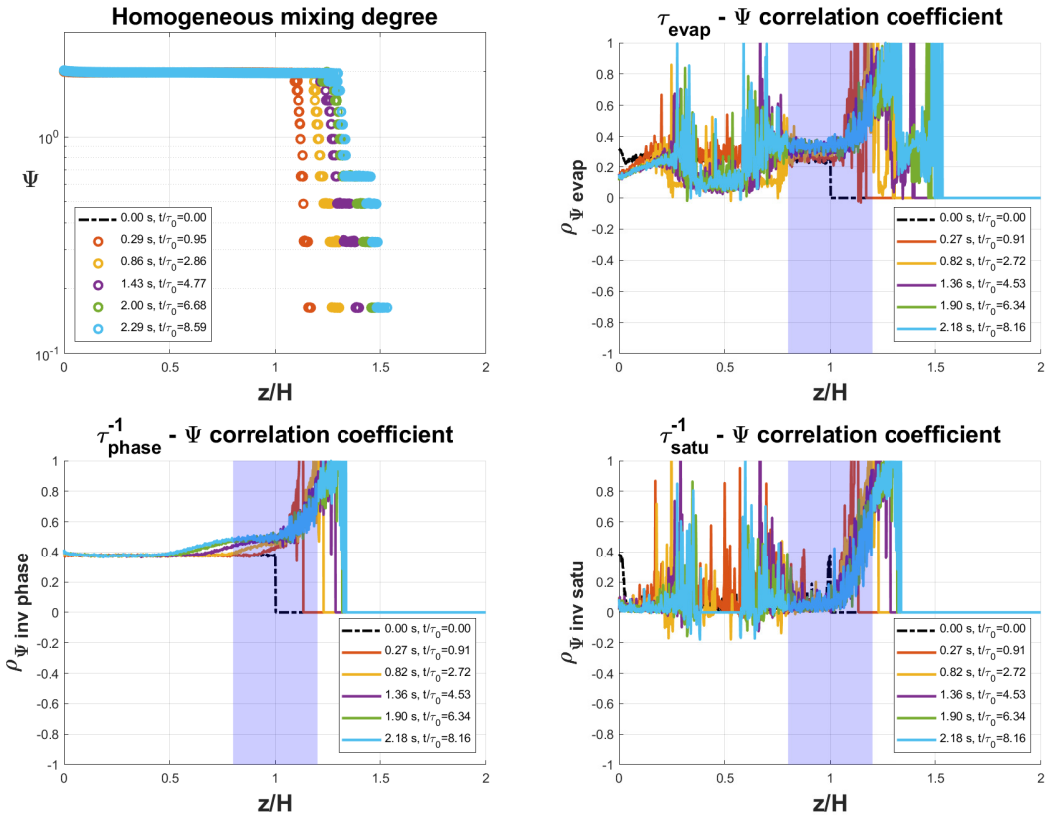

Figure 6.18: Homogeneous mixing degree and $\Psi - \tau_{microphysics}$ correlation coefficients as distributed across the interface.

plotted as ensemble averages of runs `B012`, `B017` and `B018`. Statistics appear to be less noisy for a small portion of the domain across the mixing region. The evaporation time exhibits positive correlation with Ψ, whereas the phase relaxation and saturation time are negatively and weakly correlated, respectively. A similar result for the evaporation time was found also by Lu et al., 2018 with measured data. The negative correlation of $\tau_{phase}^{-1} \propto (N\overline{r})$ is somewhat unexpected and would require further investigation. However, this analysis seems to show that the evaporation time better represents the mixing dynamics rather than τ_{phase} and τ_{satu}.

Chapter 7

Conclusion

Direct numerical simulations of a cloud-clear air interface were run under different initial configurations. All runs show the evolution of two adjacent homogeneous isotropic fields with initial $Re_\lambda = 50$ in the cloud cube. The combined effect of condensational growth and fully efficient collision-coalescence have been observed. All runs were executed for a few initial eddy turnover times in order to compute a comprehensive evolution of the slowest structures. Unstable configurations led to the rise of a small hump of kinetic energy at the mid interface and acted as additional local forcings. High interfacial temperature gradients are common in cumulus clouds (Andrejczuk et al., 2004) and may play a key role in the mixing dynamics (Malinowski et al., 2008). Anyway, both the TKE dissipation rate and the enstrophy rapidly set to quasi-steady state values. As a consequence, large droplets settle, thus reducing droplet surface variance in the mixing region. Supersaturation variance also decays rapidly during the first phase of the simulation. Although the peak in the droplet spectrum (figure 6.15) does not decrease sensibly, it shifts towards larger modal radii, which is probably an effect of growth by condensation.

No clear dependence of the variance of the droplet surface spectrum $\sigma^2_{r^2}$ on the eddy turnover time and the phase relaxation time was found. The steady state model of Chandrakar et al., 2016 does not seem to fit well the results of these experiments. However, small broadening of the initial polydisperse distribution was observed, with a few drops reaching relatively large radii ($\gtrsim 30$ µm). Condensational growth (equation 1.1) becomes uneffective for relatively large drops and collisional growth may be crucial (Devenish et al., 2012). Following Burnet and Brenguier, 2007; Lehmann et al., 2009 and the DNS works of Kumar et al., 2018; Kumar et al., 2014, the $\overline{r} - N$ mixing diagrams (figure 3.1, 3.2 and 3.3) were plotted and the plane averaged values for the local concentration and mean volume radius were mapped over these plots. Small droplets floating high above the interface tend to the inhomogeneous limit, which somewhat appears to be in good agreement with the distribution of the reaction time computed by using plane-averaged values. The

evaporation time may be the prevalent time for the region with $z/H > 1$. Small droplets that are advected upwards may easily find themselves in a subsaturated parcel and evaporate in a shorter time. The clear air slab is pushed to the fast microphysics regime as $\tau \sim \ell/u_{rms}$, a condition that is believed to foster inhomogeneous mixing. Both droplet concentration and droplet mean radius tend to zero in this region and the phase relaxation time acquires relatively high values $\tau_{phase}^{-1} \propto \overline{r}N$.

Although the phase relaxation time may be significant for regions that are characterised by more homogeneous regimes (see scattered plots for $z/H < 1$, figure 6.16), the $\Psi - \tau_{phase}^{-1}$ correlation plots suggest that this time scale does not accurately represent the mixing dynamics. In fact, basing on the argument of the Damköhler number (Andrejczuk et al., 2009) one should expect a positive correlation. Positive correlation coefficients ~ 0.35 were found for the evaporation time in the mixing region, and no correlation was found between the homogeneous mixing degree and the inverse saturation time τ_{satu}^{-1} in the mixing region.

Future simulations may introduce a fluctuating temperature field and higher values of u_{rms} and Re_λ as initial conditions. Also, the initial value of the integral scale may be increased to push the transient towards the fast microphysics regime with no need to modify the domain size or the initial droplet concentration. A model for dispersed aerosols and secondary activation should be developed too. Further DNS studies on shearless mixing and time-scale parameterization (Lu et al., 2018) are needed.

Bibliography

Andrejczuk, M., Grabowski, W. W., Malinowski, S. P., & Smolarkiewicz, P. K. (2004). Numerical Simulation of Cloud–Clear Air Interfacial Mixing. *Journal of the Atmospheric Sciences*, *61*(14), 1726–1739. doi:10.1175/1520-0469(2004)061<1726:NSOCAI>2.0.CO;2

Andrejczuk, M., Grabowski, W. W., Malinowski, S. P., & Smolarkiewicz, P. K. (2006). Numerical Simulation of Cloud–Clear Air Interfacial Mixing: Effects on Cloud Microphysics. *Journal of the Atmospheric Sciences*, *63*(12), 3204–3225. doi:10.1175/JAS3813.1

Andrejczuk, M., Grabowski, W. W., Malinowski, S. P., & Smolarkiewicz, P. K. (2009). Numerical Simulation of Cloud–Clear Air Interfacial Mixing: Homogeneous versus Inhomogeneous Mixing. *Journal of the Atmospheric Sciences*, *66*(8), 2493–2500. doi:10.1175/2009JAS2956.1

Baker, M. B., Corbin, R. G., & Latham, J. (1980). The influence of entrainment on the evolution of cloud droplet spectra: I. A model of inhomogeneous mixing. *Quarterly Journal of the Royal Meteorological Society*, *106*(449), 581–598. doi:10.1002/qj.49710644914

Baker, M. B., & Latham, J. (1979). The Evolution of Droplet Spectra and the Rate of Production of Embryonic Raindrops in Small Cumulus Clouds. *Journal of the Atmospheric Sciences*, *36*(8), 1612–1615. doi:10.1175/1520-0469(1979)036<1612:TEODSA>2.0.CO;2

Balachandar, S., & Eaton, J. K. (2010). Turbulent Dispersed Multiphase Flow. *Annual Review of Fluid Mechanics*, *42*(1), 111–133. doi:10.1146/annurev.fluid.010908.165243

Bhowmick, T., & Iovieno, M. [Michele]. (2019). Direct Numerical Simulation of a Warm Cloud Top Model Interface: Impact of the Transient Mixing on Different Droplet Population. *Fluids*, *4*(3). doi:10.3390/fluids4030144

Biona, C. B., Druilhet, A., Benech, B., & Lyra, R. L. (2001). Diurnal cycle of temperature and wind fluctuations within an African equatorial rain forest. *Agricultural and Forest Meteorology*, *109*(2), 135–141. doi:10.1016/S0168-1923(01)00253-2

Burnet, F., & Brenguier, J.-L. (2007). Observational Study of the Entrainment-Mixing Process in Warm Convective Clouds. *Journal of the Atmospheric Sciences*, *64*(6), 1995–2011. doi:10.1175/JAS3928.1

Chandrakar, K. K., Cantrell, W., Chang, K., Ciochetto, D., Niedermeier, D., Ovchinnikov, M., ... Yang, F. (2016). Aerosol indirect effect from turbulence-induced broadening of cloud-droplet size distributions. *Proceedings of the National Academy of Sciences*, *113*(50), 14243–14248. doi:10.1073/pnas.1612686113

Devenish, B. J., Bartello, P., Brenguier, J.-L., Collins, L. R., Grabowski, W. W., IJzermans, R. H. A., ... Warhaft, Z. (2012). Droplet growth in warm turbulent clouds. *Quarterly Journal of the Royal Meteorological Society*, *138*(667), 1401–1429. doi:10.1002/qj.1897

Dimotakis, P. E. (2005). Turbulent mixing. *Annual Review of Fluid Mechanics*, *37*(1), 329–356. doi:10.1146/annurev.fluid.36.050802.122015

Frisch, U., & Kolmogorov, A. (1995). *Turbulence: The Legacy of A. N. Kolmogorov*. Cambridge University Press.

Gallana, L. (2016). *Statistical analysis of inhomogeneous fluctuation fields. Scalar transport in shearless turbulent mixing, effects of stratification, solar wind and solar wind-interstellar medium interaction* (Doctoral dissertation, Politecnico di Torino).

Gao, Z., Liu, Y., Li, X., & Lu, C. (2018). Investigation of Turbulent Entrainment-Mixing Processes With a New Particle-Resolved Direct Numerical Simulation Model. *Journal of Geophysical Research: Atmospheres*, *123*(4), 2194–2214. doi:10.1002/2017JD027507. eprint: https://agupubs.onlinelibrary.wiley.com/doi/pdf/10.1002/2017JD027507

Gerber, H. E., Fricks, G. M., Jensen, J. B., & Hudson, J. G. (2008). Entrainment, Mixing, and Microphysics in Trade-Wind Cumulus. *Journal of the Meteorological Society of Japan. Ser. II*, *86A*, 87–106. doi:10.2151/jmsj.86A.87

Ghan, S. J., Abdul-Razzak, H., Nenes, A., Ming, Y., Liu, X., Ovchinnikov, M., ... Shi, X. (2011). Droplet nucleation: Physically-based parameterizations and comparative evaluation. *Journal of Advances in Modeling Earth Systems*, *3*(4). doi:10.1029/2011MS000074

Göke, S., Ochs, H. T., & Rauber, R. M. (2007). Radar Analysis of Precipitation Initiation in Maritime versus Continental Clouds near the Florida Coast: Inferences Concerning the Role of CCN and Giant Nuclei. *Journal of the Atmospheric Sciences*, *64*(10), 3695–3707. doi:10.1175/JAS3961.1

Götzfried, P., Kumar, B., Shaw, R. A., & Schumacher, J. (2017). Droplet dynamics and fine-scale structure in a shearless turbulent mixing layer with phase changes. *Journal of Fluid Mechanics*, *814*, 452–483. doi:10.1017/jfm.2017.23

Grabowski, W. W., & Vaillancourt, P. (1999). Comments on "Preferential Concentration of Cloud Droplets by Turbulence: Effects on the Early Evolution of Cumulus Cloud Droplet Spectra". *Journal of the Atmospheric Sciences*, *56*(10), 1433–1436. doi:10.1175/1520-0469(1999)056<1433:COPCOC>2.0.CO;2

Holton, J. (2004). *An Introduction to Dynamic Meteorology*. An Introduction to Dynamic Meteorology. Elsevier Science.

Howell, W. E. (1949). THE GROWTH OF CLOUD DROPS IN UNIFORMLY COOLED AIR. *Journal of Meteorology*, *6*(2), 134–149. doi:10.1175/1520-0469(1949)006<0134:TGOCDI>2.0.CO;2

Iovieno, M. [M.], Cavazzoni, C., & Tordella, D. (2001). A new technique for a parallel dealiased pseudospectral Navier–Stokes code. *Computer Physics Communications*, *141*(3), 365–374. doi:10.1016/S0010-4655(01)00433-7

Iovieno, M. [M.], Di Savino, S., Gallana, L., & Tordella, D. (2014). Mixing of a passive scalar across a thin shearless layer: concentration of intermittency on the sides of the turbulent interface. *Journal of Turbulence*, *15*(5), 311–334. doi:10.1080/14685248.2014.905393

Ishihara, T., Gotoh, T., & Kaneda, Y. (2009). Study of High–Reynolds Number Isotropic Turbulence by Direct Numerical Simulation. *Annual Review of Fluid Mechanics*, *41*(1), 165–180. doi:10.1146/annurev.fluid.010908.165203

Jiménez, J., Wray, A. A., Saffman, P. G., & Rogallo, R. S. (1993). The structure of intense vorticity in isotropic turbulence. *Journal of Fluid Mechanics*, *255*, 65–90. doi:10.1017/S0022112093002393

Katul, G. G., Geron, C. D., Hsieh, C.-I., Vidakovic, B., & Guenther, A. B. (1998). Active Turbulence and Scalar Transport near the Forest–Atmosphere Interface. *Journal of Applied Meteorology*, *37*(12), 1533–1546. doi:10.1175/1520-0450(1998)037<1533:ATASTN>2.0.CO;2

Kerr, R. A. (2009). Clouds Appear to Be Big, Bad Player in Global Warming. *Science*, *325*(5939), 376–376. doi:10.1126/science.325_376

Khain, A., Pinsky, M., & Magaritz-Ronen, L. (2018). Physical Interpretation of Mixing Diagrams. *Journal of Geophysical Research: Atmospheres*, *123*(1), 529–542. doi:10.1002/2017JD027124

Khvorostyanov, V., & Curry, J. (2014). *Thermodynamics, Kinetics, and Microphysics of Clouds*. Cambridge University Press.

Kinzer, G. D., & Gunn, R. (1951). THE EVAPORATION, TEMPERATURE AND THERMAL RELAXATION-TIME OF FREELY FALLING WATERDROPS. *Journal of Meteorology*, *8*(2), 71–83. doi:10.1175/1520-0469(1951)008<0071:TETATR>2.0.CO;2

Köhler, H. (1922). *Zur Kondensation des Wasserdampfes in der Atmosphäre*. Geofysiske Publikationer. Cammermeyers Bogh. Retrieved from https://books.google.it/books?id=3T4cnQEACAAJ

Korolev, A. V., & Mazin, I. P. (2003). Supersaturation of Water Vapor in Clouds. *Journal of the Atmospheric Sciences*, *60*(24), 2957–2974. doi:10.1175/1520-0469(2003)060<2957:SOWVIC>2.0.CO;2

Kumar, B., Götzfried, P., Suresh, N., Schumacher, J., & Shaw, R. A. (2018). Scale Dependence of Cloud Microphysical Response to Turbulent Entrainment and Mixing. *Journal of Advances in Modeling Earth Systems*, *10*(11), 2777–2785. doi:10.1029/2018MS001487

Kumar, B., Schumacher, J., & Shaw, R. A. (2013). Cloud microphysical effects of turbulent mixing and entrainment. *Theoretical and Computational Fluid Dynamics*, *27*(3–4), 361–376. doi:10.1007/s00162-012-0272-z

Kumar, B., Schumacher, J., & Shaw, R. A. (2014). Lagrangian Mixing Dynamics at the Cloudy–Clear Air Interface. *Journal of the Atmospheric Sciences*, *71*(7), 2564–2580. doi:10.1175/JAS-D-13-0294.1

Laird, N. F., Ochs, H. T., Rauber, R. M., & Miller, L. J. (2000). Initial Precipitation Formation in Warm Florida Cumulus. *Journal of the Atmospheric Sciences*, *57*(22), 3740–3751. doi:10.1175/1520-0469(2000)057<3740:IPFIWF>2.0.CO;2

Lamb, D., & Verlinde, J. (2011). *Physics and Chemistry of Clouds*. Cambridge University Press.

Lanotte, A. S., Seminara, A., & Toschi, F. (2009). Cloud Droplet Growth by Condensation in Homogeneous Isotropic Turbulence. *Journal of the Atmospheric Sciences*, *66*(6), 1685–1697. doi:10.1175/2008JAS2864.1

Latham, J., & Reed, R. L. (1977). Laboratory studies of the effects of mixing on the evolution of cloud droplet spectra. *Quarterly Journal of the Royal Meteorological Society*, *103*(436), 297–306. doi:10.1002/qj.49710343607

Lehmann, K., Siebert, H., & Shaw, R. A. (2009). Homogeneous and Inhomogeneous Mixing in Cumulus Clouds: Dependence on Local Turbulence Structure. *Journal of the Atmospheric Sciences*, *66*(12), 3641–3659. doi:10.1175/2009JAS3012.1

Li, X.-Y., Brandenburg, A., Svensson, G., Haugen, N. E. L., Mehlig, B., & Rogachevskii, I. (2020). Condensational and Collisional Growth of Cloud Droplets in a Turbulent Environment. *Journal of the Atmospheric Sciences*, *77*(1), 337–353. doi:10.1175/JAS-D-19-0107.1

Lide, D. (2004). *CRC Handbook of Chemistry and Physics, 85th Edition*. CRC Handbook of Chemistry and Physics, 85th Ed. Taylor & Francis.

Lothon, M., Lenschow, D. H., & Mayor, S. D. (2009). Doppler Lidar Measurements of Vertical Velocity Spectra in the Convective Planetary Boundary Layer. *Boundary-Layer Meteorology*, *132*(2), 205–226. doi:10.1007/s10546-009-9398-y

Lu, C., Liu, Y., & Niu, S. (2011). Examination of turbulent entrainment-mixing mechanisms using a combined approach. *Journal of Geophysical Research:*

Atmospheres, *116*(D20). doi:10.1029/2011JD015944. eprint: https://agupubs.onlinelibrary.wiley.com/doi/pdf/10.1029/2011JD015944

Lu, C., Liu, Y., Niu, S., Krueger, S., & Wagner, T. (2013). Exploring parameterization for turbulent entrainment-mixing processes in clouds. *Journal of Geophysical Research: Atmospheres*, *118*(1), 185–194. doi:10.1029/2012JD018464

Lu, C., Liu, Y., Zhu, B., Yum, S. S., Krueger, S. K., Qiu, Y., ... Luo, S. (2018). On Which Microphysical Time Scales to Use in Studies of Entrainment-Mixing Mechanisms in Clouds. *Journal of Geophysical Research: Atmospheres*, *123*(7), 3740–3756. doi:10.1002/2017JD027985

MacPherson, J. I., & Isaac, G. A. (1977). Turbulent Characteristics of Some Canadian Cumulus Clouds. *Journal of Applied Meteorology*, *16*(1), 81–90. doi:10.1175/1520-0450(1977)016<0081:TCOSCC>2.0.CO;

Malinowski, S., Andrejczuk, M., Grabowski, W., Korczyk, P., Kowalewski, T., & Smolarkiewicz, P. (2008). Laboratory and modeling studies of cloud-clear air interfacial mixing: anisotropy of small-scale turbulence due to evaporative cooling. *New Journal of Physics*, *10*(7), 075020. doi:10.1088/1367-2630/10/7/075020

Monin, A., & Yaglom, A. (2013). *Statistical Fluid Mechanics, Volume II: Mechanics of Turbulence*. Dover Books on Physics. Dover Publications.

Ovadnevaite, J., Zuend, A., Laaksonen, A., Sanchez, K. J., Roberts, G., Ceburnis, D., ... O' Dowd, C. (2017). Surface tension prevails over solute effect in organic-influenced cloud droplet activation. *Nature*, *546*, 637–641. doi:doi:10.1038/nature22806

Pawlowska, H., Brenguier, J., & Burnet, F. (2000). Microphysical properties of stratocumulus clouds. *Atmospheric Research*, *55*(1), 15–33. doi:10.1016/S0169-8095(00)00054-5

Petters, M. D., & Kreidenweis, S. M. (2007). A single parameter representation of hygroscopic growth and cloud condensation nucleus activity. *Atmospheric Chemistry and Physics*, *7*(8), 1961–1971. doi:10.5194/acp-7-1961-2007

Pinsky, M. B., Khain, A. P., & Levin, Z. (1999). The role of the inertia of cloud drops in the evolution of the spectra during drop growth by diffusion. *Quarterly Journal of the Royal Meteorological Society*, *125*(554), 553–581. doi:10.1002/qj.49712555410

Pope, S. B. (2000). *Turbulent Flows*. doi:10.1017/CBO9780511840531

Pöschl, U., Martin, S. T., Sinha, B., Chen, Q., Gunthe, S. S., Huffman, J. A., ... Andreae, M. O. (2010). Rainforest Aerosols as Biogenic Nuclei of Clouds and Precipitation in the Amazon. *Science*, *329*(5998), 1513–1516. doi:10.1126/science.1191056

Pruppacher, H., & Klett, J. (2010). *Microphysics of Clouds and Precipitation*. Atmospheric and Oceanographic Sciences Library. Springer Netherlands.

Radkevich, A., Lovejoy, S., Strawbridge, K. B., Schertzer, D., & Lilley, M. (2009). Scaling turbulent atmospheric stratification. III: Space–time stratification of passive scalars from lidar data. *Quarterly Journal of the Royal Meteorological Society*, *134*(631), 317–335. doi:10.1002/qj.203

Rangno, A. L., & Hobbs, P. V. (2005). Microstructures and precipitation development in cumulus and small cumulonimbus clouds over the warm pool of the tropical Pacific Ocean. *Quarterly Journal of the Royal Meteorological Society*, *131*(606), 639–673. doi:10.1256/qj.04.13

Rogers, R., & Yau, M. (1996). *A Short Course in Cloud Physics*. Elsevier Science.

Sardina, G., Picano, F., Brandt, L., & Caballero, R. (2015). Continuous Growth of Droplet Size Variance due to Condensation in Turbulent Clouds. *Phys. Rev. Lett. 115*, 184501. doi:10.1103/PhysRevLett.115.184501

Schemenauer, R., MacPherson, J., Isaac, G., & Strapp, J. (1980). *Canadian participation in HIPLEX 1979* (Report APRB No. 110). Atmospheric Environment Service, Environment Canada.

Sedunov, I. (1974). *Physics of Drop Formation in the Atmosphere*. Halsted Press Book. John Wiley & Sons.

Seinfeld, J., & Pandis, S. (2016). *Atmospheric Chemistry and Physics: From Air Pollution to Climate Change*. Wiley.

Shaw, R. A. [Raymond A.]. (2000). Supersaturation Intermittency in Turbulent Clouds. *Journal of the Atmospheric Sciences*, *57*(20), 3452–3456. doi:10.1175/1520-0469(2000)057<3452:SIITC>2.0.CO;2

Shaw, R. A. [Raymond A.]. (2003). Particle-Turbulence Interaction in Atmospheric Clouds. *Annual Review of Fluid Mechanics*, *35*(1), 183–227. doi:10.1146/annurev.fluid.35.101101.161125

Shaw, R. A. [Raymond A.], Reade, W. C., Collins, L. R., & Verlinde, J. (1998). Preferential Concentration of Cloud Droplets by Turbulence: Effects on the Early Evolution of Cumulus Cloud Droplet Spectra. *Journal of the Atmospheric Sciences*, *55*(11), 1965–1976. doi:10.1175/1520-0469(1998)055<1965:PCOCDB>2.0.CO;2

Shaw, R. A. [Raymond A.], Reade, W. C., Collins, L. R., & Verlinde, J. (1999). Comments on "Preferential concentration of cloud droplets by turbulence: Effects on the early evolution of cumulus cloud droplet spectra": Reply. *Journal of the Atmospheric Sciences*, *56*(10), 1437–1441. doi:10.1175/1520-0469(1999)056<1437:R>2.0.CO;2

She, Z.-S., Jackson, E., & Orszag, S. A. (1990). Intermittent vortex structures in homogeneous isotropic turbulence. *Nature*, *344*, 226–228. doi:10.1038/344226a0

Siebert, H. [H.], Gerashchenko, S., Gylfason, A., Lehmann, K., Collins, L., Shaw, R., & Warhaft, Z. (2010). Towards understanding the role of turbulence on droplets in clouds: In situ and laboratory measurements. *Atmospheric*

Research, *97*(4), 426–437. From the Lab to Models and Global Observations: Hans R. Pruppacher and Cloud Physics. doi:https://doi.org/10.1016/j.atmosres.2010.05.007

Siebert, H. [H.], Lehmann, K., & Wendisch, M. (2006). Observations of Small-Scale Turbulence and Energy Dissipation Rates in the Cloudy Boundary Layer. *Journal of the Atmospheric Sciences*, *63*(5), 1451–1466. doi:10.1175/JAS3687.1

Siebert, H. [H.], Shaw, R. A. [R. A.], & Warhaft, Z. (2010). Statistics of Small-Scale Velocity Fluctuations and Internal Intermittency in Marine Stratocumulus Clouds. *Journal of the Atmospheric Sciences*, *67*(1), 262–273. doi:10.1175/2009JAS3200.1

Siebert, H. [Holger], & Shaw, R. A. [Raymond A.]. (2017). Supersaturation Fluctuations during the Early Stage of Cumulus Formation. *Journal of the Atmospheric Sciences*, *74*(4), 975–988. doi:10.1175/JAS-D-16-0115.1

Szumowski, M. J., Rauber, R. M., Ochs, H. T., & Miller, L. J. (1997). The Microphysical Structure and Evolution of Hawaiian Rainband Clouds. Part I: Radar Observations of Rainbands Containing High Reflectivity Cores. *Journal of the Atmospheric Sciences*, *54*(3), 369–385. doi:10.1175/1520-0469(1997)054<0369:TMSAEO>2.0.CO;2

Tennekes, H., & Lumley, J. (1972). *A First Course in Turbulence*. MIT Press. Pe Men Book Company.

Tölle, M. H., & Krueger, S. K. (2014). Effects of entrainment and mixing on droplet size distributions in warm cumulus clouds. *Journal of Advances in Modeling Earth Systems*, *6*(2), 281–299. doi:10.1002/2012MS000209

Tordella, D., & Iovieno, M. [M.]. (2006). Numerical experiments on the intermediate asymptotics of shear-free turbulent transport and diffusion. *Journal of Fluid Mechanics*, *549*, 429–441. doi:10.1017/S0022112005007688

Tordella, D., & Iovieno, M. [M.]. (2011). Small-Scale Anisotropy in Turbulent Shearless Mixing. *Phys. Rev. Lett. 107*, 194501. doi:10.1103/PhysRevLett.107.194501

Tordella, D., Iovieno, M., & Bailey, P. R. (2008). Sufficient condition for Gaussian departure in turbulence. *77*(1), 016309. doi:10.1103/PhysRevE.77.016309

Tritton, D. (1988). *Physical Fluid Dynamics*. Oxford Science Publ. Clarendon Press.

Vaillancourt, P. A., & Yau, M. K. (2000). Review of Particle-Turbulence Interactions and Consequences for Cloud Physics. *Bulletin of the American Meteorological Society*, *81*(2), 285–298. doi:10.1175/1520-0477(2000)081<0285:ROPIAC>2.3.CO;2

Vaillancourt, P. A., Yau, M. K., Bartello, P., & Grabowski, W. W. (2002). Microscopic Approach to Cloud Droplet Growth by Condensation. Part II:

Turbulence, Clustering, and Condensational Growth. *Journal of the Atmospheric Sciences*, *59*(24), 3421–3435. doi:10.1175/1520-0469(2002)059<3421:MATCDG>2.0.CO;2

Vaillancourt, P. A., Yau, M. K., & Grabowski, W. W. (2001). Microscopic Approach to Cloud Droplet Growth by Condensation. Part I: Model Description and Results without Turbulence. *Journal of the Atmospheric Sciences*, *58*(14), 1945–1964. doi:10.1175/1520-0469(2001)058<1945:MATCDG>2.0.CO;2

Vallis, G. (2006). *Atmospheric and Oceanic Fluid Dynamics: Fundamentals and Large-scale Circulation*. Cambridge University Press.

Wex, H., Stratmann, F., Topping, D., & McFiggans, G. (2008). The Kelvin versus the Raoult Term in the Köhler Equation. *Journal of the Atmospheric Sciences*, *65*(12), 4004–4016. doi:10.1175/2008JAS2720.1

Yang, F., Shaw, R., & Xue, H. (2016). Conditions for super-adiabatic droplet growth after entrainment mixing. *Atmospheric Chemistry and Physics*, *16*(14), 9421–9433. doi:10.5194/acp-16-9421-2016

Yum, S. S., Wang, J., Liu, Y., Senum, G., Springston, S., McGraw, R., & Yeom, J. M. (2015). Cloud microphysical relationships and their implication on entrainment and mixing mechanism for the stratocumulus clouds measured during the VOCALS project. *Journal of Geophysical Research: Atmospheres*, *120*(10), 5047–5069. doi:10.1002/2014JD022802